

LIBRARY Michigan State University

This is to certify that the

dissertation entitled

Microwave-Microwave and Infrared-Microwave Double Resonance Spectroscopy of $$^{\rm NH}_3$, $^{\rm CH}_3{}^{\rm OH}$ and $^{\rm CF}_3{}^{\rm I}$$

presented by

Dean B. Peterson

has been accepted towards fulfillment of the requirements for

Ph.D. degree in Chemistry

Major professor

Date December 21, 1987



RETURNING MATERIALS:
Place in book drop to remove this checkout from your record. FINES will be charged if book is returned after the date stamped below.

MICROWAVE-MICROWAVE AND INFRARED-MICROWAVE DOUBLE RESONANCE SPECTROSCOPY OF NH $_3$, CH $_3$ OH AND CF $_3$ I

Ву .

Dean B. Peterson

A DISSERTATION

Submitted to

Michigan State University

in partial fulfillment of the requirements

for the degree of

DOCTOR OF PHILOSOPHY

Department of Chemistry

1987

ABSTRACT

MICROWAVE-MICROWAVE AND INFRARED-MICROWAVE DOUBLE RESONANCE SPECTROSCOPY OF NH3, CH3OH AND CF3I

Вy

Dean B. Peterson

Double resonance spectroscopy involves the simultaneous application of two radiations to a sample at frequencies that are resonant with transitions in the sample molecule. There are many different types of double resonance methods. Two distinct techniques, 3-level and 4-level double resonance, can be discussed. In either case the higher power radiation is termed the pumping source (pump) and the lower power radiation is termed the signal source (probe).

The 4-level double resonance technique was used to study energy transfer by collisions in rotational energy levels of NH_3 with He and H_2 as collision partners. The rotational transitions were monitored and pumped by microwave radiation. The experimental details and results of the microwave-microwave double resonance study is presented in the thesis.

The 3-level double resonance technique is used for simplification and assignment of spectra. An infrared-microwave double resonance experiment was developed using a Fourier transform infrared spectrometer. A discussion of the results from the double resonance experiment is given.

An infrared-microwave double resonance spectrometer has been developed in our laboratory which employs a powerful microwave source, a cylindrical cavity sample cell, and a tunable infrared microwave sideband laser. With this apparatus, a ground state microwave transition, whose assignment and frequency are normally known, can be selected for pumping and the infrared spectrometer can then be scanned to locate vibration-rotation transitions that are affected by the pumped microwave transition. The results of a study of CH₃OH including a lineshape analysis are given along with results from experiments on CF₃I.

To Sue

ACKNOWLEDGMENTS

I would like to thank Professor Richard H. Schwendeman for his great help throughout these studies, not only as an advisor, but also as a good friend.

My thanks are also extended to Mr. Ron Haas for his work and wit to help me endure the FTIR days.

I would also like to thank the members of the group throughout the years for their discussions and friendship.

A special thanks is extended to my parents for their encouragement and belief in me.

Finally I would like to thank Sue for always being there. (IOEO)!

TABLE OF CONTENTS

LIST C	F TAI	BLES	• •	• •	•	•	•	•	•	•	•	•	•	•	•	•	•	•	•	•	.ix
LIST O	F FI	BURES	· .		•	•	•	•	•	•	•	•	•	•	•	•	•	•	•	•	.xi
CHAPTE	R I.	Int	rodu	cti	on	•	•	•	•	•	•	•	•	•	•	•	•	•	•	•	.1
CHAPTE	R II.	. Fo	ur-I	eve	1 1	lic	ro	wa	ve	-M	ic	ro	wa	ve	D	ou	b l	e			
	Reso	nance	in	NH ₃	-н	e a	nd	N	H ₃	-H	2	Ga	s	Mi	хt	ur	es	١.	•	•	. 7
	2.1	Intr	oduc	tio	n.	•	•		•	•	•		•		•	•	•		•	•	. 7
	2.2	Theo	ry.		•	•	•	•	•	•	•	•	•	•	•	•		•	•	•	.10
	2.3	Expe	rime	enta	1.	•	•	•	•	•		•			•		•	•		•	. 16
	2.4	Resu	ılts		•	•	•	•	•	•	•	•	•		•	•	•	•	•	•	.21
	2.5	Refe	erend	es.	•	•	•	•	•	•		•	•	•	•	•	•	•	•	•	. 25
CHAPTE	R II	ı. 1	nfre	red	-M:	icr	.ow	av	е	Do	ub	le	R	es	or	an	ce	: T	s i	.ng	£
	a Fo	urier	Tre	nsf	ori	n I	n f	ra	re	d	Sp	ec	tr	0	et	er	٠.	•	•	•	. 27
	3.1	Intr	roduc	ctio	n.	•	•	•	•	•	•	•	•	•		•	•	•	•	•	. 27
	3.2	The	ory.			•	•	•	•		•		•	•		•	•	•	•	•	.31
		Co	here	ence	S	pli	tt	in	g	•	•		•	•	•	•	•	•	•	•	.31
		Fo	ourie	er T	rai	n s f	or	m	Sp	ec	tr	05	co	РУ	•	•	•	•	•	•	. 36
	3.3	Вхре	erime	ent.	•	•	•		•	•	•		•	•	•	•	•	•	•	•	. 44
		Ir	stru	ımen	ta	tio	n	•	•		•			•		•	•	•	•	•	. 44
		Sa	ample	Pr	oc	ess	in	g	•	•	•	•		•	•	•	•	•	•	•	.58
	3.4	Resu	ılts		•	•	•		•	•	•	•		•	•	•	•	•	•	•	. 62
	3.5	Refe	erend	ces.	•	•	•		•	•	•			•	•	•		•	•	•	. 67
CHAPTI	BR IV	. I	nfra	red	Mi	cro	wa	ve	s	id	eb	an	d	La	86	er					
	Spec	tros	сору	of	СН	3 ^{OE}	Ι.	•	•	•	•	•		•	•	•	•	•	•	•	. 68
	4.1	Int	coduc	etic	n.					_			_								. 68

4.2	Theory	0
	General Spectroscopy	0
	Methanol	7
4.3	Experimental	8
	Introduction	8
	CO ₂ Laser	8
	Sideband	0
4.4	Results and Discussion	9
4.5	References	06
CHAPTER V.	Infrared-Microwave Double Resonance with a	
Side	eband Laser	08
5.1		
5.2		
	Methanol (CH ₃ OH)	
	CF ₃ I	
	Lineshape Analysis and Generation l	
	Absorption Coefficient	
5.3	Experimental	
	CO ₂ Sideband Laser	
	Microwave Pump	
	Double Resonance Spectrometer	
5 4	Results and Discussion	
0.1	Infrared-Microwave Double Resonance in	
		20
	CH ₃ OH	30
	CF ₃ I	40

	Lineshapes	3 0	f	In	fr	ar	ed [.]	-Mi	cr	OW	ave	e I	001	ıb.	le		
	Resonance	Si	gn	al	8	in	C	H ₃ 0	Н.	•	•	•	•	•	•	•	. 152
5.5	References.	•	•	•	•	•	•		•	•	•	•	•	•	•	•	.156
CHAPTER VI	. Summary as	ad	Fu	tu	re	W	or	k.	•	•	•	•	•	•	•	•	.158
6.1	Summary	•	•	•	•	•	•		•	•	•	•	•	•	•	•	. 158
6.2	Future Work	•	•	•	•	•	•		•	•	•	•	•	•	•	•	.161
6.3	References.	•	•	•	•	•	•		•	•	•	•	•	•	•	•	. 166
APPRNDTY		_		_		_	_										. 167

LIST OF TABLES

Table	Page
2.1	Comparison of calculated and experimental
	values of four-level double resonance
	effects in NH ₃ -He mixtures
2.2	Comparison of calculated and experimental
	values of four-level double resonance
	effects in NH ₃ -H ₂ mixtures
2.3	Four-level double resonance effects in
	NH ₃ -He
2.4	Four-level double resonance effects in
	NH ₃ -H ₂
3.1	The first ten roots of $J_m(x) = 054$
4.1	Selection rules for asymmetric rotor
	rotational transitions
4.2	Parameters used to calculate the energy
	levels of the ground and $v_5 = 1$ states of
	сн ₃ он
4.3	Calculated energies and coefficients for
	the vibrational ground state of CH_3OH 86
4.4	Calculated energies and coefficients for
	the CO stretching state of CH ₃ OH 87
4.5	Comparison of observed and calculated
	frequencies of CH ₃ OH transitions 104
5.1	Vibration-rotation parameters for the ground
	and v_1 =1 states of CF_3I

5.2	CH ₃ OH double resonance experimental
	results
5.3	Pumped ground state rotational transitions
	in CF ₃ I
5.4	Parameters for CF_3I transitions in the $10~\mu m$
	region

LIST OF FIGURES

Figure	Page
1.1	Energy level diagram presenting various
	3-level and 4-level double resonance
	schemes. The thick and thin arrows
	represent pump and signal transitions,
	respectively
2.1	An energy level diagram of symmetrically
	split levels in ammonia. The pump
	increases or decreases the absorption
	signal intensity depending on whether
	$k_{\Phi} < k_{\chi} \text{ or } k_{\Phi} > k_{\chi}$. Here, k denotes
	the rate constant for the process11
2.2	Block diagram of microwave-microwave
	four-level double resonance spectrometer17
2.3	Plot of microwave detector signal vs.
	power/max. power. Attenuators before and
	after the sample cell were manipulated in
	such a way that the microwave power inside
	the cell could be changed without changing
	the power at the detector. The results of
	this plot show that the pumping transition
	could be brought to within 1-2% of complete
	saturation at the highest powers20
3.1	Energy level diagram for single and double
	resonance

3.2	An example of the use of radio frequency
	microwave double resonance (RFMDR) to
	simplify spectra. The upper trace is a
	portion of the normal Stark modulated
	microwave spectrum of ethyl formate.
	The lower trace is the RFMDR spectrum in
	the same region with the radio frequency
	pump coincident with a transition. Only
	the three level resonances in the ground
	(v=0) and first excited state (v=1)
	appear strongly in the spectrum. The
	simplification in the RFMDR spectrum is
	evident (from Wodarczyk and Wilson, (11)) .37
3.3	Diagram of a Michelson interferometer40
3.4	Interferogram taken by a BOMEM DA3.01 FTIR
	of CH_3F at 0.02 cm ⁻¹ resolution42
3.5	Spectrum calculated from interferogram of
	CH_3F at 0.02 cm ⁻¹ resolution
3.6	Block diagram of FTIR-microwave double
	resonance spectrometer
3.7	Diagram of optical components in BOMEM
	DA3.01 FTIR spectrometer
3.8	Diagram of the Cassegrain mirror arrangement
	used to reduce the diameter of the infrared
	beam from the BOMEM interferometer49
3.9	Diagram of microwave cavity cell used in

	double resonance experiment
3.10	Diagrams of field lines for 3 low-order
	modes in circular waveguide. The solid
	lines show electric field directions,
	whereas the dashed lines show magnetic
	field directions (from Moreno (14))52
3.11	Plot of reflected power from microwave
	cavity cell versus microwave frequency.
	The sharp dips indicate resonances in the
	cell
3.12	Plot of reflected power versus microwave
	frequency for one resonance of the TEll
	mode
3.13	A comparison of a normal spectrum and a
	modulated spectrum of NH_3 at 0.02 cm ⁻¹ .
	The upper trace is the normal calculated
	spectrum of NH3. The lower trace is the
	calculated spectrum using amplitude
	modulation and phase sensitive detection
	on the interferometer signal 60
3.14	A comparison of calculated interferograms
	from simulated spectra. Trace (A) was
	calculated with a splitting of 5 data
	points. Traces (B) and (C) were calculated
	with increasing splitting, respectively64
4.1	The variation of energy levels with I and

	K for a molecule of slight asymmetry. The
	deviations of the curves from horizontal
	lines represent the deviations from the
	levels of a symmetric top
4.2	Energy levels of a hindered rotor with
	three potential minima and various
	asymmetries and barrier heights: (A)
	symmetric rigid rotor, very high barrier,
	(B) symmetric rotor, intermediate barrier,
	(C) asymmetric rotor, intermediate
	barrier, (D) asymmetric rotor, high
	barrier, (E) asymmetric rotor, very high
	barrier (9)
4.3	A schematic representation of the CH ₃ OH
	molecule
4.4	Vibration-rotation spectra comparing a
	symmetric top molecule to an asymmetric
	molecule with a torsional barrier. It
	should be noted that the scale of
	splitting for the symmetric top is five
	times that for the asymmetric top with
	internal rotation
4.5	A block diagram of an extra-cavity laser
	stabilization scheme used on the CO ₂ laser.91
4.6	A diagram of the sideband modulator. The
	CdTe crystal is inserted between two Al O

	slabs in a brass housing that is matched
	to double-ridged waveguide
4.7	A diagram of the electric fields of the
	CO2 laser and sideband laser as created
	by the sideband modulator crystal 95
4.8	A diagram of the sideband laser
	spectrometer
4.9	FTIR spectrum of the CO stretch band of
	сн ₃ он
4.10	A typical scan of the sideband laser
	showing four transitions of CH ₃ OH. The
	CO ₂ laser is fixed at the 9P(26) laser
	line while the microwaves are swept101
4.11	A plot of the ratio of $(-/+)$ sidebands
	versus microwave frequency for two
	different laser lines (9P(16) (o) and
	10R(24) (x))
5.1	Three level energy diagram used for
	density matrix calculation
5.2	Calculated lineshape using a Rabi
	frequency of 100 MHz for the pumping
	radiation
5.3	Block diagram of CO ₂ sideband laser
	spectrometer
5.4	Block diagram of infrared microwave double
	resonance spectrometer

5.5	Resonance cavity cell used in infrared
	microwave double resonance experiment to
	obtain high microwave fields
5.6	Absorption spectrum of CH ₃ OH. The CO ₂
	laser is on the 9P(24) laser line and the
	microwaves are swept from 15.0 to 16.0 GHz.141
5.7	Double resonance spectrum of CH3OH over
	the same region as figure 5.6. This shows
	the selectivity of the double resonance
	technique
5.8	Infrared microwave double resonance
	spectrum of CF3I. The CO2 laser is on the
	9R(16) laser line. The pump frequency is
	15,287.6 MHz
5.9	Trace A shows the double resonance signal
	of CH ₃ OH with the pumping frequency on
	resonance with the pumped transition.
	Trace B is 150 MHz off resonance and
	Trace C is 300 MHz off resonance. The ${\rm CO}_2$
	laser is on the 9P(24) laser line145
5.10	Infrared microwave double resonance
	spectrum of CF3I. The CO2 laser is on the
	9R(16) laser line. The pumping frequency
	is 12,150.0 MHz
5.11	Infrared microwave double resonance
	spectrum of CF ₂ I. The CO ₂ laser is on the

	9R(16) laser line. The pumping frequency
	is 9,000.0 MHz
5.12	Calculated lineshape using different Rabi
	frequencies. The signal with the largest
	amplitude was generated using the largest
•	Rabi frequency
5.13	Experimental results for the infrared-
	microwave double resonance on the R(4,1)A
	transition of CH ₃ OH, obtained using
	different pumping powers. The CO ₂ laser
	is on the 9P(24) laser line
6.1	Diagram of sideband laser Lamb-dip
	spectrometer
6.2	A plot of a Stark modulated Lamb-dip from
	the Q(5,3) transition of CH_3F 165

CHAPTER I

Introduction

High resolution infrared and microwave spectroscopy, i.e., the detection and interpretation of molecular transitions, has rapidly progressed in the past two decades. There are new developments of higher resolution and faster acquisition instruments almost daily. One spectroscopic tool useful for many applications and extensively used in our laboratory is the technique of double resonance.

Double resonance spectroscopy involves the simultaneous application of two fields of radiation on the sample, both resonant with transitions in the sample molecule. One of the fields, the pump, must have enough strength to perturb the system either by changing the population distribution of the two levels involved or by creating a coherence splitting of the pumped levels. These two changes will be discussed in more detail in the following chapters. The second field, the probe or signal, must be weak so not to disturb the related energy levels. The probe radiation is used only to monitor the effect of the pump on the transition in resonance with the probe.

Double resonance was first used in the microwave and radiofrequency regions (1-3). After the advent of the

laser, double resonance was extended to the infrared, visible, and ultraviolet regions of the electromagnetic spectrum. Since the first investigation using a laser (4) many scientists have used double resonance techniques for a variety of studies.

There are two types of double resonance systems, which can be separated by their mechanisms and the information obtained from each. In the first, the two transitions in resonance with the frequencies of the applied fields have a common level (the three level system). The second type does not have a common level; this is known as a four level system. These two double resonance mechanisms are explained in Figure 1.1 by energy level diagrams. In the three level system, the pumping effect on the energy level in common is directly monitored by the changes in the probed transition. This system is used for investigations to identify particular transitions. In the four level system, the effects of the pumping radiation on the molecule must be transmitted to the energy levels of the probe radiation through intermolecular collisions. Observations of these double resonance signals lead to information about the collisional process and the collisional "selection rules" (5). The four level double resonance system can also be used to increase the populations of upper levels associated with excited vibrational bands. The four level system is

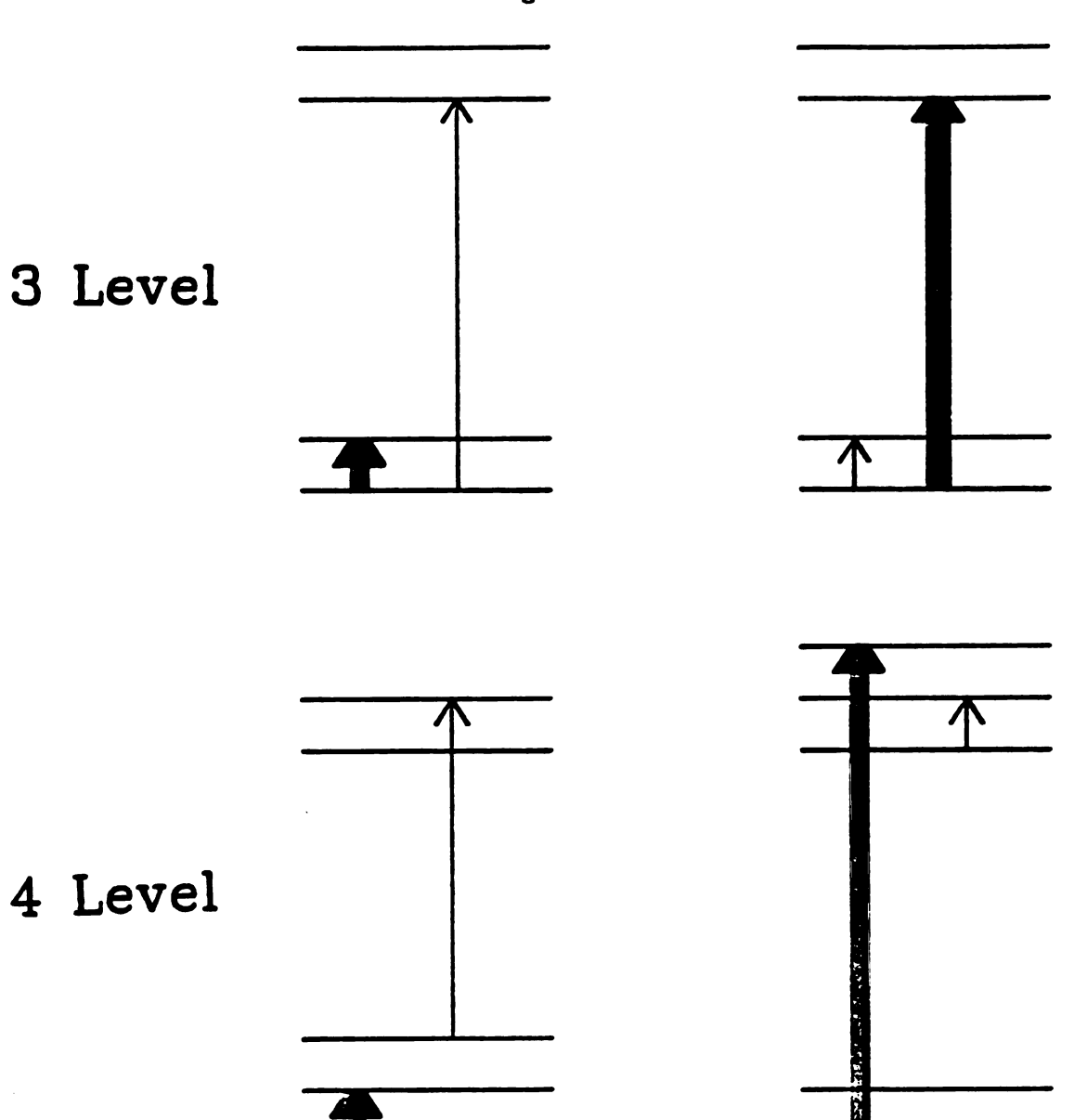


Figure 1.1. Energy level diagram presenting various 3-level and 4-level double resonance schemes. The thick and thin arrows represent pump and signal transitions, respectively.

then used to increase the intensity of a hot band or combination band transition. The two different systems introduced above will be presented in experiments in this thesis.

The thesis describes a combination of different techniques of double resonance used for molecular studies on NH_3 , CH_3F , CH_3OH , and CF_3I . The material is presented in a chronological order in the author's graduate research program. Chapter 2 describes a microwave-microwave four level double resonance experiment performed on NH_3 -He and NH_3 -H₂ gas mixtures. This experiment was used to confirm results obtained earlier by Oka et al. (6-9).

Chapter 3 presents the theoretical foundation of the infrared-microwave double resonance experiments. The background theory of Fourier transform infrared spectroscopy is also given. Chapter 3 explains the FTIR-microwave double resonance experiment and gives the results from the study.

Chapter 4 introduces the theoretical considerations used to predict and calculate transitions. It also describes the theory of the methanol molecule. The CO₂ sideband laser is introduced in Chapter 4, along with the use of extra cavity CO₂ laser stabilization. A list of CH₃OH transitions is given and a comparison of results from diode laser experiments (10,11) is made.

The infrared-microwave double resonance experiment

using the ${\rm CO}_2$ sideband laser as the infrared source is presented in Chapter 5. Chapter 5 explains the theory of ${\rm CF}_3{\rm I}$ and the lineshape obtained from the double resonance experiment. Results form a double resonance study of ${\rm CH}_3{\rm OH}$ and ${\rm CF}_3{\rm I}$ are given.

The final chapter of the thesis is a summary of the work. This chapter gives an overall view of the work accomplished and a proposal for future experiments in the field of double resonance spectroscopy.

References

- T. Yajima, and K. Shimoda, J. Phys. Soc. Japan., <u>15</u>,
 1668 (1960).
- 2. K. Shimoda, J. Phys. Soc. Japan., 14, 954 (1959).
- 3. A. Battaglia, A. Gazzini, and E. Polacca,
 Nuovo Cimento, <u>14</u>, 1076 (1959).
- 4. A. M. Ronn, and D. R. Lide, J. Chem. Phys. <u>47</u>, 3669 (1967).
- 5. T. Oka, Adv. Atom. Mol. Phys. 9, 127 (1974).
- 6. T. Oka, J. Chem. Phys. <u>47</u>, 13 (1967).
- 7. T. Oka, J. Chem. Phys. 47, 4852 (1967).
- 8. T. Oka, J. Chem. Phys. 48, 4919 (1968).
- 9. T. Oka, J. Chem. Phys. 49, 3135 (1968).
- lO. P. W. Daly, and T. Oka, J. Chem. Phys. <u>53</u>, 3272 (1970).
- A. R. Fabris, and T. Oka, J. Chem. Phys. <u>56</u>, 3168
 (1972).

CHAPTER II

Four-Level Microwave-Microwave Double Resonance in

 $\frac{\mathrm{NH_3-He}}{\mathrm{and}}$ and $\frac{\mathrm{NH_3-H_2}}{\mathrm{3}}$ Gas Mixtures.

2.1 Introduction

Four-level microwave-microwave double resonance
measurements can be used to determine relative probabilities
of collision induced transitions. By observing these
effects, collisional "selection rules" for different gas
mixtures can be obtained.

In a four-level double resonance process, the equilibrium populations in two molecular levels are perturbed by the absorption of radiation at the resonance frequency. The collisional effect is then monitored in another two-level system by observing the absorption of a weak radiation signal at this second resonance frequency. It is important to understand that these molecular energy levels are not connected. Therefore the only possible effect of one transition on another is through a collision.

A series of four-level double resonance experiments were done by Oka and co-workers on many different molecules (1-6). One particular group of experiments on NH₃ with

different collisional partners has attracted a large amount of attention (2-8).

The interstellar NH_3 molecules show nonthermal population distributions among the low lying rotation—inversion levels (9). Because NH_3 molecules collide mostly with H or He atoms or H_2 molecules in interstellar space, the fundamental data on NH_3 - H_2 and NH_3 -He collisions are useful for the interpretation of this abnormal stationary state distribution.

The experimental data have since been compared to calculated double resonance effects on the NH_3 -He system by Davis and Green (10) with only partial success and by Billing and Diercksen (11), whose results match the experimental values. Billing and Diercksen (12) also did calculations on the NH₂-H₂ system, but the calculated results were not in good agreement with the observed values. The unsatisfactory nature of the comparison between theory and experiment led Davis and Green to the following statement (10): "Although it is possible that the theory still suffers from some unidentified problem, the methods used have been remarkably successful in predicting detailed experimental results,... We therefore suggest that further progress in understanding NH_3 rare gas collisions might require reexamination of the experimental work". In order to test the validity of the experimental data, we repeated

many of the four-level double resonance measurements on $\rm NH_3-H_2$ mixtures.

Both the $\mathrm{NH_3}$ -He and $\mathrm{NH_3}$ -H₂ collisional effects were studied in the microwave spectroscopy laboratory at Michigan State University. In this experiment a strong microwave source (pump) is tuned to a resonant frequency of an $\mathrm{NH_3}$ inversion transition while a second very weak microwave source (signal) is tuned to a second inversion transition. The absorption of the signal radiation with the pump turned off ($\mathrm{I_{off}}$) is compared to the absorption when the pump source saturates its transition ($\mathrm{I_{on}}$). The comparison is expressed as the ratio $\Delta\mathrm{I/I}$ where $\Delta\mathrm{I}=\mathrm{I_{on}}$ - $\mathrm{I_{off}}$ and $\mathrm{I}=\mathrm{I_{off}}$. Through this observation of $\Delta\mathrm{I/I}$ the collisional "selection rules" can be analyzed.

The next section outlines the history of the theory and shows in particular how this applies to the NH₃ molecule. In the following section the experimental apparatus is described. Then the final section states the results of our experiment compared to the calculated and experimental results of previous studies.

2.2 Theory

The energy levels studied in this work are composed of inversion doublets of ammonia as shown in Figure 2.1. Many of the transitions between the inversion doublets fall in the 20-26 GHz microwave region. In Figure 2.1 the pumping radiation is indicated by the bold arrow $v_{_{\mathbf{D}}}$ and the signal is denoted ν_{α} . There are three possible outcomes which could result from this experiment. The first is when the rate of the parity changing X transition is greater than that of the parity conserving ϕ transition. In this case the signal absorption should increase when the pump radiation is turned on. In the second situation, the rates of both types of transitions are comparable; this case would give no change in signal absorption. The final case is when the o transition rate is greater than the x transition rate. This situation would produce an decrease in signal absorption. The observation of this can be shown as $\Delta I/I$ being either positive or negative. Of course, if the second case were to occur, the method would prove to be useless, however the probability of these rates being exactly equal is quite small.

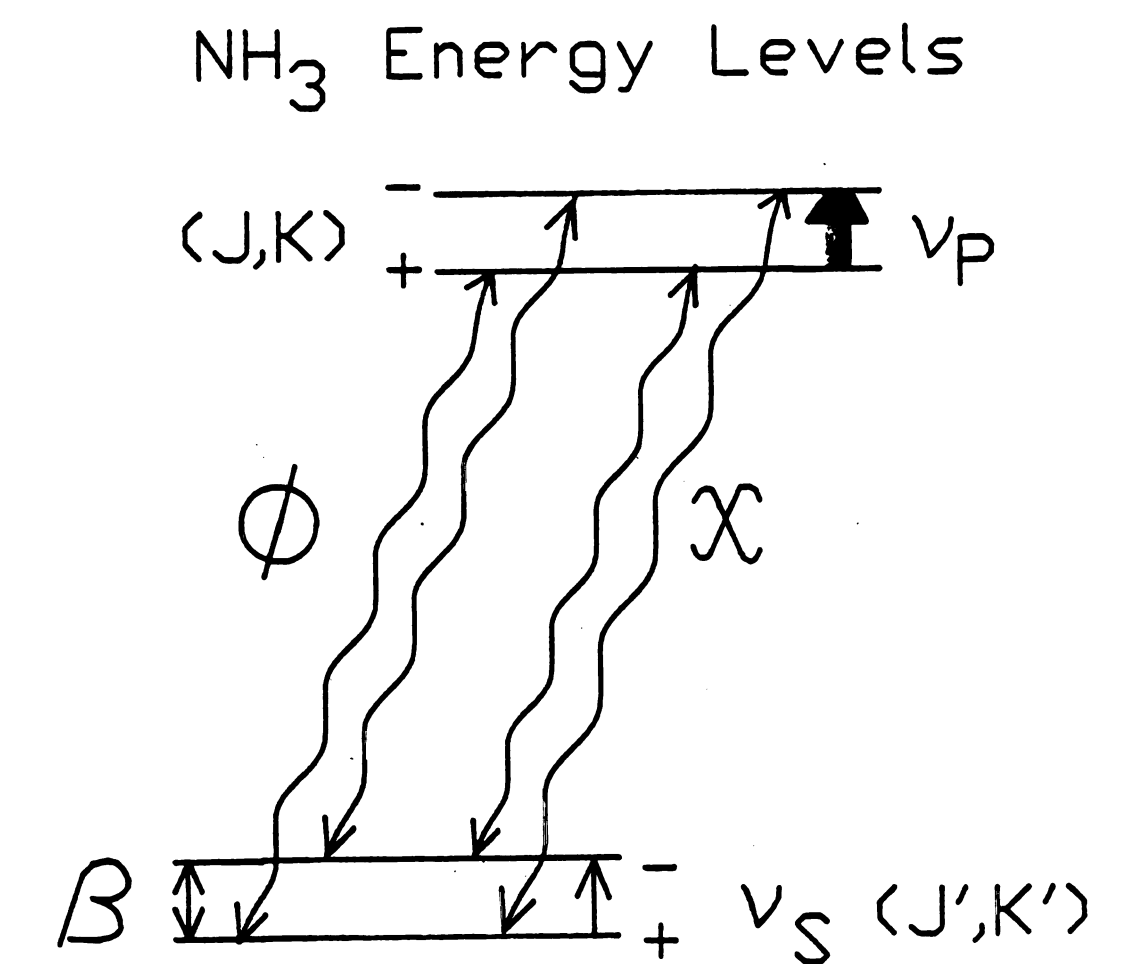


Figure 2.1. An energy level diagram of symmetrically split levels in ammonia. The pump increases or decreases the absorption signal intensity depending on whether $k_{\bar{\Phi}} < k_{\chi}$ or $k_{\bar{\Phi}} > k_{\chi}$. Here, k denotes the rate constant for the process.

experiments was developed by Davis and Green (10,12,13,14). Green began the theoretical studies by using the electron gas model which was created by Gordon and Kim (15). In this study the ammonia molecule was treated as a rigid top.

Davis and Boggs extended this work by using Green's theory with classical path calculations to obtain degeneracy averaged cross sections for the NH₃-He collisions as a function of energy of collision. Then, a Boltzmann average over the collisional energy was performed to determine rate constants at room temperature, from which the $\Delta I/I$ value was determined. The calculated $\Delta I/I$ values were found to be in poor agreement with the experimental results (4).

Other changes to the theory were made by Davis, Boggs and Mehrota (10,16,17,18). These results were still found to give mixed agreement with the experiments. Green then introduced a Hartree-Fock potential modified by the addition of long-range dispersion and induction contributions. When this improvement did not help much, Davis and Green included in their calculation the m-dependence of the cross sections for NH₃-He collisions (10), which also did not change things very much and which led to the statement quoted above. At this point we began, at the instigation of T. Oka, a series of experiments to check the experimental measurements performed in Oka's Laboratory.

G. D. Billing, L. L. Poulsen and H. F. Diercksen in

1985 performed an elegant series of calculations on both the NH₃-He and NH₃-H₂ systems (11,18). Both of these calculations were done by ab initio self-consistent-field (SCF) methods. The main difference between these calculations and those carried out by Davis and Green is the potential function used for the collisional interaction. The results obtained by this method are in much better agreement with the experimental data reported by Oka, and verified by our work, and with some infrared laser microwave double resonance results reported by Das and Townes (7). Table 2.1 presents a comparison of the calculated results of Davis and Green (10); Billing, Poulsen and Diercksen (18); with the experimental results of Oka (1-4), for the NH₃-He gas mixture. Table 2.2 compares the calculated and experimental results for the NH₃-H₂ system.

Table 2.1. Comparison of calculated and experimental values of four-level double resonance effects in NH_3 -He mixtures.

Observed ΔI/I ^b Oka ^e	Calculated $\Delta I/I^b$		Transition ^a	
	Billing et al.d	Davis ^C	Signal	Pump
-3.5	-8.8	22	(2,1)	(1,1)
-10.0	-5.2	-12	(2,2)	
-2.8	-4.5	3	(3,1)	
0.0	3.2	5	(3,2)	
-3.0	0.7	-1	(2,1)	(2,2)
-4.2	-5.3	14	(3,2)	
-0.3	1.5	3	(3,1)	
\2.5	5.6	14	(3,1)	(2,1)
-5.0	-5.9	-7	(3,2)	
4.4	7.9		(4,1)	(3,1)
-5.0	-5.5		(4,2)	
-0.6	1.3		(4,4)	
-2.5	-2.9		(3,1)	(3,2)
0.0	0.6		(4,1)	•
0.0	-2.4		(4,2)	

^a The pump and signal transitions are between the inversion doublets for the level (J,K).

 $^{^{}b}$ $\Delta I/I$ = (Ipumped - Iunpumped)/ Iunpumped where the I's are proportional to the absorption of the radiation.

c Reference (10)

d Reference (18)

e References (4,6)

Table 2.2. Comparison of calculated and experimental values of four-level double resonance effects in $\rm NH_3^{-H}_2$ mixtures.

Observed \Delta I/I	Calculated $\Delta I/I^b$	Transition ^a	
Oka ^e	Billing and Diercksen ^d	ımp Signal	
+5.2	+	(1,1)	(2,1)
-0.6	-	(3,2)	` ' '
-3.0	<u>-</u>	(1,1)	(2,2)
-2.6	-	(1,1)	
+11.2	+	(2,1)	(-,-,
+0.5	+	(1,1)	(3,2)
+2.3	+	(2,2)	(-,-,
-2.4	-	(2,1)	(4.1)
+8.3	+	(3,1)	(-,-,
+4.2	• +	(3,2)	(4,2)
-1.9	<u>.</u>	(1,1)	
-1.1	-	(2,1)	(- , -)

^a The pump and signal transitions are between the inversion doublets for the level (J,K).

^b Sign of $\Delta I/I$ calculated ratio.

 $^{^{\}text{C}}$ $\Delta\text{I}/\text{I}$ = (Ipumped - Iunpumped)/ Iunpumped where the I's are proportional to the absorption of the radiation.

d Reference (11)

e References (5,6)

2.3 Experimental

The four-level microwave-microwave double resonance experiment was introduced by Oka and his co-workers, and the method and their results are summarized in References (1-6). In order to test the validity of the experimental data, we repeated many of the four-level double resonance measurements on these systems. In our apparatus, which differs somewhat from that used previously, a phase-locked Hewlett-Packard (HP) 8690B backward wave oscillator (BWO) served as the low-power signal radiation source, whereas a phase-locked OKI 24V11 K-band klystron served as the pump source. The experimental set-up is shown in Figure 2.2.

The BWO was frequency locked by using a HP model 8709A synchronous detector and a HP 8455A reference oscillator. The klystron was locked by means of a Microwave Systems MOS5 phase lock system. Radiation from the pump, whose frequency was always lower than that of the signal source, was prevented from reaching the detector by means of a slotted piece of waveguide which could be squeezed until the longer dimension was just below the cut-off point for the pump frequency.

The sample cell was a standard X-band waveguide Stark cell and the detector response to the signal radiation was processed at the Stark modulation frequency (33.3 kHz) by

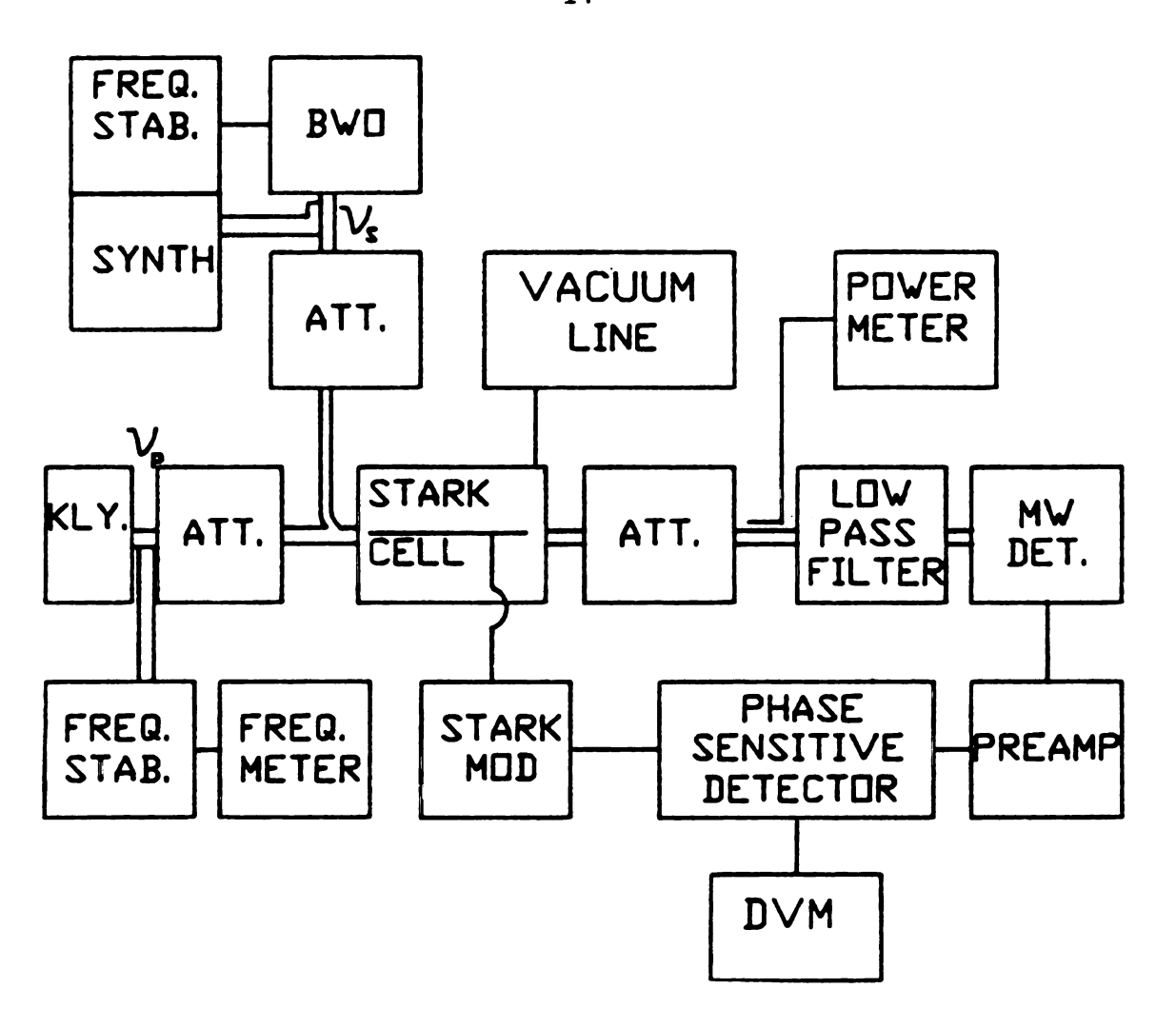


Figure 2.2. Block diagram of microwave-microwave four-level double resonance spectrometer.

monitored by a digital voltmeter (DVM). After determining that both the pump and signal sources were locked at the appropriate resonance frequencies, the low-pass filter was checked to be sure that no pump signal reached the detector. The DVM zero was determined by reducing the signal power to near zero and recording the DVM voltage. Then, the signal was returned to a predetermined level and the DVM output was recorded with the pump power at its highest value and at 40db below its highest value. The system was tested for spurious responses by noting no change in the PSD output when the pump frequency was deliberately tuned off resonance.

The NH₃ gas was a specially purified sample obtained from J. L. Dye of Michigan State University. The He was a 99.99% pure commercial gas. The sample mixtures were prepared by mixing ~5 Torr of NH₃ and ~500 Torr of He into one sample bulb and ~5 Torr of NH₃ and ~500 Torr of H₂ into another sample bulb. Since NH₃ strongly adsorbs on the walls of our microwave sample cell, the actual gas ratios in the cell at the time of measurement were probably smaller than 1/100. The total pressure in the sample cell was typically 70-80 mTorr for both samples. All measurements were carried out at room temperature (~297 K).

In order to determine whether the pumping source used

(OKI 24V11 klystron) had sufficient power to saturate a transition, the pump was used as a source for a one photon experiment. Attenuators before and after the sample cell were manipulated in such a way that the microwave power inside the cell could be changed without changing the power at the microwave detector. The resulting absorption vs. power plot is shown in Figure 2.3. The results of this plot show that the pumping transition could be brought to within 1-2% of complete saturation at the highest powers.

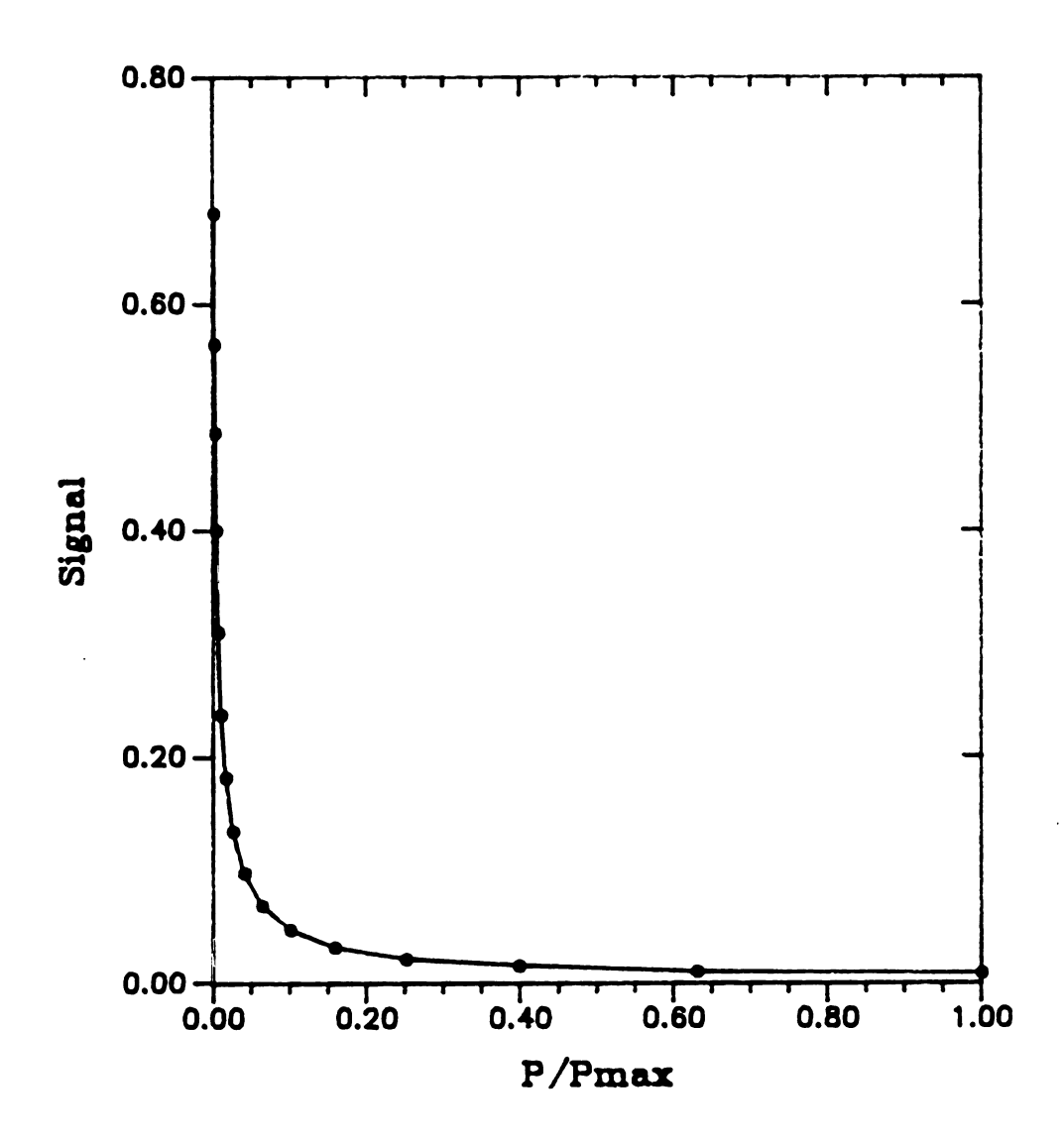


Figure 2.3. Plot of microwave detector signal vs.

power/max. power. Attenuators before and after the sample

cell were manipulated in such a way that the microwave power

inside the cell could be changed without changing the power

at the detector. The results of this plot show that the

pumping transition could be brought to within 1-2% of

complete saturation at the highest powers.

2.4 Results

The values of $\Delta I/I$ for the NH_2 -He mixture are compared to the previously reported values in Table 2.3 and for the NH2-H2 mixture in Table 2.4. Although there are some minor differences between the present and previous results, the overall agreement is very good, especially given the variation in instrumental arrangement and sample pressure in the two experiments. In Oka's experiments two klystrons were used to generate the microwave frequencies for the pump and signal radiations. The high microwave power was passed through a K-band Stark modulation cell in the opposite direction of the signal microwave radiation, whereas we used the low-pass filter to prevent the pumping radiation from reaching the detector. The results show that the $\Delta I/I$ ratios are small unless the k values in the pump and signal transitions are the same or differ by ±3. There is no indication at all of any problem with the previous experimental work that could explain the differences between observed and calculated AI/I values. By confirming the experimental values of $\Delta I/I$ by Oka and co-workers, the present data confirm the recent suggestion by Billing et al. that the source of the original discrepancies between theory and experiment are mainly the result of an inadequate potential function for collisions of NH, with He or H,.

Table 2.3. Four-level double resonance effects in NH_3 - He.

Transition ^a		ΔI/I ^b		Transition ^a		ΔI/I ^b	
Pump	Signal	Oka ^C P	eterson	Pump	Signal	<u>Oka</u> ^C	Peterson
(1,1)	(5,5)	-0.6	-1.0	(5,4)	(4,4)	0.0	0.0
	(7,7)	0.0	-0.6		(5,5)	0.0	0.3
(2,1)	(1,1)	-3.5	-5.2		(7,7)	0.2	0.3
	(2,2)	-3.0	-3.4		(8,7)	-1.3	-2.9
	(3,3)	0.0	0.0		(8,8)	0.0	
	(4,4)	-3.2	-2.7	(0.0)	(9,8)		0.4
	(5,5)	-0.3	-0.5	(6,5)	(1,1)	0.6	0.5
	(7,7)	0.0	0.5		(2,2)	1.7	1.5
	(9,8)		0.1		(3,3)	0.0	0.4
(2,2)	(5,5)	-3.9	-4.1		(4,4)	0.0	0.3
	(7,7)	0.0	-0.4		(5,5)	1.1	1.6
(3,2)	(1,1)	0.0	0.4		(7,7)	0.0	0.2
	(2,2)	-4.2	-3.2		(8,7)		-0.4
	(3,3)	0.0	0.3		(8,8)	0.0	
	(4,4)	-1.0	-0.3		(9,8)	-2.2	-2.8
	(5,5)	-2.5	-1.3	(7,6)	(1,1)	0.0	0.2
	(7,7)	0.0	0.5		(2,2)	0.0	-2.5
	(9,8)		0.1		(3,3)	1.1	0.9
(3,3)	(6,6)	-2.9			(4,4)	0.0	0.1
(4,3)	(1,1)	0.0	0.5		(5,5)	0.0	0.5
	(2,1)		-0.5		(6,6)	1.0	1.2
	(2,2)	0.0	0.0		(7,7)	0.0	0.4
	(3,3)	-2.2	-2.5		(9,8)		0.6
	(4,4)	0.0	0.0		(10,9)	-1.9	-1.7
	(5,5)	0.0	0.4	(8,7)	(3,3)	0.0	0.0
	(6,6)	-1.1	-0.9		(4,4)	0.0	0.3
	(7,7)	0.0	0.0		(5,5)	0.0	0.1
	(8,7)	0.0	-2.4		(7,7)	0.8	1.6
	(9,8)		0.8		(8,8)	0.0	
(5,4)	(1,1)	2.0	1.9	(9,8)	(5,5)	-0.3	-0.1
	(2,1)		-1.3		(7,7)	0.0	-0.2
	(2,2)	0.6	0.0		(8,8)	1.3	
	(3,3)	0.0	0.0				

The pump and signal transitions are between the inversion doublets for the level (J,K). $\Delta I/I = (Ipumped - Iunpumped) / Iunpumped where the I's are proportional to the absorption of the radiation. References <math>(4,6)$

Table 2.4. Four-level double resonance effects in NH_3-H_2 .

Transition ^a		$\Delta I/I^{b}$		Transition ^a		$\Delta I / I^{\mathbf{b}}$	
Pump	Signal	<u>Oka</u> ^C	Peterson	Pump	Signal	Oka ^C	Peterson
(1,1)	(5,5)	0.0	0.0		(3,3)		-0.4
	(7,7)		0.0		(4,4)	0.0	-0.3
(2,1)	(1,1)	5.2	8.4		(5,5)		0.5
	(2,2)	0.0	-2.3		(6,6)		0.0
	(3,3)		-0.3		(7,7)		0.3
	(4,4)	0.0	0.6		(8,7)		-1.0
	(5,5)	0.0	0.0	(6,5)	(1,1)	0.0	0.3
	(7,7)		0.0		(2,2)		-0.7
	(9,8)		0.2		(3,3)		0.1
(2,2)	(5,5)	0.0	-1.0		(4,4)	0.0	0.1
	(7,7)		0.0		(5,5)	0.0	0.4
(3,2)	(1,1)	0.5	0.4		(7,7)		0.0
	(2,2)	2.3	1.8		(8,7)		-2.7
	(3,3)		0.0		(9,8)		-0.9
	(4,4)	0.0	-0.1	(7,6)	(1,1)		0.2
	(5,5)	0.0	-0.2		(2,2)		-1.2
	(7,7)		-0.1		(3,3)	0.0	0.2
	(9,8)		0.3		(4,4)		-0.1
(4,3)	(1,1)		0.3		(5,5)		0.3
	(2,2)		-0.7		(7,7)		0.5
	(3,3)	0.0	0.0		(9,8)		0.2
	(4,4)		0.0	(8,7)	(3,3)		0.0
	(5,5)		-0.1		(4,4)		-0.1
	(7,7)		0.0		(5,5)		0.0
	(8,7)		-3.0		(7,7)		-0.1
	(9,8)		0.3	(9,8)	(5,5)		0.3
(5,4)	(1,1)	0.4	0.7		(7,7)		-0.2
	(2,2)	0.0	-0.3				

The pump and signal transitions are between the inversion doublets for the level (J,K).
ΔI/I = (Ipumped - Iunpumped)/ Iunpumped where the I's are proportional to the absorption of the radiation.
References (5,6).

theoretical work recently done by Billing et al. shows a much closer correlation to the experimental results than the previous theoretical studies. Another experiment performed by Townes and Das also gave similar results. It is, therefore, our conclusion that the reported data in this and previous work by Oka et al. are consistent.

2.5 References

- 1. T. Oka, J. Chem. Phys. 47, 13 (1967).
- 2. T. Oka, J. Chem. Phys. 47, 4852 (1967).
- 3. T. Oka, J. Chem. Phys. 48, 4919 (1968).
- 4. T. Oka, J. Chem. Phys. 49, 3135 (1968).
- 5. P. W. Daly and T. Oka, J. Chem. Phys. 53, 3272 (1970).
- 6. A. R. Fabris and T. Oka, J. Chem. Phys. <u>56</u>, 3168 (1972).
- A. Das and C. H. Townes, J. Chem. Phys. <u>85</u>, 179 (1986);
 A. Das, Ph. D. Thesis, University of California at Berkeley, 1985.
- N. Morita, S. Kano and T. Shimizu, J. Chem. Phys. <u>68</u>, 3897 (1978).
- 9. A. C. Cheung, D. M. Rank, C. H. Townes, S. H. Knowels, and W. T. Sullivan III, Astrophys, J. 157, L13 (1969).
- S. L. Davis and S. Green, J. Chem. Phys. <u>78</u>, 2170
 (1983).
- G. D. Billing and G. H. F. Diercksen, Chem. Phys. <u>105</u>,
 145 (1986).
- 12. S. Green, J. Chem. Phys. <u>64</u>, 3463 (1976).
- 13. S. L. Davis and J. E. Boggs, J. Chem. Phys. <u>69</u>, 2355 (1978).
- 14. S. Green, J. Chem. Phys. <u>73</u>, 2740 (1980).
- 15. R. G. Gordon and Y. S. Kim, J. Chem. Phys. <u>56</u>, 3122 (1972).

- S. L. Davis and J. R. Boggs, J. Chem. Phys. <u>75</u>, 3937
 (1981).
- 17. S. L. Davis, J. E. Boggs and S. C. Mehrota, J. Chem. Phys. <u>71</u>, 1418 (1979).
- 18. G. D. Billing, L. L. Poulsen and G. H. F. Diercksen, Chem. Phys. 98, 397(1985).
- D. B. Peterson and R. H. Schwendeman, J. Chem. Phys. 86, 7241 (1987).

CHAPTER III

Infrared-Microwave Double Resonance Using a Fourier Transform Infrared Spectrometer

3.1 Introduction

Infrared-microwave double resonance experiments have been carried out by a number of different laboratories (1-5). However all of these experiments have used an infrared source with a large enough power to saturate, at least partially, a molecular transition. The effect of the infrared radiation is to change the populations of pumped transitions, which can be easily observed. With this technique both three-level and four-level double resonance effects can be seen.

The first reproducible work done by means of the infrared-microwave double resonance technique was reported by T. Shimizu and T. Oka in 1970 (6). They used an N_2 0 laser to pump the ν_2 [q Q (8,7)] transition of 14 NH $_3$ and studied the effect of the pumping on ground state inversion transitions that were observed with a K-band microwave source and standard Stark modulation. The results showed that there was a large effect on the populations of the inversion energy levels directly pumped by the laser

radiation and a smaller effect on the populations of other levels through collisions. After this work, many papers that described applications of the technique of infrared-microwave double resonance were published.

A different approach was used by H. Jones and F. Kohler (2) to pump with infrared radiation and observe assigned ground state transitions with microwave radiation. They put the microwave cell inside the laser cavity and studied the effects on the laser output of tuning the microwaves through resonances. By noting the effects of rotational transitions in the lower and upper levels of the infrared transition, assignments could be made for the vibration-rotation states pumped by the infrared. Only rather weak microwave power was needed to obtain strong effects. This technique was used to assign some vibration-rotation transitions in the CF₃I molecule. More will be said about this in Chapter 5.

The most prolific researcher in the field of infraredmicrowave double resonance has been M. Takami with a number
of collaborators (5,7-9). In addition to a variety of
experimental work, he has published a definitive theory of
double resonance. His work is the closest to ours in that
the infrared radiation is weak and the microwave radiation
is stronger. However, his experiments still use partial
saturation of the infrared transitions. Takami also detects

the effect on the microwave radiation, even though with his experiments it is not clear which radiation source is the pump and which is the signal due to their comparable strengths.

With this brief history of the technique and its applications I would now like to describe the double resonance experiments we performed. In the first series of experiments, the radiation source used for the infrared light was a Fourier transform infrared spectrometer. In this case, the infrared radiation was obviously very weak and therefore a very strong microwave source was used. We hoped to see an effect on the infrared (vibrational) absorption that is known as "coherency splitting" or "high-frequency Stark effect"; this splitting will be discussed in the next section.

The rationale for the infrared-microwave double resonance experiments described in this thesis has been to try to exploit the advantages of microwave pumping with a tunable infrared source. The main advantage of this technique is that rotational spectra in the ground state have been assigned and are well understood for many molecules. Therefore, the pumped transitions are well known and then the vibrational transitions affected by three-level double resonance can be easily assigned. A second advantage of this technique is that the spectral complexity of the

vibrational band is greatly decreased if only the vibrational transitions in coincidence with the ground state pumped levels are affected. This can then lead to a very small number of transitions if a modulation scheme is used. The final advantage mentioned here is the fact that by using a widely tunable microwave and infrared source, there is no problem with finding a coincidental overlap of a transition and a laser line.

In the following sections the theory of the double resonance phenomenon will be discussed along with an explanation of an experiment employing a Fourier transform infrared spectrometer and an amplified microwave source.

Some results will be shown and conclusions about the experiment will also be given.

3.2 Theory

Coherence Splitting

As stated above, the effects seen by previous authors of infrared-microwave double resonance experiments are the results of changes in population. The population effect for an infrared transition is much larger than that for a microwave transition because of the difference in energy of the two levels involved. According to the Boltzmann distribution, the population ratio of the upper and lower energy states of a transition is calculated by the following equation.

$$N_2/N_1 = \exp(-h\nu_{12}/kT)$$
 (3.1)

If the transition is in the infrared region of ~1000 cm⁻¹, the ratio is 0.007, but for a transition in the microwave region of ~15 GHz, the ratio is 0.997. Since the populations can at most be equalized by steady-state radiation, the population effect on saturation of an infrared transition can be very large, whereas the population effect for a microwave transition is necessarily very small.

Since the population change is so small for the

microwave pump, another effect must be present to observe an infrared-microwave double resonance signal. The phenomenon observed when using a strong microwave pump is called coherence splitting. This splitting effect is created only with very large radiation powers. The splitting was first calculated by Javan (10).

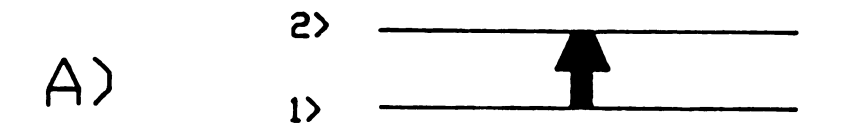
For the following explanation let us consider a twolevel system first. When a two level system is irradiated with coherent radiation, the wave functions of the two separate states are combined linearly in a time coherent manner (10). If the radiation is resonant with the energy level difference in the two level system as shown in Figure 3.1(A) the combination takes the form,

$$\Psi_1(t) = \Psi_1(t) \cos(\omega_0 t/2) + i\Psi_2(t) \sin(\omega_0 t/2)$$
 (3.2)

$$\Psi_2(t) = \Psi_2(t) \cos(\omega_0 t/2) - i\Psi_1(t)\sin(\omega_0 t/2)$$
 (3.3)

where $\Psi_1(t)$ and $\Psi_2(t)$ represent the normalized "stationary states" but time-dependent wave functions of states |1> and |2> in the absence of radiation. The factor ω_0 is the angular frequency, which is related to the transition matrix element $|\mu_{12}|$ between the two states as shown by

$$\omega_0/2\pi = |\mu_{12}| E/h = \nu_0.$$
 (3.4)



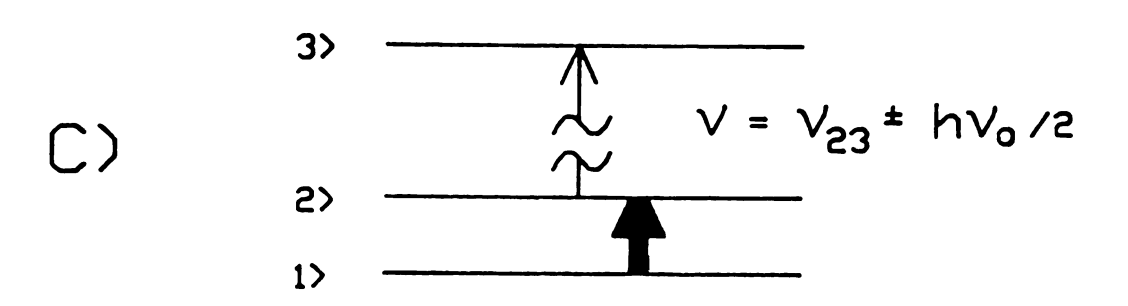


Figure 3.1 Energy level diagram for single and double resonance.

This quantity ν_0 is commonly known as the Rabi frequency. The important outcome of Equations (3.1) and (3.2) is that the system nutates between two possible states at a frequency ν_0 (the Rabi frequency) without ever being in either state for any prolonged amount of time.

Now let us consider how this nutation affects the double resonance phenomenon. We will do this in a simple, quantitative way that can be verified by more complex calculation. To begin, we introduce a third level |3> as shown in Figure 3.1(B). If we look at the time-dependent wavefunctions for states |2> and |3> in the absence of radiation, we get the following:

$$\Psi_2(t) = \Psi_2(r) \exp(-iR_2 t/h) \qquad (3.5)$$

and

$$\Psi_3(t) = \Psi_3(r) \exp(-i\mathbb{E}_3 t/h) \tag{3.6}$$

The normal linear transition between states $|2\rangle$ and $|3\rangle$ involves the time-dependent part of the wave functions and its frequency ν_{23} can be shown to obey the Bohr frequency condition,

$$h_{\nu_{23}} = E_3 - E_2$$
 (3.7)

Now, with the application of the pumping radiation resonant with the $|1\rangle \rightarrow |2\rangle$ transition we obtain a wave function for $|2\rangle$ of the form in Equation (3.2). If we assume that transitions between $|1\rangle$ and $|3\rangle$ are forbidden, the Ψ_1 part may be ignored so we get an equation of the form.

$$\Psi_2(t) = \Psi_2(t)\cos(\omega_0 t/2).$$
 (3.8)

If this is expanded in exponential form,

$$Ψ_2(t) = Ψ_2(r) \exp(-iR_2t/\hbar)(\exp(iω_0t/2))/2$$
 (3.9)
+ $Ψ_2(r) \exp(-iR_2t/\hbar)\exp(-iω_0t/2)/2$,

Which can be further simplified to

$$\Psi_{2}(t) = 1/2\Psi_{2}(r) \exp(-i(E_{2} - h\nu_{0}/2)t/\hbar) +$$

$$1/2\Psi_{2}(r) \exp(-i(E_{2} + h\nu_{0}/2)t/\hbar)$$
(3.10)

Then, a splitting occurs when the frequency is calculated for the $|2\rangle \rightarrow |3\rangle$ transition.

$$v(\pm) = v_{23} \pm v_0/2$$
 (3.11)

From this result we can see that the normal one photon

transition between states $|2\rangle$ and $|3\rangle$ is split into two transitions if there is a coincidence between the frequency of strong pumping radiation and states $|1\rangle$ and $|2\rangle$. Equation (3.11) shows that the coherence splitting is equal to the Rabi frequency ν_0 .

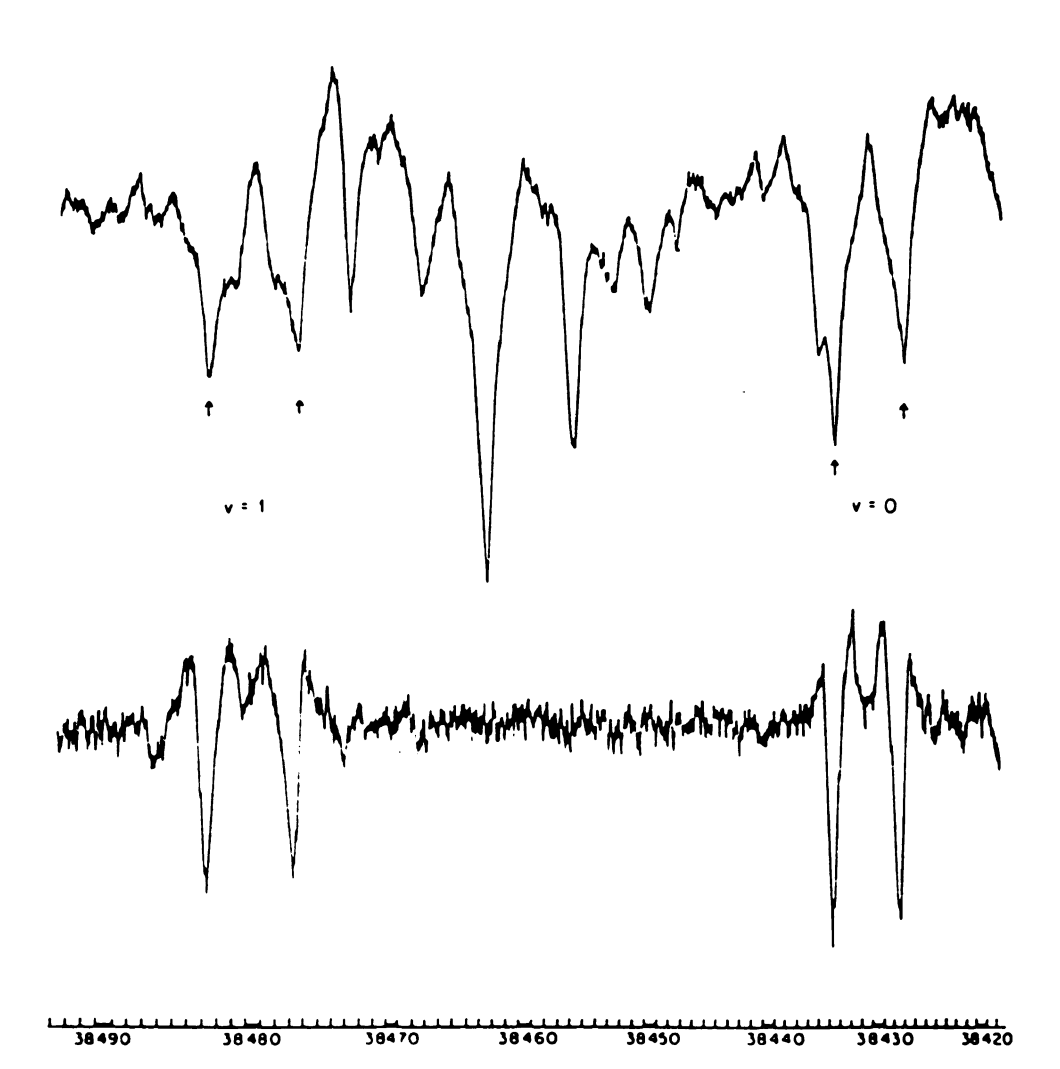
The coherence splitting has been used in observations of microwave-microwave and also radiofrequency-microwave double resonance experiments. Our interest in this phenomenon and the development of it for an infrared-microwave experiment came from the work of Wodarczyk and Wilson (11). They described a spectrometer in which a radiofrequency pump was used to modulate and thus assign microwave transitions. By using the double resonance method a spectrum could be simplified as shown in Figure 3.2. This then makes the assignment much simpler. We were interested in using this same idea to simplify infrared spectra. To do this a tunable high resolution infrared source was needed, and a Fourier transform infrared spectrometer was a logical choice.

Fourier Transform Spectroscopy

The Fourier transform infrared (FTIR) spectrometer was first developed by A. A. Michelson in 1881 (12). The diagram of a Michelson interferometer is shown in Figure

Figure 3.2 An example of the use of radio frequency microwave double resonance (RFMDR) to simplify spectra. The upper trace is a portion of the normal Stark modulated microwave spectrum of ethyl formate. The lower trace is the RFMDR spectrum in the same region with the radio frequency pump coincident with a transition. Only the three level resonances in the ground (v=0) and first excited state (v=1) appear strongly in the spectrum. The simplification in the RFMDR spectrum is evident (from Wodarczyk and Wilson, (ll)).





3.3. The polychromatic source radiation passes through an aperture and is separated into two beams by a beamsplitter. One beam is directed to a stationary mirror, while the other beam is sent to a movable mirror. The two beams are then reflected back to the beamsplitter, through the sample, and finally to the detector. The two reunited beams interfere constructively or destructively, depending on the path difference and the wavelength of the light.

The signal at the detector is a function of path difference (x) and is known as an interferogram. The interferogram can be described by,

$$I(x) - I(0)/2 = \sum B(\nu_k) \cos(2\pi \nu_k x).$$
 (3.12)

Here, ν_k is the wavenumber of the kth radiation, $B(\nu_k)$ is the intensity of the source at $\nu = \nu_k$, and I(x) is proportional to the intensity of the light leaving the interferometer for a path difference x. If we assume a continuous source of radiation with $B(\nu)d\nu$ equal to the intensity between ν and ν + $d\nu$, then

$$I(x) - I(0)/2 = \int_{0}^{+\infty} B(\nu) \cos(2\pi\nu x) d\nu$$
 (3.13)

This equation is part of a cosine Fourier transform pair, so that

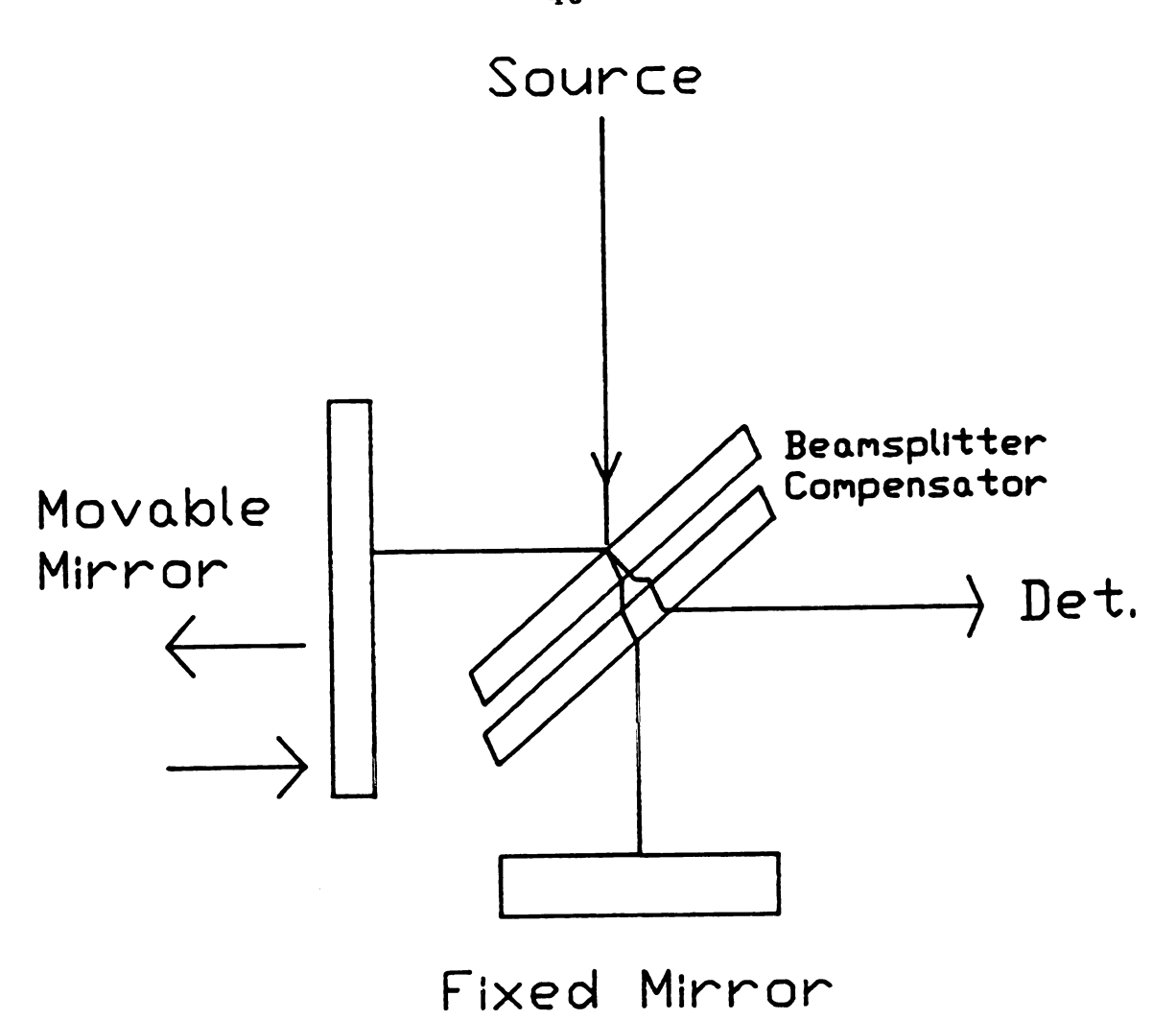


Figure 3.3 Diagram of a Michelson interferometer.

$$B(\nu) = \frac{2}{\pi} \int_{0}^{+\infty} [I(x) - I(0)/2] \cos(2\pi x \nu) dx \qquad (3.14)$$

These last two equations define the relationship between the interferogram and the normal frequency domain spectrum. A typical interferogram and its normal spectrum is shown in Figures 3.4 and 3.5 respectively. The most important criterion for the success of this experiment is the resolution available for the infrared source. The resolution can be written as a function of path difference, as follows:

$$Res(cm^{-1}) = \frac{1}{2\Delta x} \tag{3.15}$$

where Δx is the maximum path difference (in cm). For example, in our instrument the maximum possible difference is 50 cm, which corresponds to a maximum resolution of 0.01 cm⁻¹. Thus, by using an interferometer arrangement instead of a scanning spectrometer we can obtain the spectrum all at once and at a higher resolution than available with a normal grating instrument.

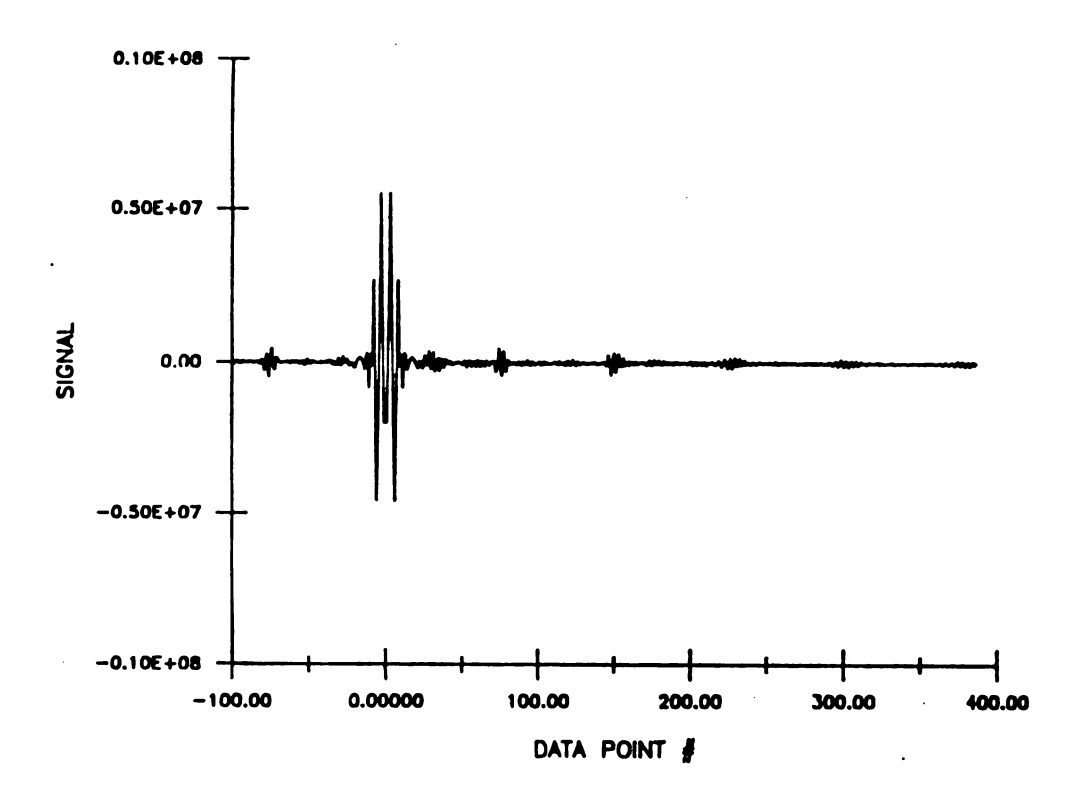


Figure 3.4 Interferogram taken by a BOMEM DA3.01 FTIR of ${
m CH_3F}$ at 0.02 cm $^{-1}$ resolution.

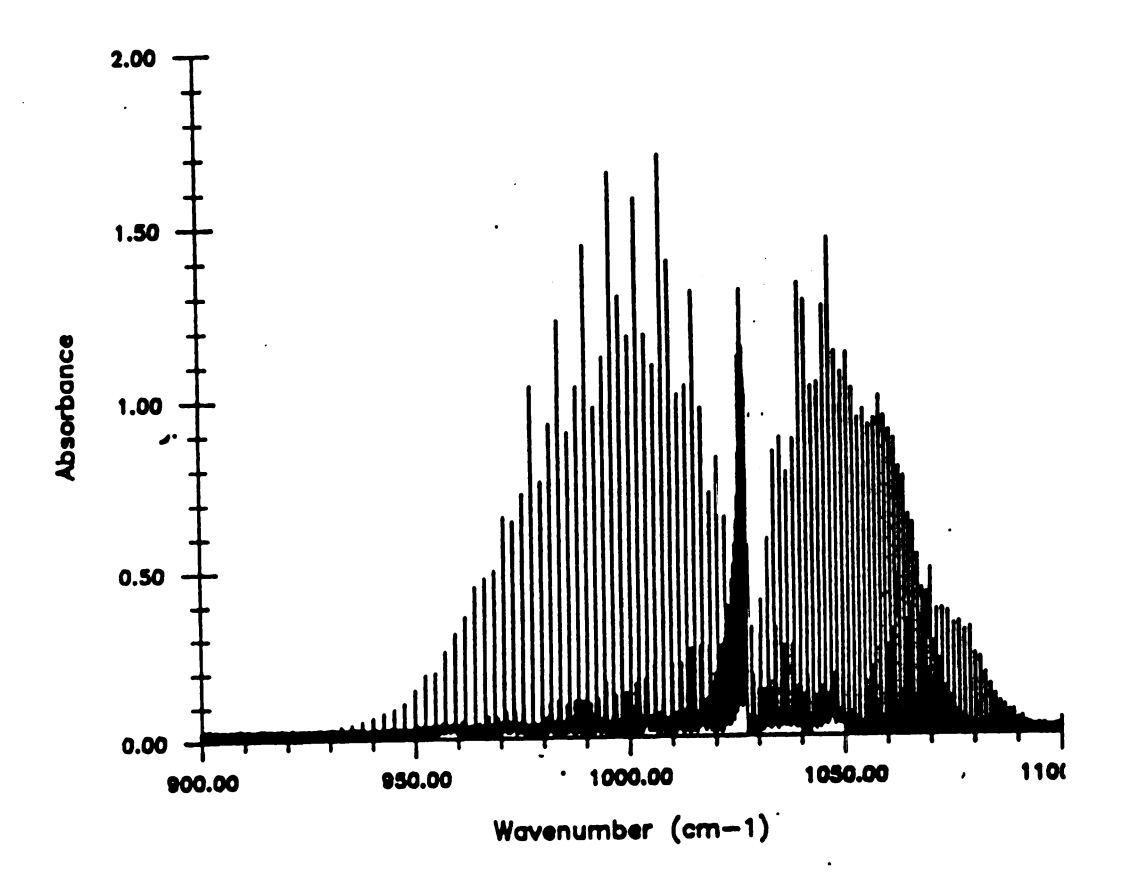


Figure 3.5 Spectrum calculated from interferogram of ${
m CH_3F}$ at 0.02 cm $^{-1}$ resolution.

3.3 Experiment

As mentioned above, our first infrared microwave double resonance experiment utilized a strong microwave source for the pumping radiation and a FTIR spectrometer for the infrared signal radiation. The observed double-resonance should then be the effect of the microwave pump on the infrared transitions that share a common level with the microwave transition. To see this effect the microwaves were chopped at 100 kHz and the infrared signal was processed by a lock-in amplifier at the chopping frequency. A block diagram of the set-up is displayed in Figure 3.6.

Instrumentation

The FTIR spectrometer used for the double resonance experiment was a BOMEM model DA3.01. The infrared source was a water cooled Globar, which is a good polychromatic source in the mid-infrared region. The beam of light is first focused by an off-axis ellipsoid mirror onto an iris. The beam then passes to a flat mirror after which it is recollimated by a f/4 paraboloid mirror; the optical diagram is shown in Figure 3.7. The recollimated light is then sent through the Michelson interferometer, which is a KBr beamsplitter and two flat mirrors, and which has a maximum

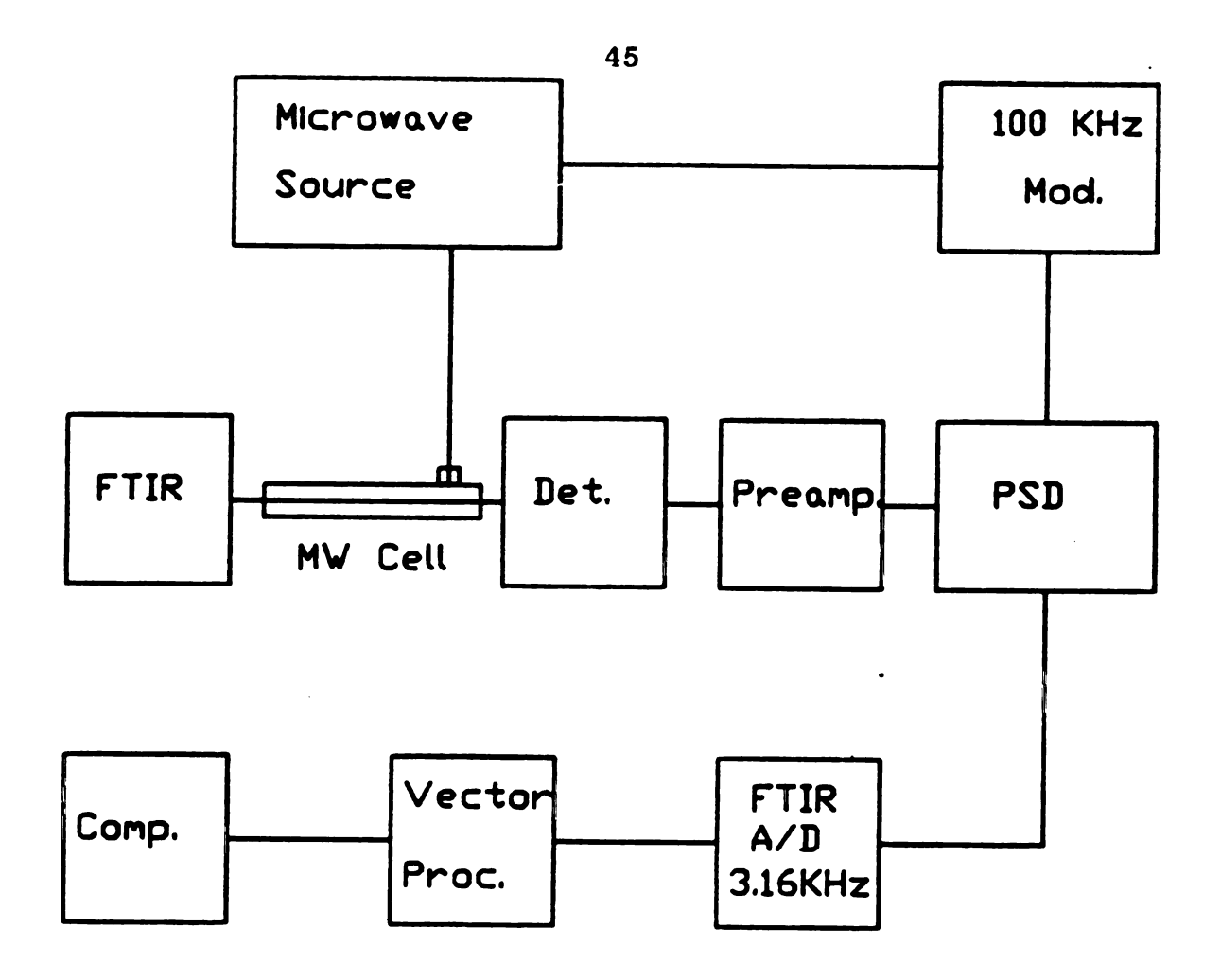


Figure 3.6 Block diagram of FTIR-microwave double resonance spectrometer.

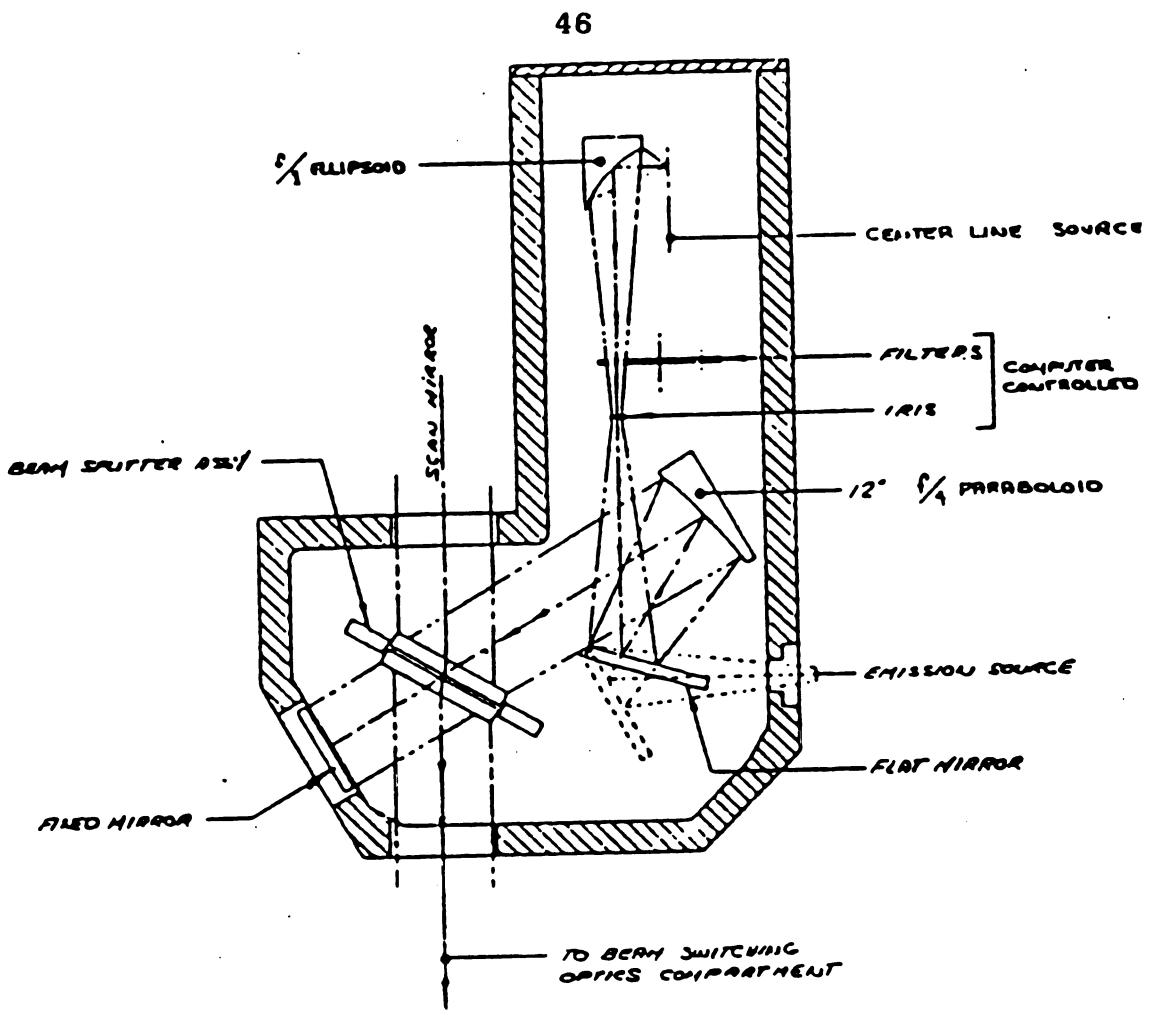


Figure 3.7 Diagram of optical components in BOMEM DA3.01 FTIR spectrometer.

path difference of 50.0 cm. Upon recombination, the beam is condensed and sent through a sample cell and finally focused on the detector. The detector used was a liquid-N₂ cooled mercury cadmium telluride photoconductive detector, manufactured by Infrared Associates. The signal from the matched preamplifier was coherently detected at 100 kHz by a Stanford Research Systems SR510 lock-in amplifier. The output of the lock-in amplifier was sent to the analog to digital converter board on the BOMEM instrument where it was sampled at a rate of 3.16 kHz.

The sample used was NH_3 at a pressure of 300 mtorr. The path length of the cell was 12 inches. The NH_3 sample was an ultra pure sample obtained from Dr. J. L. Dye. Ammonia was selected for the sample because it is a symmetric top with inversion doublets that give strong microwave transitions in the 8 to 26 GHz range. Ammonia was also picked because the ν_2 band is well understood, so that predictions of the frequency of the expected double resonance signals could be made easily.

The diameter of the infrared beam from the interferometer was reduced by a Cassegrain mirror assembly. The reason for this was to increase the field strength of the infrared radiation and still keep the beam collimated.

A more detailed diagram of this apparatus is shown in Figure 3.8. The shadow of the small mirror had essentially no

effect on the infrared beam because a shadow, 2.5 cm in diameter, in the center of the beamsplitter already exists from the center quartz beamsplitter piece. The mount was designed to be flexible in the Z axis as shown and an ability to tilt the mirrors was also available. With the Cassegrain mirror arrangement the beam was condensed and recollimated from 9 cm to 2.5 cm with very little loss.

As mentioned earlier, the splitting of the pumped energy levels is dependent on the electric field of the radiation. Because of the large Doppler width of the NH₃ molecule under study (~35 MHz HWHM), the Rabi frequency needs to be of the order of 35 MHz. The microwave radiation was generated by a backward wave oscillator and amplified by a travelling wave tube amplifier (TWTA). With this apparatus, the microwave power output is ~20 Watts.

To increase the microwave electric field inside the sample cell a microwave cavity cell was constructed from a design used by J. Asmussen (13). The cell is made of brass and shown in detail in Figure 3.9. Since the cell had to be able to work from 8-18 GHz, it was designed so that the length of the cell could be adjusted at one end. This arrangement allows the cell to operate as a microwave cavity over the entire range desired. Another degree of freedom was needed for the antenna connection to the cell in order to provide the correct coupling between the SMA connector

Cassegrain Mirror Setup

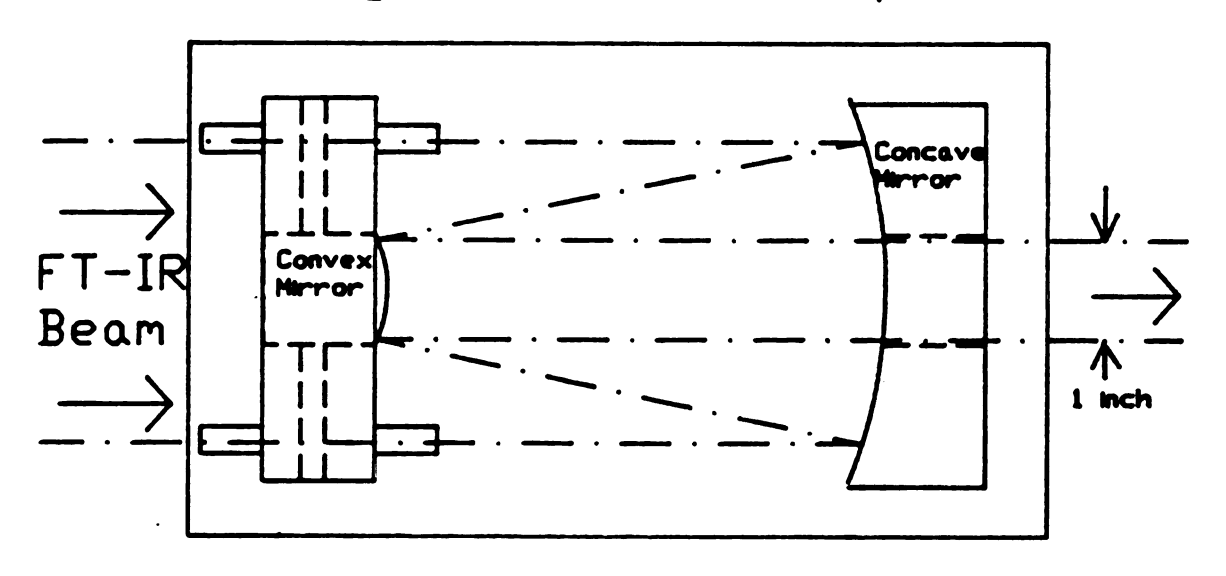


Figure 3.8 Diagram of the Cassegrain mirror arrangement used to reduce the diameter of the infrared beam from the BOMEM interferometer.

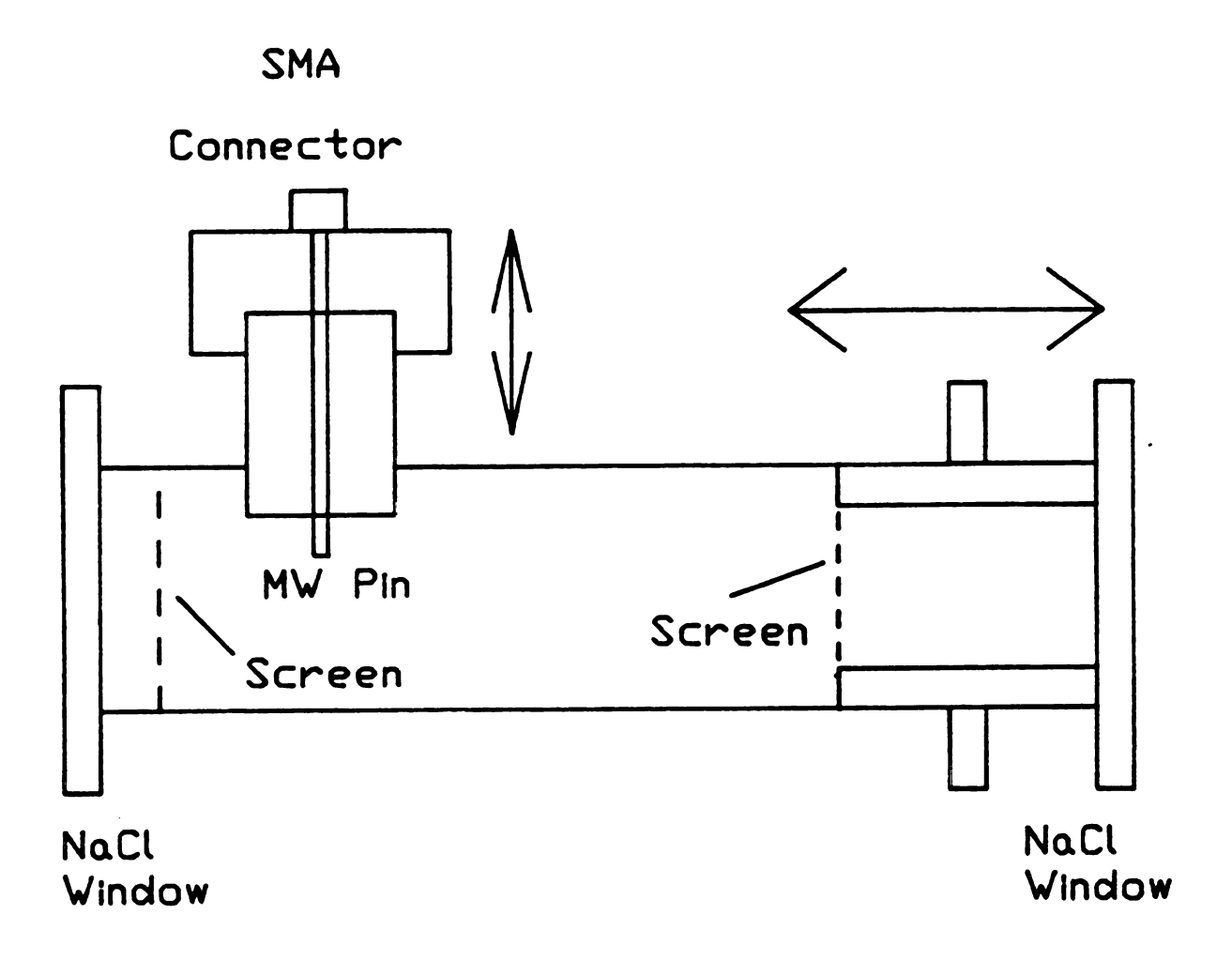


Figure 3.9 Diagram of microwave cavity cell used in double resonance experiment.

and the cell. For this purpose, the coupling antenna can be screwed in or out through a vacuum connection. The ends of the cell consist of NaCl windows for infrared transmittance; however, the microwaves are shorted at the windows by gold plated fine tungsten wire screens each of which transmits 81% of the infrared radiation. The microwave cell is also vacuum tight with a total path length of ~ 12 inches.

The mode condition inside the cell is also of interest because each mode has a different structure. Diagrams of the electro-magnetic fields of different modes inside a cylindrical waveguide are shown in Figure 3.10 (14). This diagram shows how drastic the differences are. A calculation was done for ten possible modes inside the cavity. The equation used to calculate the resonance wavelengths was the following:

$$\lambda_0 = \sqrt{(2/z_0)^2 + (2\mu_m, n/\pi a)^2}$$
 (3.16)

Here, I is an integer that gives the number of half waves along the axis of the resonator, z_0 is the half length of the resonator cavity, a is the radius of the cavity, and $\mu_{m,n}$ is the nth root of an mth order Bessel function which determines the axial field. A list of the first ten roots is given in Table 3.1 (14).

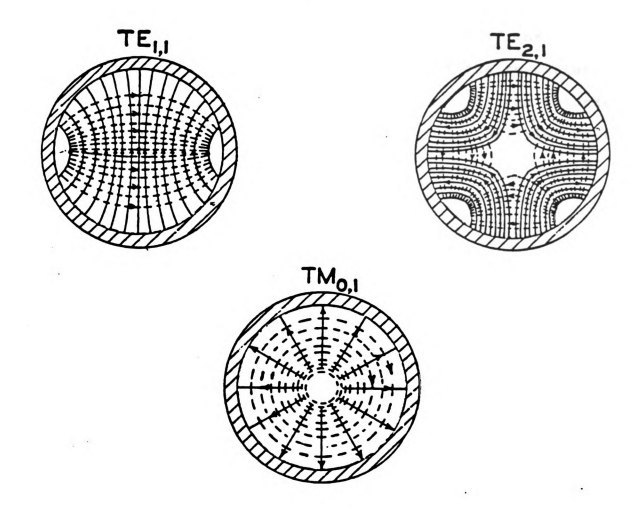


Figure 3.10 Diagrams of field lines for 3 low-order modes in circular waveguide. The solid lines show electric field directions, whereas the dashed lines show magnetic field directions (from Moreno (14)).

In order to determine the distribution of the resonant frequencies for a given length of the resonator cavity, the power reflected back from the cell was recorded as the microwave frequency was swept. A typical plot of the reflected power versus frequency is shown in Figure 3.11. The plot also has the assigned modes for each major resonance seen on the trace. The mode with the most desirable structure is the TEll mode. The reason for this is because it has an electric field maximum in the center of the cell, as shown in Figure 3.10. An important fact to remember however is that the cell is designed to be able to be in resonance at any frequency between 8-18 GHz; however not all the modes, especially at higher frequencies, give good overlap with the infrared radiation.

Another important attribute which was determined for the cell was the "Q" value. The "Q" of the cell is an efficiency term and is expressed as,

$$Q = 2\pi \frac{\text{energy stored}}{\text{energy lost/cycle}}$$
 (3.17)

The quantity Q is used as a figure of efficiency for a resonant circuit. The Q term comes into play for the determination of the electric field inside the cavity as shown in Equation 3.18,

Table 3.1. The first ten roots of $J_{\underline{m}}(x) = 0$.

No.	Value	Mode	
1 .	1.841	TE ₁₁	
2	2.405	TM ₀₁	
3	3.054	TE ₂₁	
4	3.832	TM ₁₁	
5	3.832	TE ₀₁	
6	4.201	TE 31	
7	5.136	TM ₂₁	
8	5.318	TE41	
9	5.332	TE ₁₂	
10	5.520	TM ₀₂	

a Reference (14).

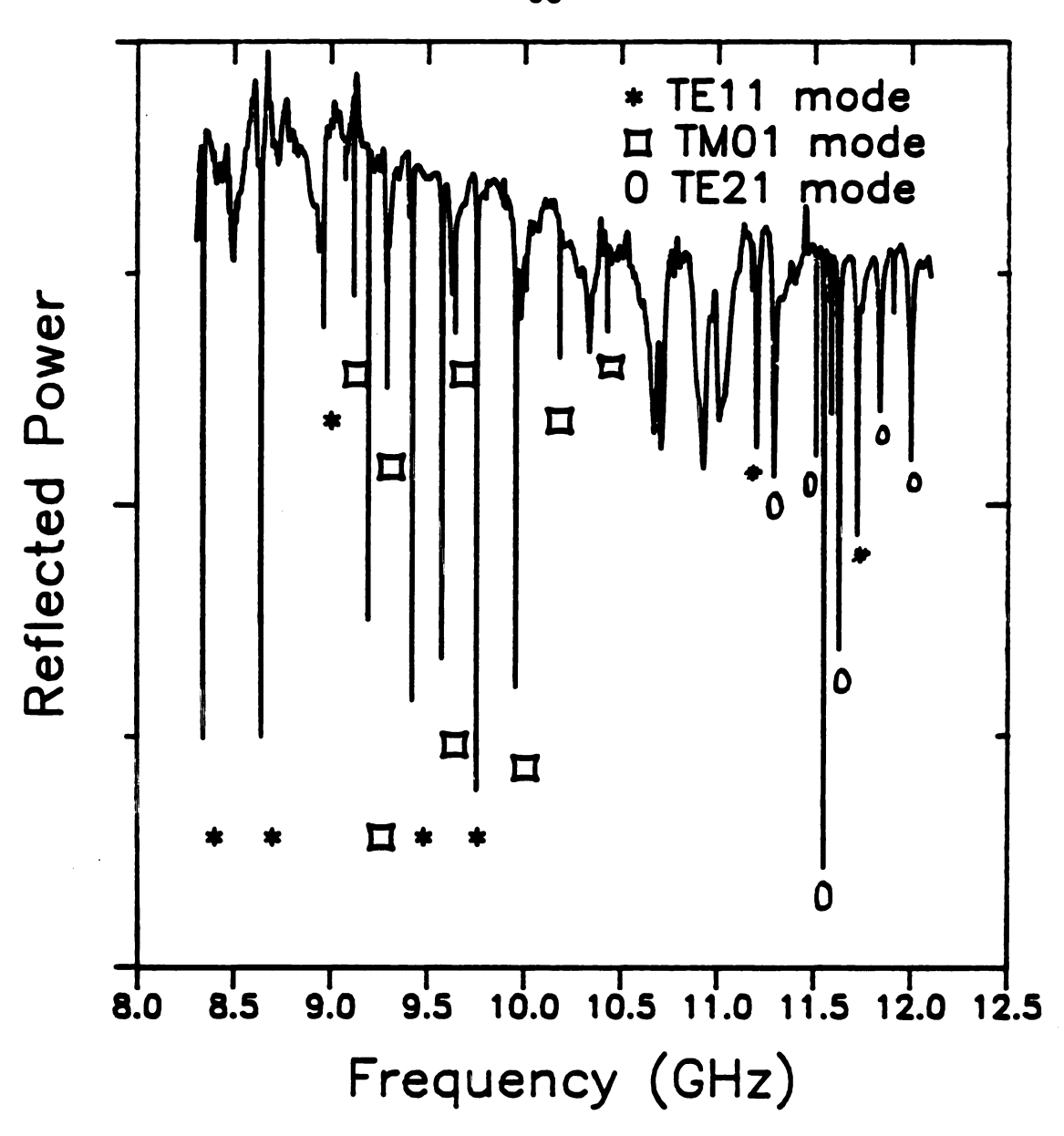


Figure 3.11 Plot of reflected power from microwave cavity cell versus microwave frequency. The sharp dips indicate resonances in the cell.

$$\mathbf{E} = \frac{8.151 \ \mathbf{Q} \ \mathbf{P}}{\omega_0 \ \mathbf{E} \ \mathbf{a}^2 \pi \mathbf{L}} \tag{3.18}$$

In this equation B is the electric field in the center of the cavity, P is the power in watts of the microwave radiation, ω_0 is the angular frequency of the radiation, a is the radius and L is the length of the cell. From the above equation, we can see that the larger the Q value the larger the effective electric field inside the cavity.

The determination of Q for the cell can be done experimentally with the use of the equation,

$$Q = f_0/\Delta f , \qquad (3.19)$$

where f₀ is the resonant frequency and Δf is the full width at half maximum (FWHM). These values can be measured by observing the reflected power from the cell. A plot of reflected power versus frequency is shown in Figure 3.12. From this plot a value for the Q of the cell was determined to be 2,600. Now if we use this value of Q and the dimensions of our cell Equation (3.18), we obtain an electric field E of ~620 V/cm for a microwave power of 20 W. This gives a Rabi frequency of 312 MHz for a transition dipole moment of 1 Debye. In our experiment, it was necessary to use electric fields smaller than this, because

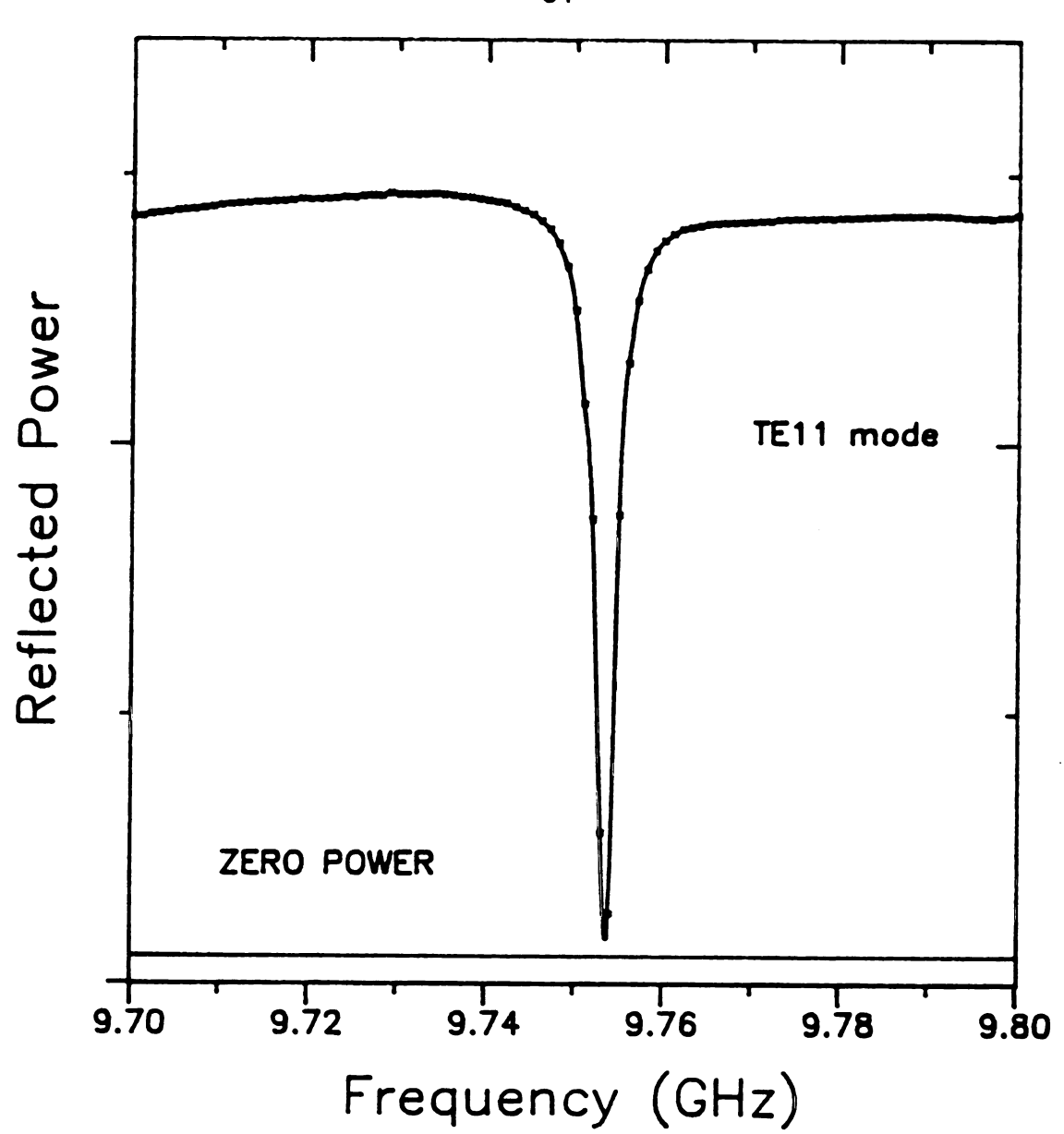


Figure 3.12 Plot of reflected power versus microwave frequency for one resonance of the TEll mode.

at high electric fields the NH_3 sample would break down. Typical Rabi frequencies in our experiments were of the order of 50 to 150 MHz.

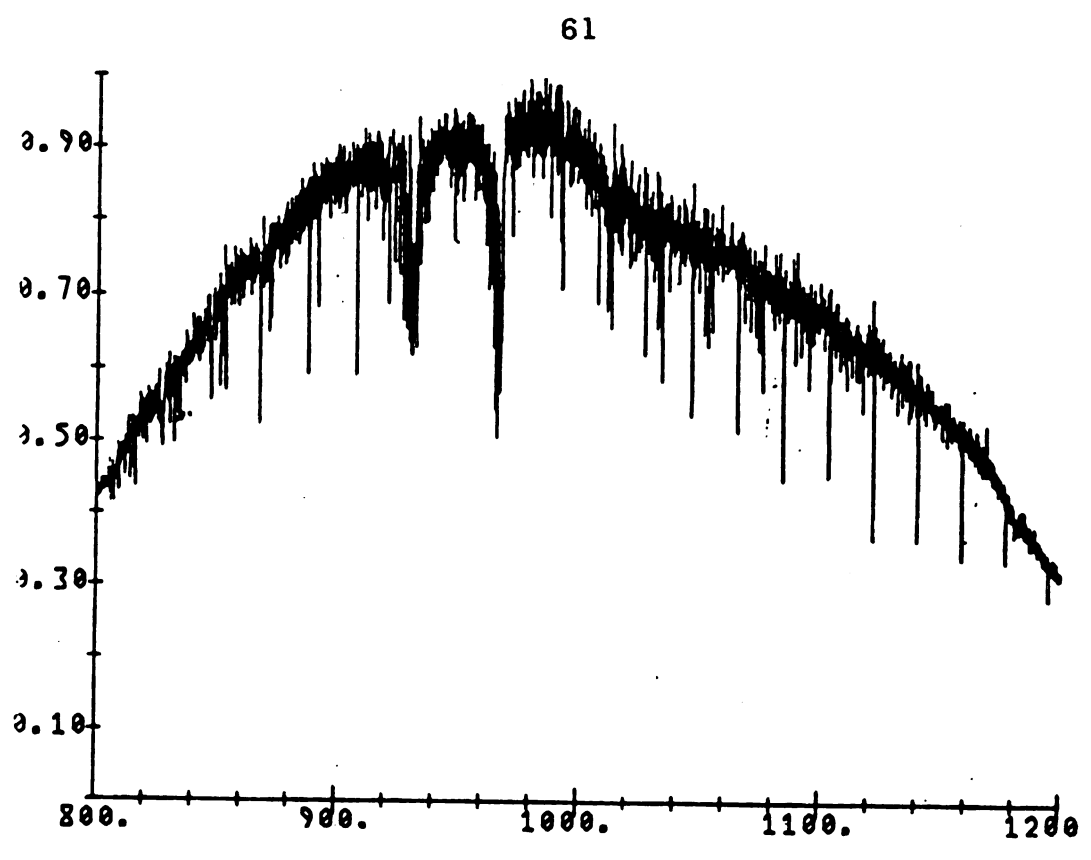
Sample Processing

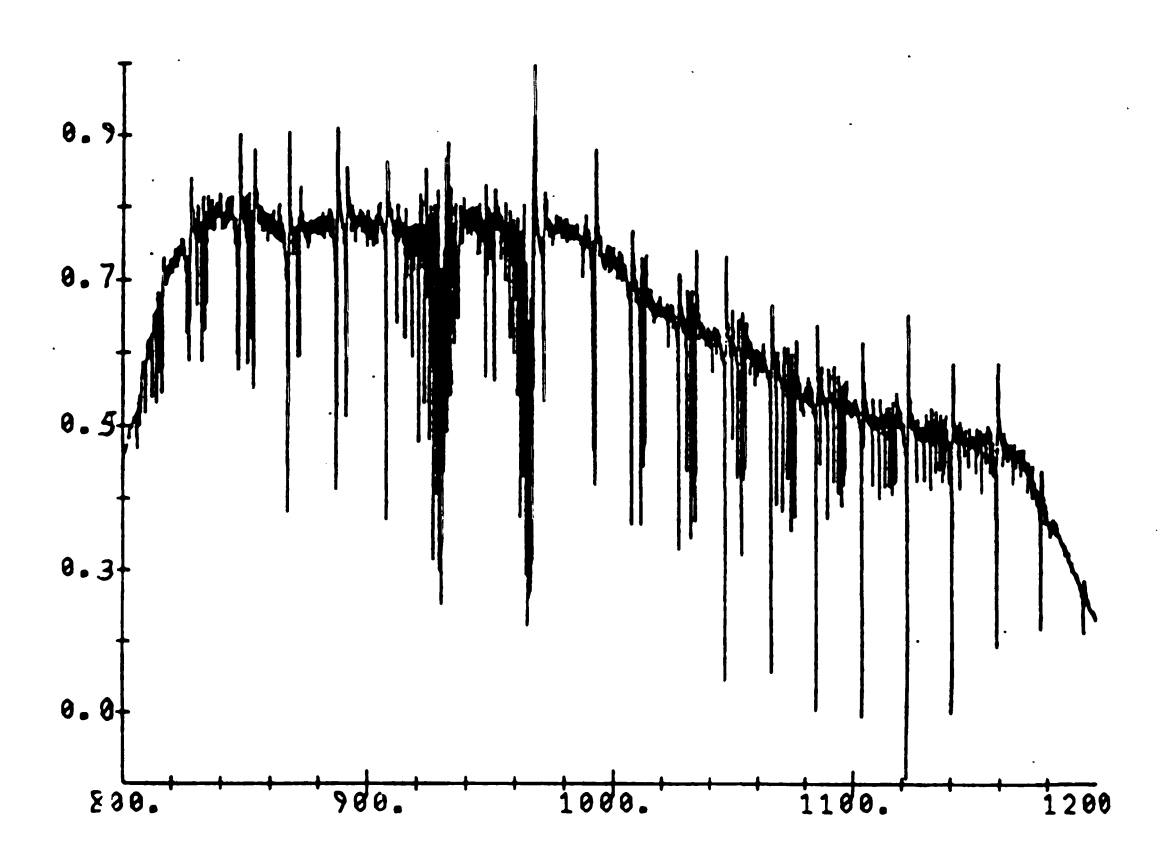
The microwave radiation applied to the coaxial cell was chopped by a PIN diode that was controlled by an applied square wave voltage. The effect of the modulation of the infrared absorption by the pumped microwaves was monitored with a phase-sensitive detector at the output of a preamplifier attached to the infrared detector. The modulation frequency was 100 kHz and the sampling frequency for the interferogram was 3.15 kHz, so that the two frequencies were far enough apart to separate each signal from the other. The reason for modulation of the microwave pump was to improve the signal/noise of the double resonance signal and to suppress the single resonance spectra. We also tried to subtract a spectrum with the microwave pump on from one with the microwave pump off.

An experiment to check the validity of the modulation scheme was carried out by simply modulating the output of the infrared detector and using the phase sensitive detection. The output of the phase sensitive detector was recorded in the usual way and sent to the high speed vector

processor for the Fourier transform calculation. A comparison between a normal spectrum at $0.02~{\rm cm}^{-1}$ resolution of NH $_3$ and the modulated spectrum under the same conditions, as shown in Figures $3.13({\rm A})$ and (B). The two spectra show no significant difference.

Figure 3.13 A comparison of a normal spectrum and a modulated spectrum of NH_3 at 0.02 cm $^{-1}$. The upper trace is the normal calculated spectrum of NH_3 . The lower trace is the calculated spectrum using amplitude modulation and phase sensitive detection on the interferometer signal.





3.4 Results

The results of our attempts to observe infrared-microwave double resonance with a high power microwave source and an FTIR spectrometer were disappointing. There was no detectable effect on the infrared transitions known to be coincident with the pumped inversion energy levels in the ground state of NH₃. Both the modulation experiment and the simple subtraction experiment showed no double resonance effects. Our explanation of this failure and a suggestion for a future experiment will be described in this section.

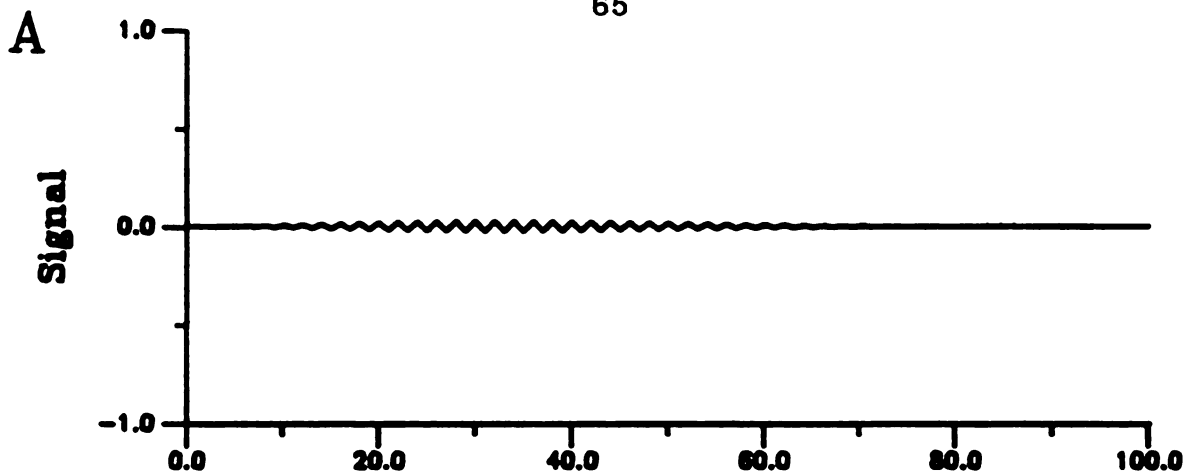
First of all let us go back to the calculation of the Rabi frequency and the coherence splitting effect. If we realize that the entire splitting effect is ~300 MHz and the resolution of our FTIR spectrometer is 600 MHz, the observable splitting will be effectively zero because of the resolution. The splitting signal which should occur has to be averaged over 600 MHz, thus no signal at all will be produced from the coherence splitting unless the Rabi frequency is further increased or the resolution of the infrared spectrometer is raised. The first alternative is impossible because at any higher electric field the sample at 100 mTorr disassociates. The second solution however is possible and has been employed in the following chapter by using the CO₂ sideband system for the infrared source. This

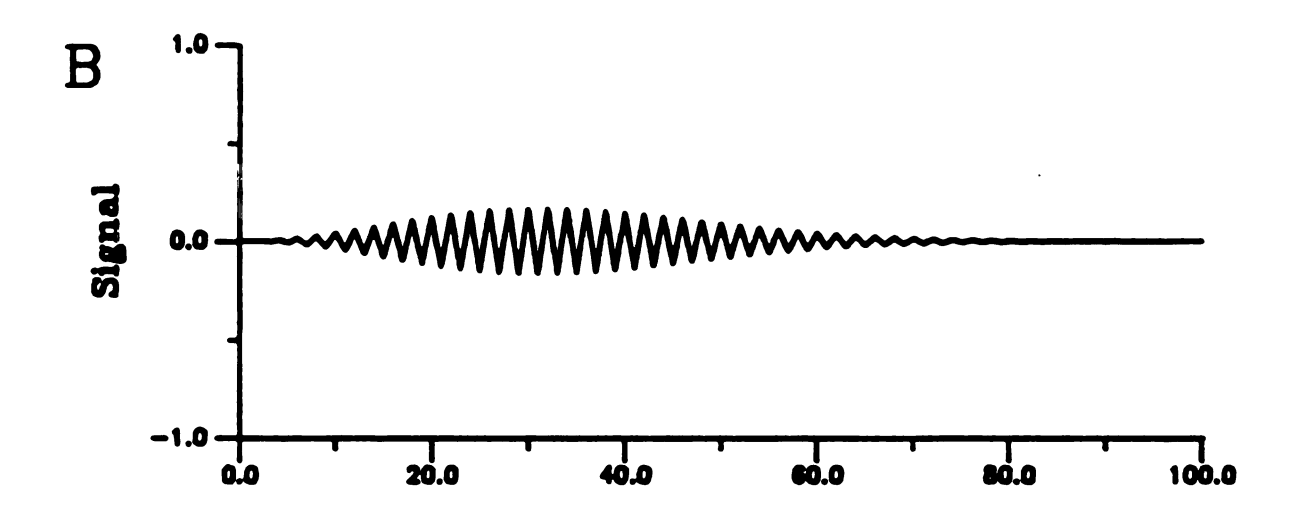
technique of FTIR as the infrared source could still possibly work on higher resolution instruments made by BOMEM or a homemade FTIR such as that at Kitt Peak.

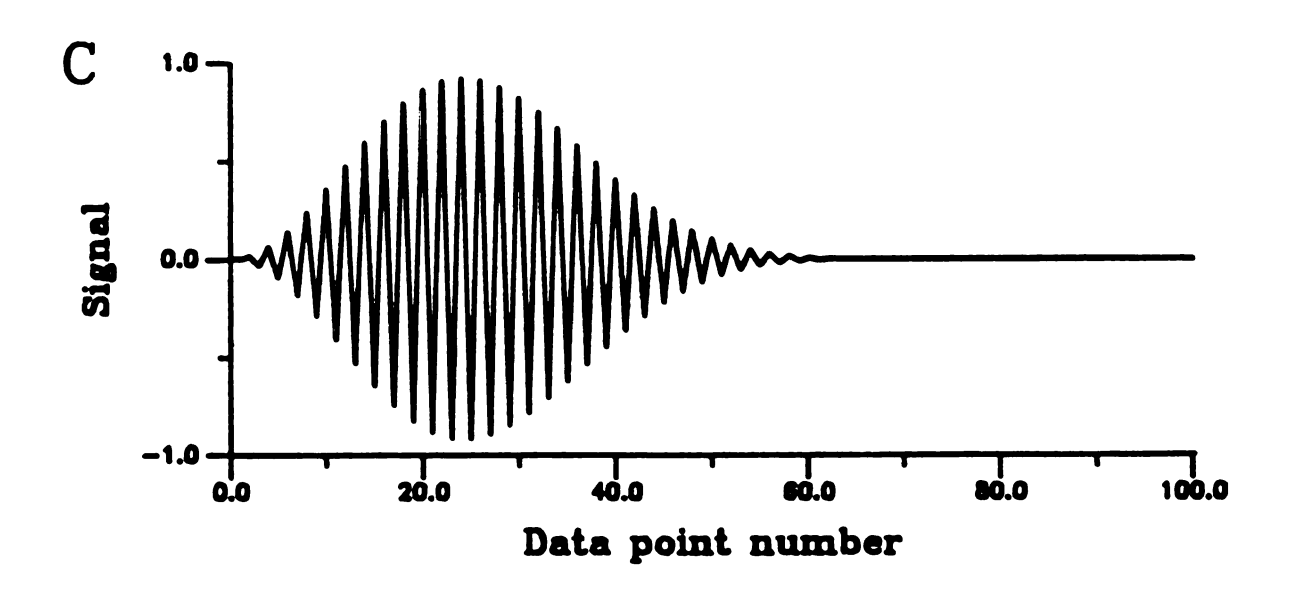
Some calculations on the interferogram signal shape were done using a program written by Peter Wentzell of Michigan State University. The results of some simulations are shown in Figures 3.14 a,b and c. As can be seen the larger the splitting the stronger the interferogram becomes. The splitting here refers to points of the spectrum and the calculation is just an inverse Fourier transformation of the predicted spectrum to obtain the interferogram. One interesting consequence of these simulations is that the signal at zero path difference is zero in the time domain. This is normally the largest signal because under normal conditions the light at zero path difference does not destructively interfere, but when a modulated signal is detected at zero path the signal is zero because the average of all the light on the sample is zero. The fact that there is no zero path burst may cause a strange anomaly to occur when the phase calculation is done on the interferogram.

Another effect that has been mentioned earlier is the population effect. Although this is very small, there have been signal to noise (S/N) ratios reported at 60000:1 (15). Our instrument however only has a S/N ratio of 500:1 and this would not be large enough to see the population change

Figure 3.14 A comparison of calculated interferograms from simulated spectra. Trace (A) was calculated with a splitting of 5 data points. Traces (B) and (C) were calculated with increasing splitting, respectively.







due to the microwave pump. The main reason for this difference in the signal to noise ratio is because of the detector used.

With the FTIR and instrumentation available at
Michigan State University the desired experimental results
for the infrared-microwave double resonance were impossible
to obtain. Therefore after much deliberation this project
using the FTIR spectrometer was abandoned until further
funding for a higher resolution instrument can be found. It
should however be pointed out that the experiment may
succeed if the steps outlined above are taken.

3.5 References

- 1. T. Shimizu, and T. Oka, Phys. Rev. A2, 1177 (1970).
- 2. H. Jones, and F. Kohler, J. Mol. Spec. <u>58</u>, 125 (1975).
- 3. H. Jones, and J. M. Brown, J. Mol. Spec. 90, 222 (1981).
- 4. T. Amano, J. Mol. Spec. 88, 194 (1981).
- 5. S. Yamamoto, K. Kuchitsa, T. Nakanaga, H. Takeo, C. Matsumara, and M. Takami, J. Chem. Phys. 83, 1444 (1985).
- 6. T. Shimizu, and T. Oka, J. Chem. Phys. 53, 2536 (1970).
- 7. M. Takami, J. Chem. Phys. <u>74</u>, 4276 (1981).
- 8. H. Jones, and M. Takami, J. Chem. Phys. 78, 1039 (1983).
- 9. M. Takami, and H. Kuze, J. Chem. Phys. 78, 2204 (1983).
- 10. A. Javan, Phys. Rev. <u>107</u>, 1579 (1957).
- F. J. Wodarczyk, and B. B. Wilson, Jr., J. Mol. Spec.
 37, 445 (1971).
- 12. A. A. Michelson, Amer. J. Sci. 22, 120 (1881).
- 13. J. Asmussen, Michigan State University, E. Lansing, MI., private communication.
- 14. T. Moreno, "Microwave Transmission Design Data", Dover, New York, NY.
- 15. J. W. Brault, Symposium on Molecular Spectroscopy, Ohio State University, June 1985.

CHAPTER IV

Infrared Microwave Sideband Laser Spectroscopy of CH3OH

4.1 Introduction

High resolution infrared spectroscopy gives a wealth of information about molecular structure. Extensive studies of the ν_3 fundamentals as well as the associated hot bands of $^{12}\text{CH}_3\text{F}$ and $^{13}\text{CH}_3\text{F}$ have been carried out by means of an infrared microwave sideband laser in the high resolution infrared spectroscopy laboratory at Michigan State University (1). This chapter describes a preliminary study of the CO stretch vibrational band of CH_3OH . This project had three goals: the first was to familiarize the author with the CO_2 laser and sideband system, the second was to check the results of a diode laser study done on CH_3OH (2,3) and, finally, the third was to separate the Q branch transitions which were unresolved in Fourier transform infrared (4) and diode laser experiments (2,3).

Methanol has previously been studied by diode laser spectroscopy (2,3), by infrared laser Stark spectroscopy (5) and by Fourier transform infrared spectroscopy (4). However, because of internal rotation and overlap of other vibration-rotation bands, the interpretation of the spectra

has been very difficult. For the reasons given above and for a further understanding of the methanol molecule, we decided to obtain spectra of the CO stretch vibrational band.

In addition to a presentation of data for methanol, this chapter includes a discussion of the rotation-vibration theory used for interpretation of the spectra. The discussion emphasizes the asymmetric top case and then explains the methanol molecule in detail. The CO₂ sideband laser is described and the experiment is presented with a discussion of the method of laser stabilization. Finally, the data for methanol are compared to the results of previous studies.

4.2 Theory

General Spectroscopy

Molecules in free space undergo many different types of motion: translation in space, overall rotation, and interatomic vibration. In addition, the electrons are in constant rapid motion. To predict the energies of molecules, their molecular motions must be understood and described.

The Born-Oppenheimer approximation allows the molecular Hamiltonian to be separated into an electronic part and a nuclear part (6). It has been shown that to good approximation the Hamiltonian for nuclear motion is (7)

$$H_{N} = H_{T} + H_{R} + H_{V} , \qquad (4.1)$$

where $\mathbf{H_T}$ is the Hamiltonian for translational motion, $\mathbf{H_R}$ is the rotational Hamiltonian, and $\mathbf{H_V}$ the vibrational Hamiltonian for the nuclear motion. With this convention we can write the energy of the molecule as the sum of these contributions;

$$E = E_{e} + E_{v} + E_{T} + E_{R}$$
 (4.2)

We have, in this case taken into account the electronic energy, vibrational energy, translational energy and the rotational energy.

To calculate the frequencies of vibration-rotation transitions in one electronic state, the electronic and translational energies are not used because they do not change. The vibrational energy change is taken into account by including a difference in the rotationless vibration energies in the fitting of the experimental data. The term $\mathbf{E}_{\text{vib}}^{\ \ \ \ }$ is used here to designate the vibrational energy.

For an introduction to the methanol molecule, the theory will be explained for the asymmetric rotor case; i.e., $I_a = I_b = I_c$ where I_a , I_b , and I_c are principal moments of inertia about three orthogonal axes through the molecular center of mass. A slightly asymmetric top molecule splits the levels labeled by the quantum numbers $\pm K$, which are degenerate in a symmetric top. A common parameter used to indicate the degree of asymmetry is Ray's asymmetry parameter (8),

$$\kappa = \frac{2B - A - C}{A - C} \qquad . \tag{4.3}$$

For a prolate symmetric top (B = C), κ equals -1, whereas for an oblate symmetric top (B = A), κ = +1. The methanol

molecule is a slightly asymmetric prolate top molecule; therefore, it has a κ value near -1. Figure 4.1 shows the rotational energy of a slightly asymmetric top as a function of J.

Since K is no longer a good quantum number for an asymmetric rotor, the energy levels are labeled by the quantum numbers K_{-1} and K_{+1} , which are the values of |K| for the limiting prolate top and oblate top cases, respectively. An asymmetric top molecule can have a dipole moment component in any or all of the three axis directions; thus, there exists three types of spectra: a-type, b-type or c-type. The intensities of rotational transitions of a given type are proportional to the square of the corresponding dipole moment component. The selection rules for the three spectral types can be defined in terms of ΔK_{-1} and ΔK_{+1} , as shown below in Table 4.1 (9).

Table 4.1. Selection rules for asymmetric rotor rotational transitions.

Type	ΔK_{-1}	ΔK_{+1}
8	even	odd
b	odd	odd
c	odd	even

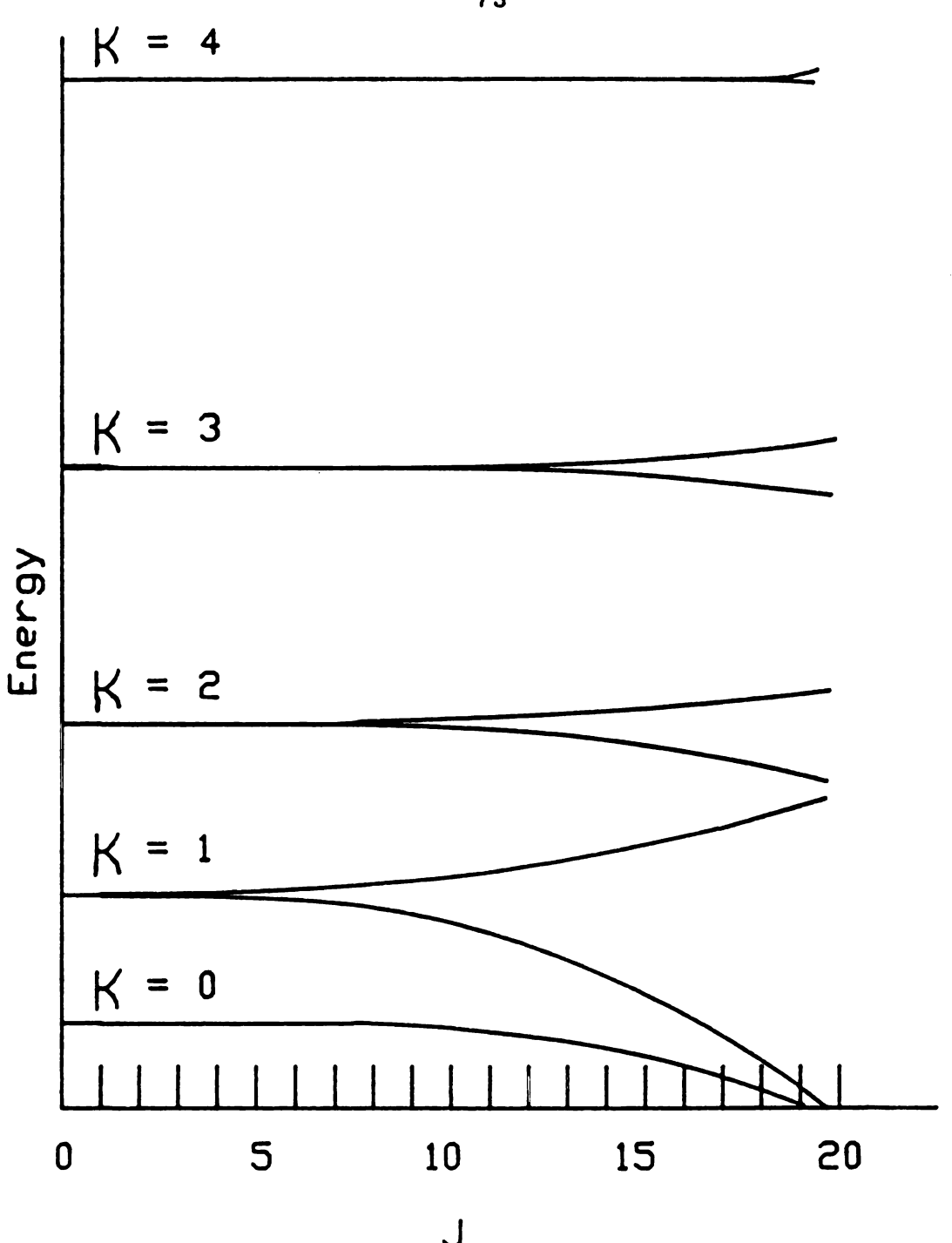


Figure 4.1. The variation of energy levels with J and K for a molecule of slight asymmetry. The deviations of the curves from horizontal lines represent the deviations from the levels of a symmetric top.

The Watson Hamiltonian for an asymmetric rotor (10) is given as:

$$H_{R} = 1/2(B + C)P^{2} + [A - 1/2(B + C)]P_{a}^{2}$$

$$+ 1/2(B - C)(P_{b}^{2} - P_{c}^{2}) - \Delta_{J}P^{4}$$

$$- \Delta_{JK}P^{2}P_{a}^{2} - \Delta_{K}P_{a}^{4} - 2\delta_{J}P^{2}(P_{b}^{2} - P_{c}^{2})$$

$$- \delta_{K}[P_{a}^{2}(P_{b}^{2} - P_{c}^{2}) + (P_{b}^{2} - P_{c}^{2})P_{a}^{2}] .$$
(4.4)

In this equation, A, B, and C are the rotational constants, and Δ_J , Δ_K , Δ_{JK} , δ_J and δ_K are quartic centrifugal distortion constants. The eigenvalues of the Watson Hamiltonian are the rotational energies for an asymmetric top molecule.

Methanol is further complicated by internal rotation of the OH bond with respect to the CH₃ group. Thus the hydrogen attached to the oxygen has three possible positions of equal energy and can tunnel through the potential barrier between them. Hence the internal rotation is hindered by the size of the potential barrier. It has been shown that the three-fold potential barrier splits the torsional energy levels into a nondegenerate (A) level and a doubly degenerate (B) level. The potential barrier height has a direct effect on the size of the splitting. Figure 4.2

shows the behavior of energy levels with various asymmetries and barrier heights. The potential barrier height can be written as a function of the angle of internal rotation γ .

$$V = \frac{V_3}{2} (1 - \cos 3\gamma) + \frac{V_6}{2} (1 - \cos 6\gamma) + \dots$$
 (4.5)

Here $V_3 + V_6 + \dots$ is the maximum potential of the barrier, V_3 is the amplitude of the dominant term, and V_6 is the magnitude of the six-fold term, which measures the deviation of the hindering potential from a simple sinusoid. With the internal rotation energy come two new quantum numbers: n, which labels the torsional levels, and τ , which labels the sublevels for a given n. By using the K quantum number the symmetry species can be related to τ . The convention used is listed below:

$$A + K + \tau = 3N + 1,$$

 $E_1 + K + \tau = 3N,$

 $\mathbb{E}_2 \rightarrow \mathbb{K} + \tau = 3\mathbb{N} + 2$.

Here N is an integer.

To obtain the total rotational Hamiltonian for the calculation of the rotational part of the total energy in Equation (4.2), it is necessary to add to the Watson

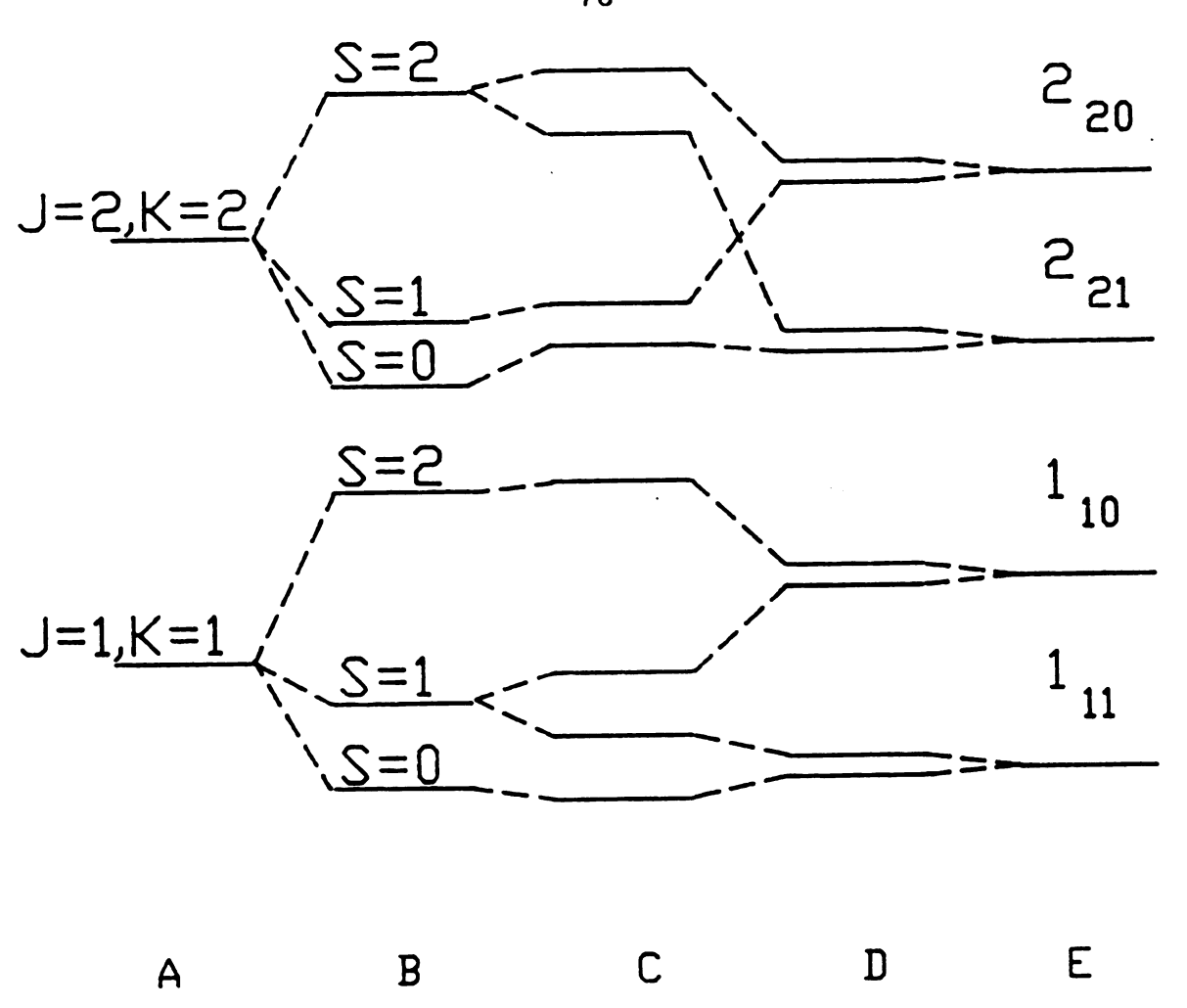


Figure 4.2. Energy levels of a hindered rotor with three potential minima and various asymmetries and barrier heights: (A) symmetric rigid rotor, very high barrier, (B) symmetric rotor, intermediate barrier, (C) asymmetric rotor, intermediate barrier rotor, high barrier, (E) asymmetric rotor, very high barrier (9).

Hamiltonian in Equation (4.4) the torsional potential, Equation (4.5), and the torsional kinetic energy,

$$T = F(P - p)^2 . (4.6)$$

In this equation p is the momentum conjugate to the torsional angle γ and P is a function of the rotational angular momenta. The calculation of the energy levels for an asymmetric rotor with internal rotation has been reviewed (9). However, as will be discussed in the next section, special techniques are necessary for calculation of the levels for methanol.

Methanol

Methanol is an asymmetric top molecule with an internal degree of freedom, referred to as torsion or hindered internal rotation. The $\mathrm{CH_3OH}$ molecule is pictured in Figure 4.3. The theoretical background work done on $\mathrm{CH_3OH}$ and its rotation-internal rotation spectrum has been elegantly presented in a series of papers by Dennison and co-workers (11-16). The three parameters associated with the external rotation are the moments of inertia $\mathrm{I_a}$, $\mathrm{I_b}$ and $\mathrm{I_c}$ about the three orthogonal axes through the center of

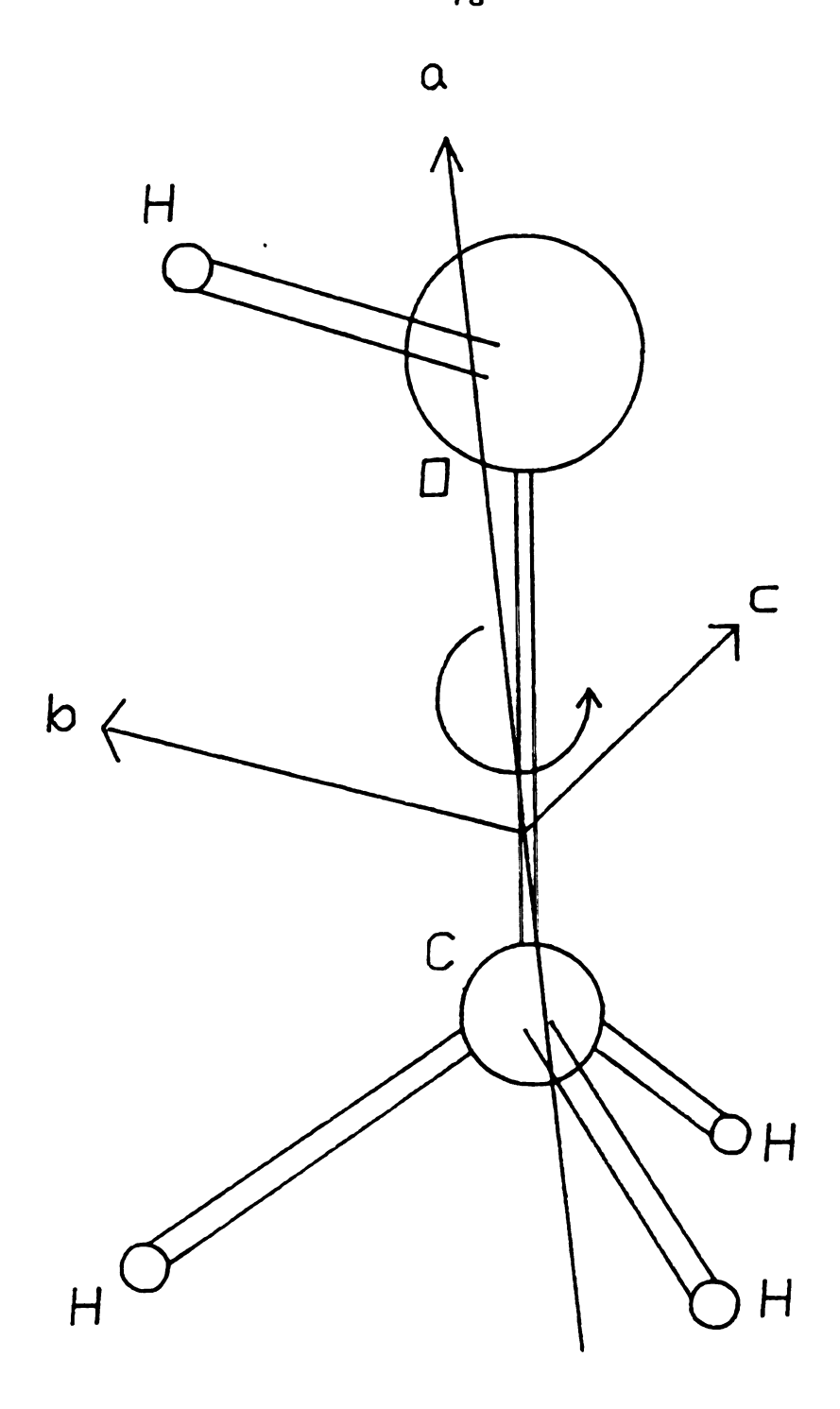


Figure 4.3. A schematic representation of the $\mathrm{CH}_3\mathrm{OH}$ molecule.

gravity of the molecule, as shown in Figure 4.3. The internal rotation is hindered by the potential function in Equation (4.5).

In methanol, the barrier height $V_2 \gg V_6$. The a-axis is usually chosen to be parallel to the symmetry axis of the CH3 group, while the b and c axes are orthogonal to a with b in the COH-plane. These axes are also shown in Figure 4.3. For a proper understanding of the internal rotation we also must know how I is shared between I,, the moment of inertia of the CH_3 group, and $I_{al} = I_{a}-I_{a2}$, which is essentially the moment of inertia of the OH group. In methanol I_{a2} and especially I_{a1} are both small, and this complicates the energy calculation. Along with the parameters already mentioned there is a small product of inertia, I ab, arising from the asymmetry. Additional parameters include centrifugal distortion constants, the parameter V_{κ} , a set of Kirtman constants that account for the effect of centrifugal distortion on the internal rotation, and of course the center frequency of the vibrational band.

The most recent calculation of the energy levels for methanol with the parameters just described has been carried out by Henningsen (17). In his theory, an energy state can be described by the quantum numbers $(n,\tau,K,J)^{V}$, where v indicates the vibrational state, J is the total rotational

angular momentum quantum number, K represents the projection of the rotational angular momentum on the a-axis, n is used to label the torsional level, and τ can be 1, 2 or 3 for the three nearly degenerate torsional states for each level. With this notation the energy levels can be written as (17),

$$E(n_{\tau}K,J)^{v} = E_{vib}^{v} + B^{v}(n_{\tau}K)J(J+1) - D^{v}(n_{\tau}K)J^{2}(J+1)^{2}$$

$$- H^{v}(n_{\tau}K)J^{3}(J+1)^{3} + W^{v}(n_{\tau}K) \qquad (4.7)$$

$$+ (asym. split.)$$

Equation (4.7) looks similar to a symmetric top energy level expansion except for the $W^V(n_{\tau}K)$ and the (asym. split.) terms. The coefficients in Equation (4.7) are as follows,

$$B^{V}(n_{\tau}K) = \frac{1}{2} (B + C) + F_{V}(1 - \cos 3\gamma) + G_{V}(p\gamma^{2}) + L_{V}K(p\gamma) - D_{Jk}K^{2} + b(n_{\tau}K), \qquad (4.8)$$

$$D^{\mathbf{V}}(\mathbf{n}_{\tau}\mathbf{K}) = D_{\mathbf{J}\mathbf{J}} - \mathbf{d}(\mathbf{n}_{\tau}\mathbf{K}), \qquad (4.9)$$

$$W^{V}(n_{\tau}K) = \frac{1}{2} V_{3} \langle 1 - \cos 3\gamma \rangle + F \langle p\gamma^{2} \rangle + [A - \frac{1}{2} (B + C)]K^{2} + \Delta K(n_{\tau}K). \qquad (4.10)$$

The term with $H(n_7K)$ is added to get a better representation

of the energies at high J, p is the momentum conjugate to the angle of internal rotation γ shown in Figure 4.3, and the bracketed quantities are internal rotation expectation values. The constants B, C, F and A are related to the moments of inertia of the molecule according to

$$B = \frac{I_b}{I_b^2 + I_{ab}^2} \frac{h}{4\pi} , \qquad (4.11)$$

$$C = \frac{1}{I_C} \frac{\hbar}{4\pi}, \qquad (4.12)$$

$$F = \left[\frac{I_{a} I_{b} - I_{ab}^{2}}{I_{a1} I_{a2} I_{b} - I_{a2} I_{ab}^{2}} \right] \frac{\hbar}{4\pi} , \qquad (4.13)$$

$$A = \left[\frac{I_a + I_b}{I_a I_b - I_{ab}^2} - \frac{I_b}{I_b^2 + I_{ab}^2} \right] \frac{h}{4\pi}. \quad (4.14)$$

The terms that are multiplied by F_v , G_v and L_v are centrifugal interaction terms that affect the internal rotation. The constants D_{Jk} and D_{JJ} are the normal centrifugal stretching constants, while $b(n_7K)$ and $d(n_7K)$ represent contributions from the asymmetry. The first two terms of $W(n_7K)$ are the expectation values of the potential energy and kinetic energy of the internal rotation, while $\Delta E(n_7K)$ lumps together the rest of the contributions to the

internal rotation. The term AR(n-K) can be expressed as,

$$\Delta E(n_7 K) = 1/2 V_6 < 1 - \cos 6 \gamma > - D_{KK} K^4 + k_1 K^3 < p_{\gamma} > (4.15)$$

$$+ k_2 K^2 < p_{\gamma}^2 > + k_3 K < p_{\gamma}^3 > + k_4 < p_{\gamma}^4 > + k_5 K^2 < 1 - \cos 3 \gamma >$$

$$+ k_6 K < p_{\gamma}(1 - \cos 3 \gamma) > + k_7 < p_{\gamma}^2(1 - \cos 3 \gamma) > + d_0.$$

The expectation values are evaluated for the basic wavefunctions of $H_T^{\ 0}$ for the state $n_T K$. The seven Kirtman constants are also used to calculate the J-independent centrifugal effects. The final term d_0 is from the asymmetry of the molecule. Table 4.2 lists all of the parameters used in the energy level calculation by means of Equation (4.7).

For the vibrational ground state (v = 0), the 20 parameter model described above works well enough to represent the energy levels of the torsional ground state (n = 0) to an accuracy of 0.002 cm⁻¹ in the range of K < 6 and J < 15. However, for the excited torsional states of the CO stretch fundamental, the situation is not as good. To give an idea of the complexity of the spectra, Figure 4.4 is a line spectrum of a region of the CO stretch in methanol compared to that of a normal symmetric top molecule.

Henningsen has done a considerable amount of work on

Table 4.2. Parameters used to calculate the energy levels of the ground and v_5 = 1 states of CH₃OH.

Parameter ^a	сн ₃ он	сн ₃ он
	ground state b	v ₅ =1 ^c
³ vib	0	1030.084 (3)
Ь	34.003856	34.2828 (26)
C C	35.306262	35.6380 (26)
ab	-0.1079	d
al	1.2504	1.2523 (8)
a2	5.3331	5.3334 (8)
73	373.21	392.35 (30)
, 6	-0.52	d
D _{KK}	0.38×10^{-4}	d
κ ₁	-0.48×10^{-4}	d
k ₂	-18.41×10^{-4}	d
k ₃	-53.73×10^{-4}	d
k ₄	-85.50×10^{-4}	d
k ₅	137.07×10^{-4}	d
k 6	67.85×10^{-4}	d
k ₇	0	d
F	-2.389×10^{-3}	-6.546×10^{-3}
G _v	-1.168×10^{-4}	-1.67×10^{-4}
L.	-2.26×10^{-6}	d
D _{JK}	9.54×10^{-6}	d
) JJ	1.6345x10 ⁻⁶	d

The units for the inertial parameters (I's) are kgm^2x10^{47} . The units for all of the remaining parameters are cm^{-1} .

b Reference (16).

c Reference (17).

The ground state parameters were assumed for the excited state.

Asymmetric Molecule with Torsional Barrier

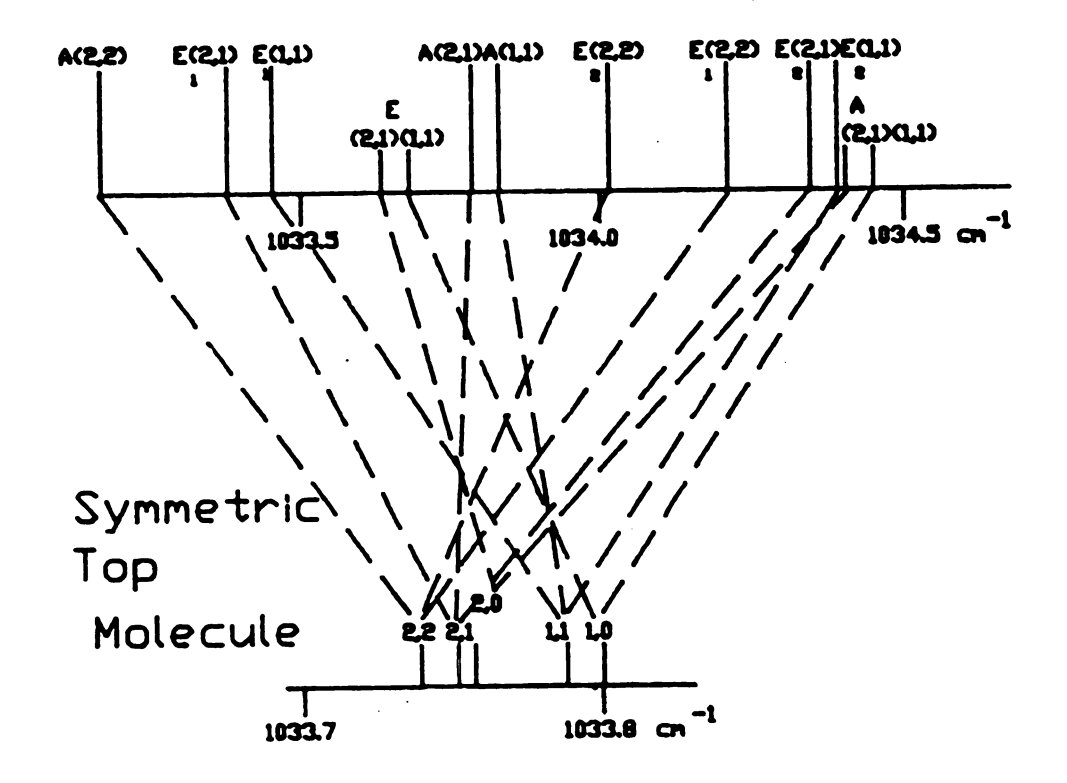


Figure 4.4. Vibration-rotation spectra comparing a symmetric top molecule to an asymmetric molecule with a torsional barrier. It should be noted that the scale of splitting for the symmetric top is five times that for the asymmetric top with internal rotation.

the theory and data analysis of the CH_3OH molecule (4,17,18), and has come up with J independent constants to form an equation for the frequencies of the transitions from v=0 to the v=1 vibrational state. His equation takes the following form for an R branch transition:

$$\nu(J \rightarrow J+1) = \nu_{vib}(n \rightarrow K) + \delta B(J+1)(J+2) + 2B^{0}(J+1)$$

$$- 4D^{0}(J+1)^{3} - \delta D(J+1)^{2}(J+2)^{2} - 6H^{0}(J+1)^{3}$$

$$- \delta H(J+1)^{3}(J+2)^{3} \qquad (4.16)$$

where

$$v_{vib}(n_{\tau}K) = v_{vib} + W^{1}(n_{\tau}K) - W^{0}(n_{\tau}K),$$
 (4.17)

$$\delta B(n\tau K) = B^{1}(n\tau K) - B^{0}(n\tau K),$$
 (4.18)

$$\delta D(n_{\tau}K) = D^{1}(n_{\tau}K) - D^{0}(n_{\tau}K), \qquad (4.19)$$

$$\delta H(n_{\tau}K) = H^{1}(n_{\tau}K) - H^{0}(n_{\tau}K).$$
 (4.20)

The constants in Equation (4.16) were determined by Henningsen (17) and are listed in Tables 4.3 and 4.4.

Table 4.3. Calculated energies and coefficients for the vibrational ground state. a.

n T K	W ⁰ (cm ⁻¹)	$-B^0(cm^{-1})$	$D^{0}(cm^{-1}x10^{-6})$
0 1 0	127.975	0.806772	4.91
0 1 1	131.851	0.806768	6.45
0 1 2	143.435	0.806761	-3.03
0 1 3	162.587	0.806724	1.13
0 1 4	189.072	0.806684	1.66
0 1 5	222.553	0.806628	1.80
0 1 6	262.618	0.806550	1.81
0 1 7	308.841	0.806443	1.78
0 1 8	360.901	0.806302	1.72
0 1 9	418.699	0.806126	1.67
0 1 10	482.396	0.805920	1.64
0 2 0	137.097	0.806865	12.86
0 2 1	142.602	0.806858	0.69
0 2 2	154.183	0.806861	1.67
0 2 3	171.559	0.806815	1.61
0 2 4	194.697	0.806733	1.51
0 2 5	223.820	0.806622	1.45
0 2 6	259.319	0.806489	1.44
0 2 7	301.615	0.806341	1.47
0 2 8	351.077	0.806183	1.53
0 2 9	407.975	0.806020	1.63
0 2 10	472.479	0.805855	1.75
0 3 0	137.097	0.806865	12.86
0 3 1	138.080	0.806831	3.15
0 3 2	145.975	0.806763	-2.83
0 3 3	161.136	0.806696	-0.15
0 3 4	183.818	0.806620	0.77
0 3 5	214.174	0.806536	1.25
0 3 6	252.264	0.806443	1.54
0 3 7	298.057	0.806340	1.72
0 3 8	351.430	0.806224	1.82
0 3 9	412.166	0.806094	1.87
0 3 10	479.949	0.805946	1.88

a Calculated by Henningsen (16).

Table 4.4. Calculated energies and coefficients for the CO stretching state. a.

птК	$W^1(cm^{-1})$	$B^1(cm^{-1})$	$D^{1}(cm^{-1}x10^{-6})$
0 1 0	132.281	0.797808	5.22
0 1 1	136.135	0.797813	7.09
0 1 2	147.651	0.797827	-2.88
0 1 3	166.696	0.797844	1.07
0 1 4	193.043	0.797863	1.62
0 1 5	226.375	0.797873	1.77
0 1 6	266.311	0.797857	1.79
0 1 7	312.467	0.797794	1.76
0 1 8	364.559	0.797666	1.72
0 1 9	422.500	0.797470	1.67
0 1 10	486.436	0.797216	1.64
0 2 0	140.719	0.798126	12.75
0 2 1	146.053	0.798187	0.14
0 2 2	157.536	0.798219	1.54
0 2 3	174.922	0.798177	1.55
0 2 4	198.182	0.798067	1.48
0 2 5	227.513	0.797902	1.44
0 2 6	263.264	0.797703	1.44
0 2 7	305.819	0.797491	1.47
0 2 8	355.521	0.797279	1.53
0 2 9	412.625	0.797078	1.62
0 2 10	477.295	0.796891	1.74
0 3 0	140.719	0.798126	12.75
0 3 1	141.906	0.798029	3.24
0 3 2	150.001	0.797898	-2.75
0 3 3	165.337	0.797781	-0.12
0 3 4	188.156	0.797671	0.78
0 3 5	218.607	0.797572	1.25
0 3 6	256.747	0.797483	1.53
0 3 7	302.544	0.797403	1.70
0 3 8	355.880	0.797329	1.80
0 3 9	416.544	0.797255	1.85
0 3 10	484.237	0.797172	1.87

a Calculated by Henningsen (16).

4.3 Experimental

Introduction

The generation of microwave sidebands on ${\rm CO}_2$ laser emission was first demonstrated in 1979 by Corcoran et al. (19). Since then, there have been many improvements on tunability and power of ${\rm CO}_2$ laser microwave sideband systems (20-23). The most suitable ${\rm CO}_2$ sideband laser for both linear and non-linear spectroscopy is the one developed by Magerl et al. (24).

The first spectroscopic investigation with infrared microwave laser sidebands was performed by Magerl et al. (25) on the SiH₄ molecule. Since this first experiment several others have been carried out (26-28) including a number of studies in our laboratory at Michigan State University (1); both Doppler limited and sub-Doppler spectroscopy have been performed. In this chapter an application of this technique to the CH₃OH molecule is described.

CO₂ Laser

The CO₂ laser used for this experiment includes a 2.0 meter, semi-sealed plasma discharge tube that contains a

mixture of CO₂, N₂, and He at a total pressure of ~10 Torr. The plasma is cooled to 5°C by circulating a refrigerated 50-50 mixture of ethylene glycol in water. The laser tube is a 1.7 meter Pyrex glass tube sealed with ZnSe windows at the Brewster angle. This arrangement of the windows creates laser emission that is polarized parallel to the plane of the optical table. One end of the cavity is a rotatable plane grating ruled with 150 lines/mm mounted on a Lansing Research Corp. rotatable mount. The other end of the cavity is a partially transmitting (90% reflection) spherical concave mirror. The mirror is mounted on a piezoelectric translator (PZT) to control the length of the cavity.

The laser radiation is directed through a cell containing CO_2 at a pressure of 10 - 50 mTorr and then reflected back on itself. The fluorescence from the CO_2 is detected at a right angle to the beam by a liquid N_2 cooled InSb photovoltaic detector (Judson Infrared Inc. J10D). By sinusoidal modulation of the laser's end mirror the laser cavity length is changed and therefore so is the laser frequency. The modulation frequency is 250 Hz. The signal from the fluorescence detector, which is the first derivative of the saturation dip in the fluorescence as a function of frequency, is processed at 250 Hz by a phase sensitive detector (PSD). The output from the PSD is fed back to the operational power supply which controls the

piezoelectric translator (PZT), thus completing the feed-back loop. By using this extra - cavity stabilization process the laser frequency is controlled to ± 150 kHz. Figure 4.5 shows a diagram of the extra-cavity laser stabilization scheme.

A short experiment was done to obtain the laser uncertainty. The experiment consisted of focusing two CO₂ lasers on a liquid nitrogen cooled Honeywell Radiation Center Hg-Cd-Te photovoltaic detector. The output of the detector was then processed by a spectrum analyzer. The stabilization scheme used can control the laser to ± 150 kHz. The conditions for this experiment were that both lasers were locked by the external fluorescence cell method described above. Most of the laser "jitter" is due to the dither voltage applied to the PZT to modulate the fluorescence.

Sideband Generator

The electrooptic crystal used to combine the two radiations is made of CdTe. The structure of the crystal is explained in detail in Dr. Sang Lee's Thesis (1). The dimensions of our crystals are 3x3x25 mm³. The sideband power can be expressed as P_{ab} and is related to the incident

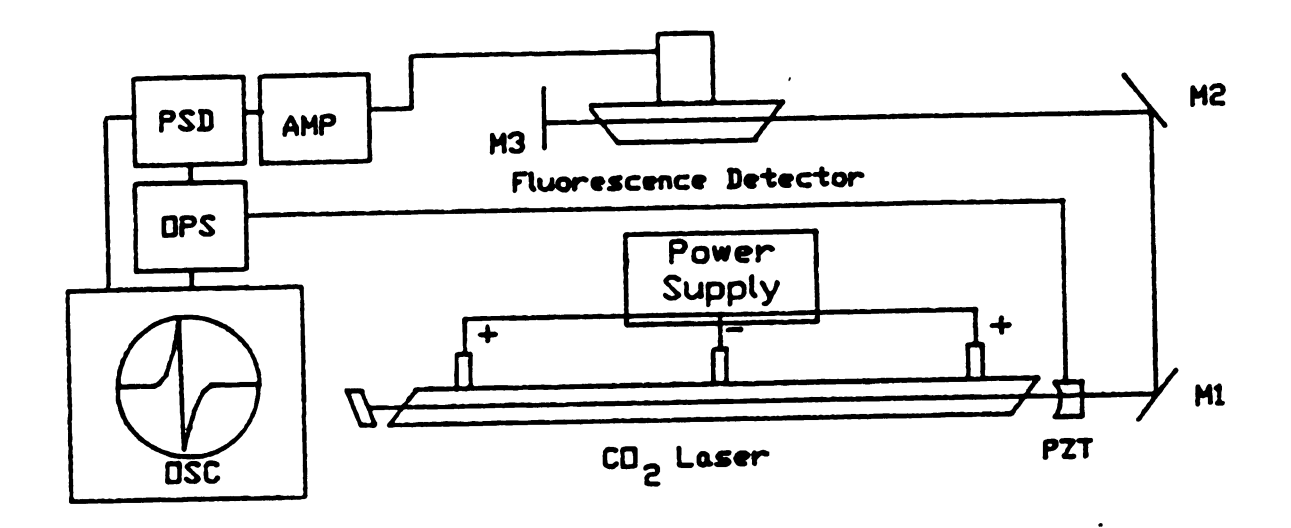


Figure 4.5. A block diagram of an extra-cavity laser stabilization scheme used on the ${\rm CO}_2$ laser.

laser power by the equation (29),

$$P_{\rm sb} = P_{\rm L} \Gamma^2 / 16$$
 . (4.21)

Here, P_L is the incident laser power and Γ is the single - pass phase retardation induced by the transverse electrooptic effect. This second term is linearly dependent on the microwave electric field and the length of the modulator crystal. The Γ term is also inversely proportional to the wavelength of the ${\rm CO}_2$ laser. The sidebands that are generated from the crystal are referred to as plus or minus according to the occurrence of a + or - sign in the equation for the frequency of the sideband,

$$v_{\rm sb} = v_{\rm CO_2} \pm v_{\rm mw} . \qquad (4.22)$$

Here, $\nu_{\rm sb}$, $\nu_{\rm CO_2}$, and $\nu_{\rm mw}$ are the frequencies of the sideband, the laser, and the microwave source, respectively. A diagram of the modulator is shown in Figure 4.6. The specification of the crystal size and the design and adjustment of the housing was done by G. Magerl of the Technical University of Vienna.

The radiation from the CO₂ laser is plane polarized with its electric field parallel to the surface of the optical table. The sideband radiation is generated in the

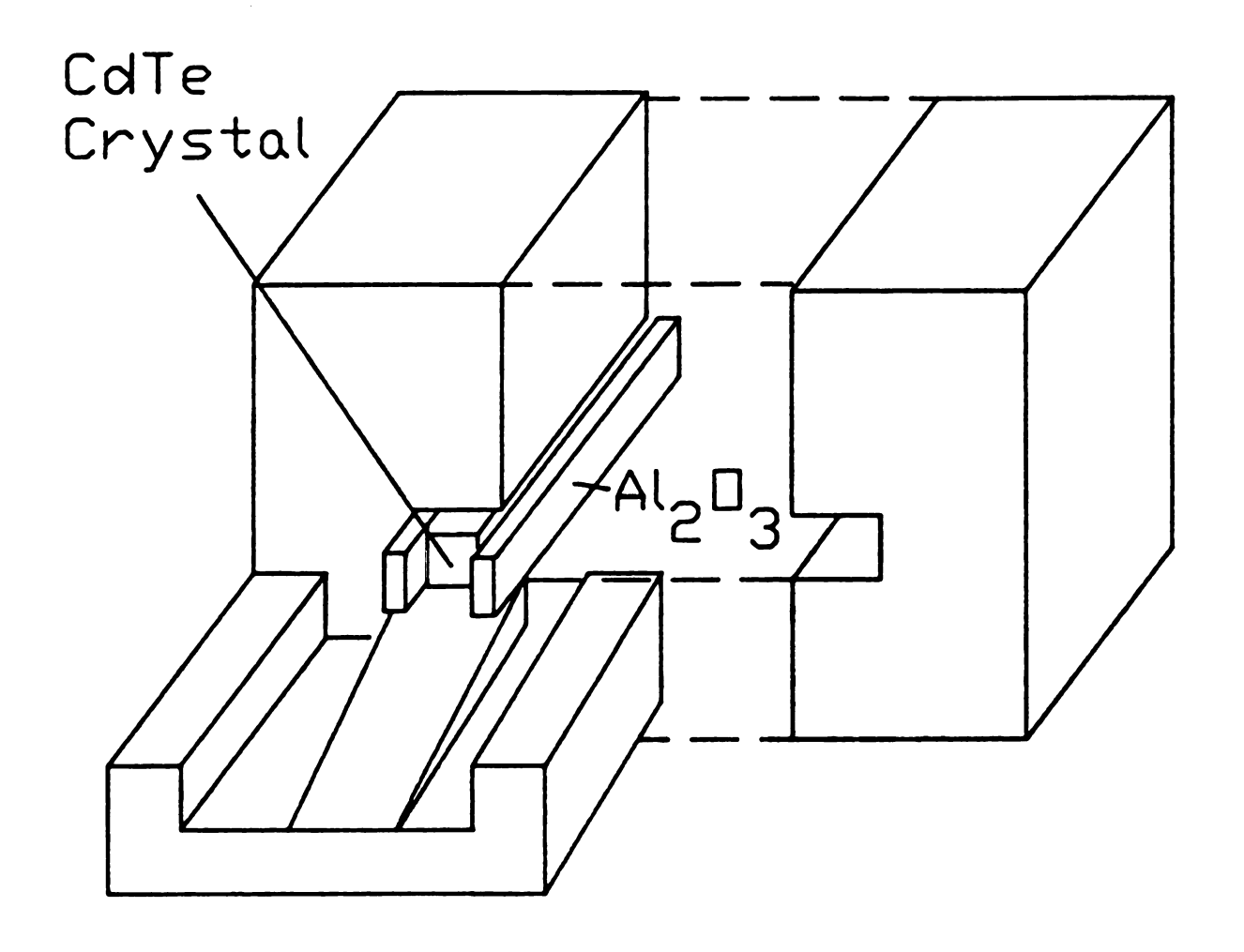


Figure 4.6. A diagram of the sideband modulator. The CdTe crystal is inserted between two ${\rm Al}_2{\rm O}_3$ slabs in a brass housing that is matched to double-ridged waveguide.

crystal and emitted at a polarization that is perpendicular to the polarization of the incident carrier. Therefore, a polarizer can be used to partially separate the carrier (${\rm CO}_2$ laser) from the two sidebands ($\nu_{\rm L} \pm \nu_{\rm mw}$). A sketch of the polarizer and radiation is shown in Figure 4.7. The separation of the radiation into carrier and sidebands by means of a polarizer is not perfect for two reasons. First, the carrier power is typically four orders of magnitude higher than the sideband power, and no polarizer has a discrimination that high. Second, the carrier radiation leaving the modulator is slightly elliptically polarized, so that some carrier ends up having the same polarization as the sidebands.

Figure 4.8 shows the experimental diagram of a CO₂ sideband laser spectrometer in the arrangement for absorption spectroscopy. The microwave radiation was generated by a Varian backward wave oscillator (BWO) operating in the 8.0 - 12.4 GHz or the 12.4 - 18.0 GHz region. The BWO frequency is controlled by an operational power supply (OPS) used to create the helix voltage. The OPS is controlled by the output from a digital to analog converter signal from the minicomputer (Digital PDP8/e). The BWO is stabilized by a phase sensitive synchronizer (Hewlett Packard Model 8709A) which locks the microwave to a harmonic of a synthesized frequency also controlled by the

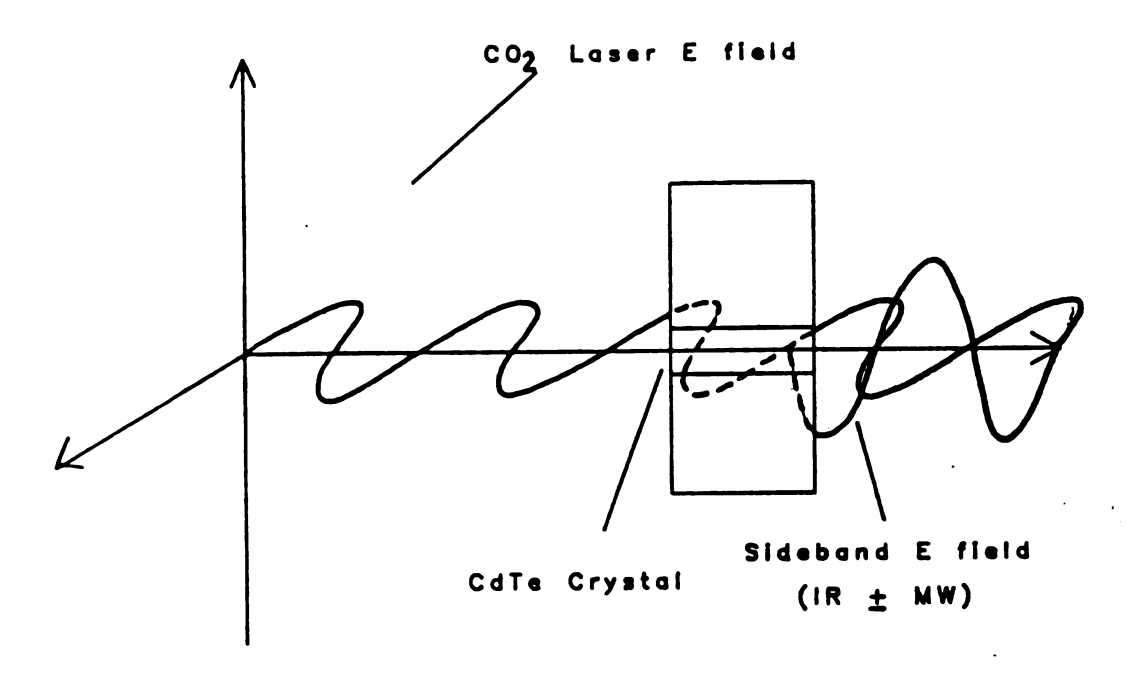


Figure 4.7. A diagram of the electric fields of the ${\rm CO}_2$ laser and sideband laser as created by the sideband modulator crystal.

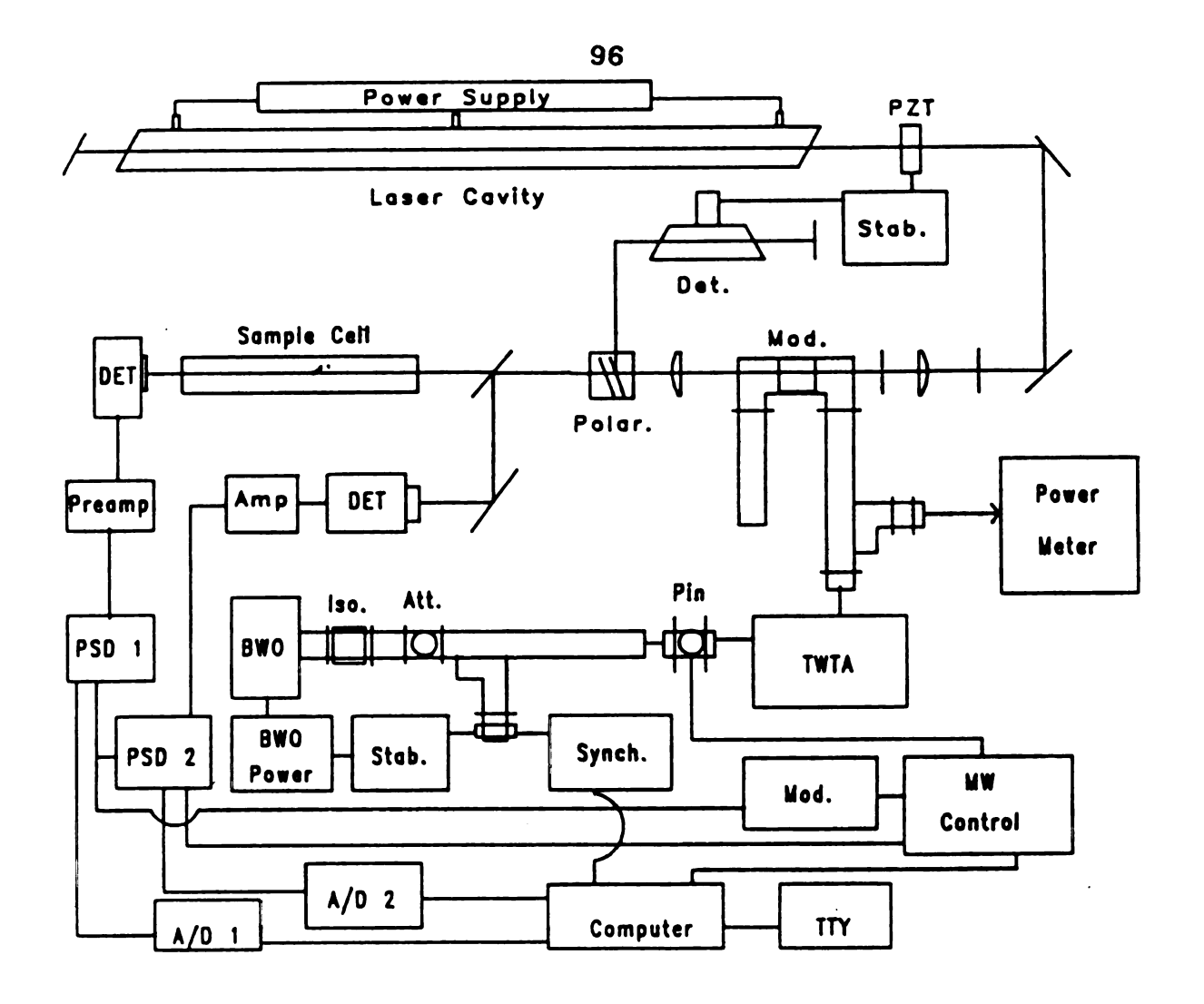


Figure 4.8. A diagram of the sideband laser spectrometer.

computer.

The output radiation from the BWO is divided into two parts by a directional coupler. One part is sent to a diode mixer-multiplier for locking to the precisely known reference frequency. The other part of the power goes to a PIN diode where it is switched on and off at 33.3 kHz. The switched microwave power is amplified by a traveling wave tube amplifier (Varian Model VZM-6991B1 TWTA). The output from the TWTA is sent through a coaxial cable to an adapter to double ridged waveguide and then to the modulator crystal. The microwave radiation leaving the crystal is terminated by an absorbing termination for normal operation or by a tunable short arrangement for operation in the higher power resonant mode.

The laser radiation is focused by a 10 inch focal length ZnSe lens in front of the crystal modulator. After the modulator, the radiation is recollimated by another ZnSe lens with a focal length of 2.5 inches. This combination of lenses condenses the beam by a factor of ~4. The polarizer used includes six ZnSe windows placed at the Brewster angle for the sideband radiation, which then reflects most of the carrier radiation (II VI Inc. polarizer).

A Ge beam splitter divides the sideband radiation into two parts. One beam is used as a reference while the other goes through the sample cell to the sample detector. The

reference beam is monitored by a liquid N₂ cooled Infrared Associates Hg-Cd-Te photoconductive detector. The output from a preamplifier is processed by a phase sensitive lockin amplifier at the reference frequency of 33.3 kHz which is the PIN diode modulation frequency. The signal from the lock-in amplifier is sent into a feedback control circuit designed by Mr. Martin Rabb at Michigan State University. The microwave power is controlled by this circuit through partial attenuation during the "on" period of the PIN diode. The feedback circuit keeps the sideband power at the reference detector at a constant level throughout the microwave sweep.

The sample pressure used for the linear absorption experiments was 0.05 - 1.5 Torr. Most of the experiments were run at 150 mTorr with a cell that has a 50 cm path length. For some of the weaker transitions, a higher pressure was used.

4.4 Results and Discussion

The complexity of the infrared spectrum of the methanol molecule in the CO stretch region (ν_5 band) is evident in both the FTIR spectra and in absorption signals from the sideband experiment. To illustrate the difficulty of assignment, a FTIR absorption spectrum of the CO stretch transitions is displayed in Figure 4.9. The Q branch shown as the center feature is very compact and unresolved. The ${\rm CO}_2$ sideband laser was also unable to resolve the Q branch; however, P and R branch transitions were easily distinguished.

A total of 26 laser lines were used to search through and record the ν_5 band of ${\rm CH_3OH.}$ The number of transitions fit to a Gaussian lineshape to find the center frequencies and relative intensities of the absorption signals was 269. A typical absorption spectrum of methanol taken by the ${\rm CO_2}$ sideband spectrometer is shown in Figure 4.10. The sweep shown here contains both positive and negative sideband absorption signals because we do not employ a monochromator to separate the two sidebands. Even without separating the sidebands, the spectra can be distinguished by recording with the laser frequency intentionally displaced from its center frequency. In this case the frequencies of transitions from the positive and negative sidebands will be

Methanol

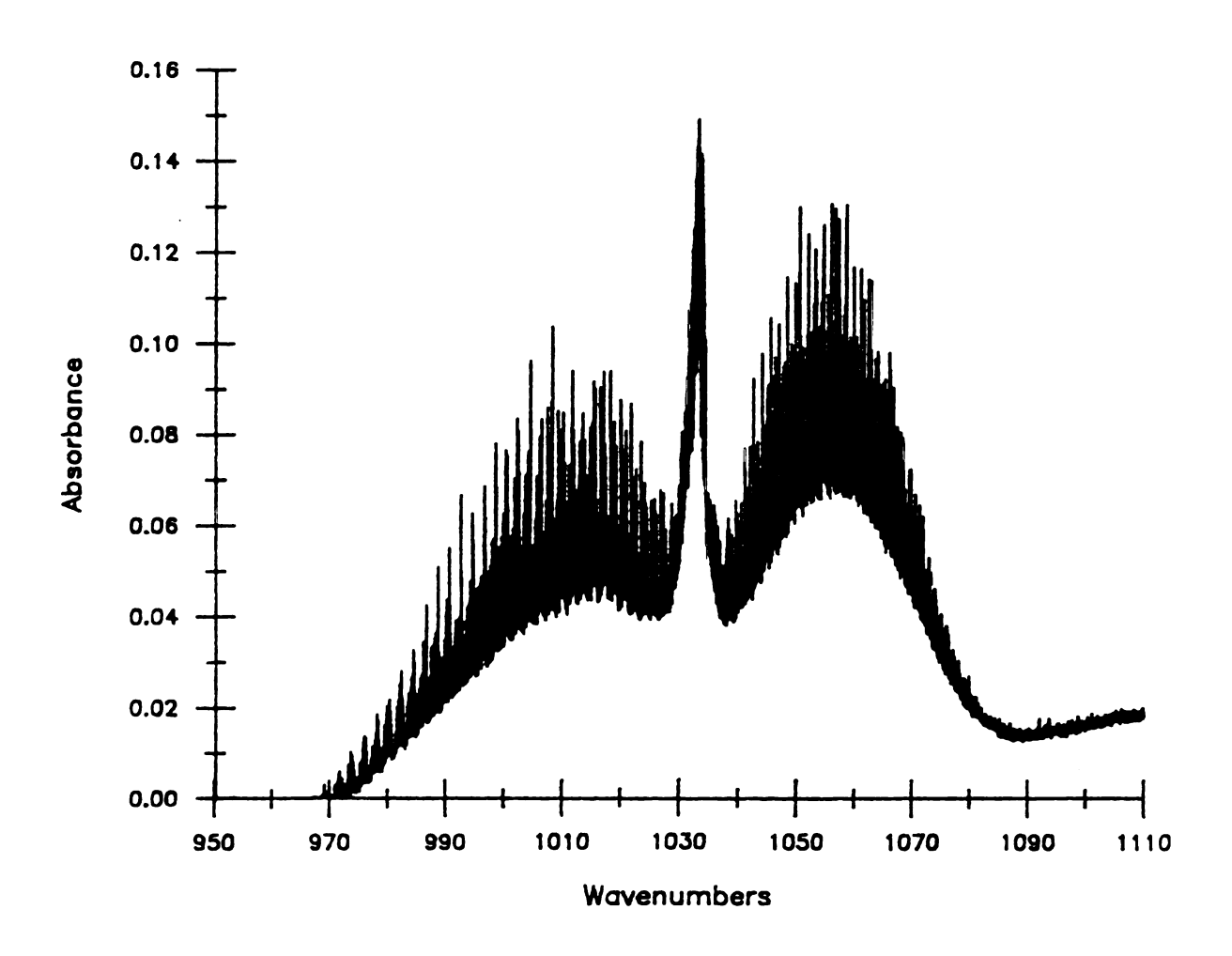


Figure 4.9. FTIR spectrum of the CO stretch band of CH3OH.

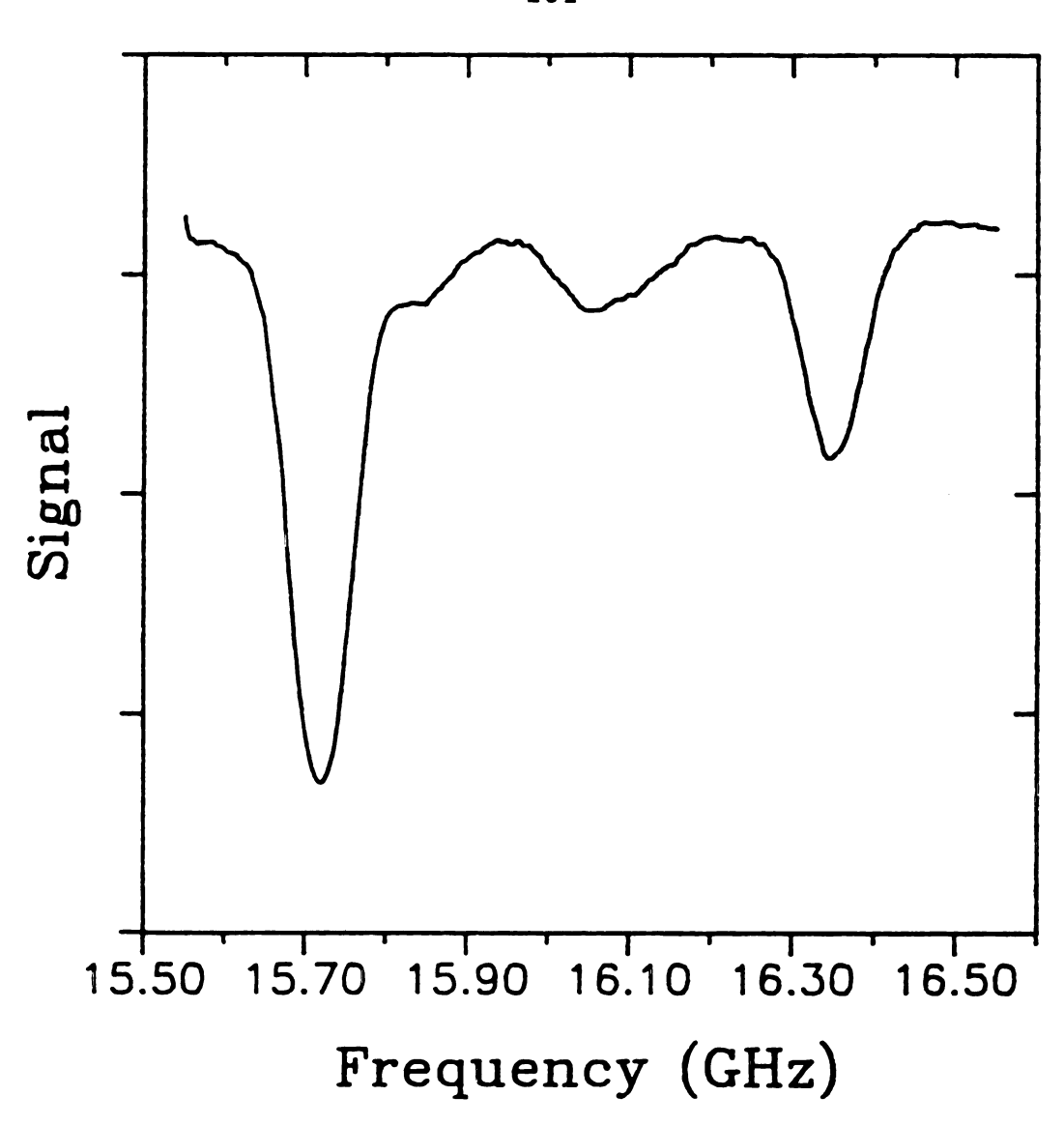


Figure 4.10. A typical scan of the sideband laser showing four transitions of CH_3OH . The CO_2 laser is fixed at the 9P(26) laser line while the microwaves are swept.

shifted in different directions.

An experiment to determine the ratio of (+) sideband radiation to (-) sideband radiation was carried out. The reason for this experiment was to see if both sidebands existed and to record their relative powers. The experiment used a Bausch and Lomb monochromator to separate the two sidebands. After leaving the monochromator the radiation was focused onto a liquid N_2 cooled Infrared Associates Hg-Cd-Te photovoltaic detector. The detector output was processed by a phase sensitive lock-in amplifier (Stanford Research System 510) at the sideband modulation frequency (33.3 kHZ). A plot of the ratios of - to + sideband power vs. frequency for two different laser lines is shown in Figure 4.11. The reason for the change with frequency of the sideband ratio is not understood at this time. However, it should be pointed out that both sidebands exist and are of comparable power.

The measured frequencies of several transitions are compared to the results of diode laser measurements by Sattler et al. (2,3) in Table 4.5. The comparison shows that the frequencies agree within the experimental error of the diode laser work, which is an order of magnitude or more greater than in the present study. Many of the transitions seen in the sideband experiment are very weak and do not appear in the reports of the theoretical calculations

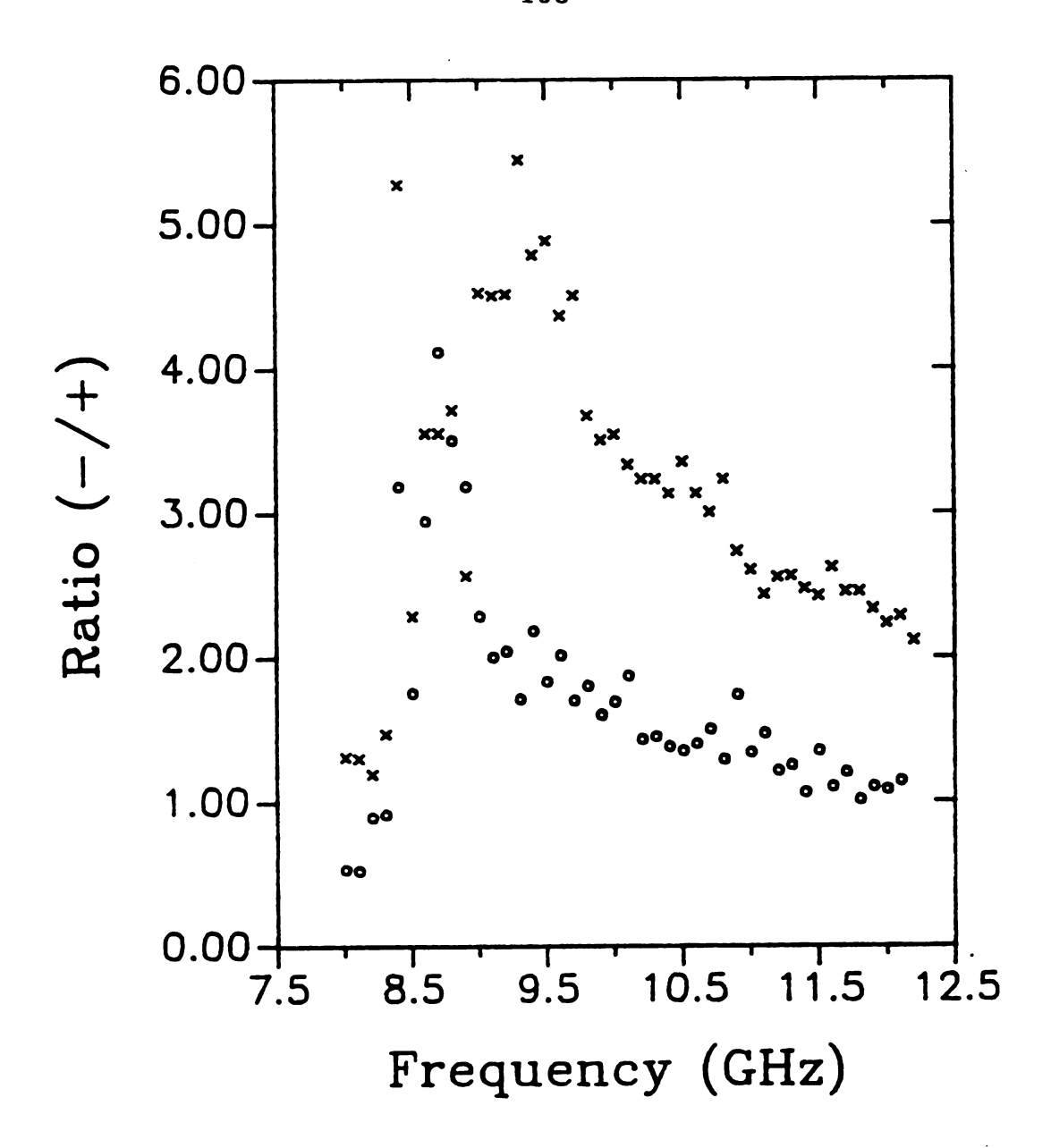


Figure 4.11. A plot of the ratio of (-/+) sidebands versus microwave frequency for two different laser lines (9P(16) (o) and 10R(24) (x)).

\$104\$ Table 4.5. Comparison of $\ensuremath{\text{CH}_3\text{OH}}$ Transitions.

Transition	Sattler ^a	Peterson ^b	
(J, k, n, T)			
R(1,0,0,2)	1036.882	1036.88297	
R(5,2,0,2)	1042.749	1042.74944	
R(5,1,0,2)	1042.850	1042.85117	
R(6,0,0,1)	1044.685	1044.68656	
R(7,2,0,3)	1046.377	1046.37772	
R(7,1,0,3)	1046.300	1046.30095	
R(11,0,0,1)	1051.832	1051.83457	
R(13,1,0,2)	1054.299	1054.29710	

Reference (2,3), an experimental accuracy of ± 0.004 cm⁻¹.

Sideband work done at Michigan State University.

(17,18) or the data from the diode laser work (2,3). These transitions are most likely higher order torsional states (n > 1) or hot band transitions of the CO stretch band. A full list of transitions and intensities is presented in the Appendix.

4.5 References

- S. K. Lee, Ph.D. Thesis, Michigan State University, 1986.
- 2. J. P. Sattler, T. L. Worchesky, and W. A. Riessler, Infrared Phys. 18, 521 (1978).
- 3. J. P. Sattler, T. L. Worchesky, and W. A. Riessler, Infrared Phys. 19, 217 (1979).
- 4. G. Moruzzi, F. Strumia, C. Bonetti, B. Carli, F. Mencarglia, M. Carlotti, G. DiLonarado, and A. Trombetti, J. Mol. Spec. 105, 24 (1984).
- 5. J. O. Henningsen, J. Mol. Spec. <u>83</u>, 70 (1980).
- 6. M. Born and J. R. Oppenheimer, Ann. Physik, <u>84</u>, 457 (1937).
- 7. B. B. Wilson, J. C. Decius, and P. C. Cross, "Molecular Vibrations", McGraw-Hill, New York, 1955.
- 8. B. S. Ray, Z. Physik, 78, 74 (1932).
- 9. C. H. Townes and A. L. Schawlow, "Microwave Spectroscopy", Dover, New York, 1975.
- 10. J. K. G. Watson, J. Chem. Phys., <u>48</u>, 4517 (1968).
- 11. J. S. Koehler and D. M. Dennison, Phys. Rev., <u>57</u>, 1004 (1940).
- 12. D. G. Burkhard and D. M. Dennison, Phys. Rev., <u>84</u>, 408 (1951).
- 13. E. V. Ivash and D. M. Dennison, J. Chem. Phys., <u>21</u>, 1804 (1953).
- 14. K. T. Hecht and D. M. Dennison, J. Chem. Phys., <u>26</u>, 48 (1957).
- 15. D. G. Burkhard and D. M. Dennison, J. Mol. Spec., $\underline{3}$, 299 (1959).
- 16. Y. Y. Kwan and D. M. Dennison, J. Mol. Spec., <u>43</u>, 291 (1972).

- 17. J. O. Henningsen, J. Mol. Spec., <u>85</u>, 282 (1981).
- 18. J. O. Henningsen, J. Mol. Spec., 102, 399 (1983).
- 19. V. L. Corcoran, R. E. Cupp, J. J. Gallagher, and W. T. Smith, Appl. Phys. Lett. 16, 316 (1970).
- 20. P. K. Cheo and M. G. Gilden, Appl. Phys. Lett., <u>28</u>, 626 (1976).
- 21. E. Bonek and H. Korechy, Appl. Phys. Lett., 25, 750 (1974).
- 22. G. Magerl and R. Bonek, J. Appl. Phys., 47, 4901 (1976)
- 23. G. Magerl and E. Bonek, Appl. Phys. Lett., 34, 452 (1979).
- 24. G. Magerl, W. Schupita, and E. Bonek, IEEE J. Quantum Electron. QE-18, 1214 (1982).
- 25. G. Magerl, E. Bonek, and W. A. Kreiner, Chem. Phys. Lett. <u>52</u>, 473 (1977).
- 26. G. Magerl, W. A. Kreiner, B. Furch, and B. Bonek, Acta Phys. Austriaca Suppl. 20, 167 (1979).
- 27. G. Magerl, W. Schupita, E. Bonek, and W. A. Kreiner, J. Mol. Spec. 83, 431 (1980).
- 28. G. Magerl, J. M. Frye, W. A. Kreiner, and T. Oka, Appl. Phys. Lett. <u>42</u>, 656 (1983).
- 29. N. McAvoy, J. Osmundson, and G. Schiffner, Appl. Opt. 11, 473 (1972).

CHAPTER V

Infrared-Microwave Double Resonance with a Sideband Laser

5.1 Introduction

Infrared-microwave double resonance has been an important investigative tool used for studies of both weak transitions and very densely packed vibrational bands. The normal scheme of the infrared microwave double resonance experiment is to pump a vibration rotation transition with strong infrared radiation and observe the rotational transitions in the excited vibrational state with a weak microwave source. However, this type of experiment is limited to vibrational transitions coincident with the pumping infrared radiation source, usually a continuous wave laser with widely-spaced lasing frequencies. experiments done in the high resolution infrared spectroscopy laboratory at Michigan State University utilized a high power microwave source to pump ground state rotational transitions and a low power infrared ${\tt CO}_2$ sideband laser to observe vibration rotation transitions. arrangement of continuously-tunable pump and signal sources enables the use of the extensive information available about ground state rotational transitions, so that observation of

a double resonance effect usually leads to straightforward assignment of the excited vibrational band. This technique is identical to the FTIR - microwave double resonance experiment explained in Chapter 3, except that we now have replaced the FTIR with a tunable infrared microwave sideband laser (IMSL).

With the advent of the sideband laser new experiments in high resolution laser spectroscopy became possible. The use of an electrooptic modulator to generate microwave sidebands on CO₂ infrared laser radiation was first carried out for spectroscopic investigations by Corcoran et al. (1) and later developed into a practical procedure by Magerl et al. (2). The sideband laser employs a CdTe electrooptic crystal which mixes microwave and infrared radiation and generates frequency tunable coherent infrared sidebands of high spectral purity. The sidebands are the infrared frequency plus the microwave frequency and the infrared frequency minus the microwave frequency. Thus by changing the microwave frequency the frequencies of the sideband laser can be changed.

The first applications of an IMSL system in the ${\rm CO}_2$ laser region at Michigan State University made use of a modulator designed and adjusted by G. Magerl and were carried out by S. Lee (3,4). In this work a large number of transitions in the ν_3 fundamental bands and in the $2\nu_3 + \nu_3$

bands of $^{12}\text{CH}_2\text{F}$ and $^{13}\text{CH}_2\text{F}$ were assigned. The molecular parameters including quartic, sextic, and octic centrifugal distortion constants were determined. Lee also used the CO, sideband laser and a waveguide laser for infrared-infrared double resonance (5). Almost simultaneously, H. Sasada used the IMSL system to measure the frequencies of a number of transitions in vibrational hot bands of $^{14}\mathrm{NH_3}$ and $^{15}\mathrm{NH_3}$ (6). In addition to the work at MSU, IMSL systems in the ${\tt CO}_2$ laser region have been used in the laboratories of Magerl and Oka. Oka and Magerl have also collaborated on many projects and were the first to obtain sub-Doppler spectra (so-called "saturation dips" or "Lamb dips") with a sideband laser system (7). The Lamb-dip results demonstrate that the radiation is sufficiently powerful to saturate vibration-rotation transitions. The CO, sideband laser has also been used for ion spectroscopy and infraredradiofrequency double resonance spectroscopy (8,9). obvious from this short historical overview of the sideband laser that the IMSL system is an important tool in the field of laser spectroscopy.

The topic of infrared-microwave double resonance was discussed in Chapter 3; therefore, the present chapter will only discuss the molecules involved in these studies and the results obtained from the double resonance experiments. The next section will describe the calculations carried out for

 ${
m CH_3OH}$ and ${
m CF_3I}$. After that, the three-level calculations and the lineshape analysis will be presented. Finally, the experiments performed on ${
m CH_3OH}$ and ${
m CF_3I}$ along with an explanation of the results from the lineshape calculation will be covered.

5.2 Theory

${\tt Methanol~(CH_3OH)}$

The vibration rotation energies of methanol have been described in detail in Chapter 4. Therefore, in this section the theoretical considerations and the parameters used for calculation of energy levels in the CO stretching vibrational state will be discussed only briefly. Methanol is a slightly asymmetric top with internal rotation. The internal rotation of the OH group can be described by using two quantum numbers n and τ . Henningsen (10) has developed an equation for the energy levels in methanol which has parameters independent of J. The equation is given below.

$$E(n,T,K,J)^{v} = E_{vib}^{v} + B^{v}(n,\tau,K)J(J+1)$$

$$- D^{v}(n,\tau,K)J^{2}(J+1)^{2} - H^{v}(n,\tau,K)J^{3}(J+1)^{3}$$

$$+ W^{v}(n,\tau,K) + (asym. splitting)$$
(5.1)

Here, n labels the torsional level and τ designates the three nearly degenerate states (1,2, or 3) for each torsional level, K is the projection of the rotational angular momentum on the a-axis, v denotes the vibrational state, and J is the angular momentum quantum number. The quantity $R_{vib}^{\ \ v}$ is the center frequency for the v^{th}

vibrational band and B^V , D^V , H^V and W^V are all constants, as listed by Henningsen (10,11). The asymmetry is treated as a perturbation because of its small effect on the energy levels. The equation used to calculate the asymmetric splitting is

asym. splitting =
$$S^{CO}(K,n) = \frac{(J+K)!}{(J-K)!}$$
 (5.2)

where $S^{CO}(K,n)$ is a rapidly decreasing function of K,

$$S^{co}(1,1) = \frac{1}{2}(B - C)^{co} \cdot I_{1,-1}^{co}$$

$$S^{co}(1,1) = 41.9 \text{ MHz}$$

$$S^{0}(1,1) = 48.6 \text{ MHz}$$

$$S^{0}(2,1) = 0.0097 \text{ MHz}$$

$$S^{co}(2,1) = 0.0065 \text{ MHz}$$

Where $I_{1,-1}$ is the overlap integral of the A-state internal rotation wavefunctions with $K=\pm 1$. The terms, S^{co} and S^{0} are splitting constants for the CO stretch and ground states, respectively.

By using equation (5.1) for the energy levels the frequencies of the P,Q and R branch transitions can be calculated by the following three equations, respectively:

$$\nu(J + J - 1) = \nu_{vib}(n_{\tau}K) + \delta B(n_{\tau}K)J(J + 1) - 2B^{co}(n_{\tau}K)J$$
$$- \delta D(n_{\tau}K)J^{2}(J + 1)^{2} + 4D^{co}J^{3} - \delta H(n_{\tau}K)J^{3}(J + 1)^{3}$$
$$+ H^{co}(n_{\tau}K)J^{3}(6J^{2} + 2)$$

$$\nu(J \to J) = \nu_{vib}(n_{\tau}K) + \delta B(n_{\tau}K)J(J+1) - \delta D(n_{\tau}K)J^{2}(J+1)^{2} - \delta H(n_{\tau}K)J^{3}(J+1)^{3}.$$

$$\nu(J \rightarrow J + 1) = \nu_{vib}(n\tau K) + \delta B(n\tau K)(J + 1)(J + 2)$$

$$+ 2B^{0}(n\tau K)(J + 1) + 4D^{0}(n\tau K)(J + 1)^{3} - \delta D(n\tau K)(J + 1)^{2}(J + 2)^{2}$$

$$- H^{0}(n\tau K)(J + 1)^{3}(6(J + 1)^{2} + 2) - \delta H(n\tau K)(J + 1)^{3}(J + 2)^{3},$$

Here,
$$v_{vib}(n_{\tau}K) = v_{vib} + W^{co}(n_{\tau}K) - W^{0}(n_{\tau}K)$$
,

$$\delta B(n\tau K) = B^{CO}(n\tau K) - B^{O}(n\tau K),$$

$$\delta D(n_{\tau}K) = D^{CO}(n_{\tau}K) - D^{O}(n_{\tau}K),$$

$$\delta H(n\tau K) = H^{CO}(n\tau K) - H^{O}(n\tau K).$$

Equations (5.4), (5.5) and (5.6) were used by Henningsen to calculate the frequencies of the rotation-vibration

transitions of the CO stretching band of $\mathrm{CH_3OH}$. This calculation was also done in our laboratory and used for comparison with the experimental results.

CF₃I

 ${
m CF}_3{
m I}$ is a symmetric top molecule with a nuclear electric quadrupole moment from the 5/2 spin of the iodine nucleus. The quadrupole coupling constant in ${
m CF}_3{
m I}$ is very large (~2100 MHz). Use of a rigid rotor approximation for ${
m CF}_3{
m I}$ with addition of centrifugal distortion effects associated with the rotation gives

$$E(J,K) = BJ(J+1) + (A-B)K^{2} - D_{J}J^{2}(J+1)^{2}$$

$$- D_{K}K^{4} - D_{JK}J(J+1)K^{2} + H_{JJ}J^{3}(J+1)^{3}$$

$$+ H_{JJK}J^{2}(J+1)^{2}K^{2} + H_{JKK}J(J+1)K^{4} + H_{KKK}K^{6} + \dots$$
(5.7)

This equation is a power series in J(J+1) and K^2 . For low J and K values the quartic centrifugal distortion terms are adequate. However, for energy calculations of high J and K, as with any expansion series, the higher order terms should be included. Equation (5.7) does not include any effects of the quadrupole splitting caused by the iodine atom.

The size of the quadrupole coupling constant makes perturbation theory inadequate for energy level calculations. Therefore a method developed by Benz et al. (12) was used. By setting up an energy matrix and diagonalizing it directly, the energy levels can be calculated to high accuracy. The non-zero elements of the energy matrices used for the calculation are as follows:

$$\langle J, K, F | H | J, K, F \rangle = \langle J, K, F | H_R | J, K, F \rangle \delta_{J, J}$$
 (5.8)
 $+ \langle J, K, F | H_O | J, K, F \rangle$

$$\langle J, K, F | H_R | J, K, F \rangle = BJ(J+1) + (A-B)K^2 - D_J J^2(J+1)^2$$
 (5.9)
- $D_{JK} J(J+1)K^2 - D_K K^4$

$$\langle J, K, F | H_Q | J, K, F \rangle = e_1 [3K^2 - J(J+1)] x_{zz}$$
 (5.10)

$$\langle J, K, F | H_Q | J+1, K, F \rangle = -3e_2 K [(J+1)^2 - K^2]^{1/2} x_{zz}$$
 (5.11)

=
$$\langle J+1, K, F | H_{O} | J, K, F \rangle$$
 (5.12)

$$\langle J, K, F | H_Q | J+2, K, F \rangle = 3e_3 \{ [(J+1)^2 - K^2] [(J+2)^2 - K^2] \}^{1/2} x_{zz}$$

$$= \langle J+2, K, F | H | J, K, F \rangle \qquad (5.13)$$

In these equations, F is the quantum number for the square of the total angular momentum (vector sum of rotational and nuclear spin angular momentum) and $x_{zz} = eQq$

is the quadrupole coupling constant. All other matrix elements of H_R + H_Q are assumed to be zero. Also,

$$e_1 = \frac{3G(G+1)/4 - I(I+1)J(J+1)}{2I(2I-1)J(J+1)(2J-1)(2J+3)}, \qquad (5.14)$$

$$G = F(F+1) - I(I+1) - J(J+1),$$
 (5.15)

$$e_2 = G_1G_2 /[8I(2I-1)J(J+1)(J+2)],$$
 (5.16)

$$G_1 = F(F+1) - I(I+1) - J(J+2),$$
 (5.17)

$$G_{2} = \frac{[(F+I+J+2)(J+I-F+1)(F+J-I+1)(F+I-J)]}{[(2J+1)(2J+3)]^{1/2}}, \qquad (5.18)$$

$$e_3 = \frac{G_3 G_4}{16I(2I-1)(J+1)(J+2)(2J+3)[(2J+1)(2J+5)]^{1/2}}, (5.19)$$

$$G_3 = [(F+I+J+2)(F+I+J+3)(I-F+J+1)(I-F+J+2)]^{1/2}, (5.20)$$

$$G_4 = [(F-I+J+1)(F-I+J+2)(F+I-J-1)(F+I-J)]^{1/2}$$
, (5.21)

The possible values of F are J+5/2, J+3/2,....|J-5/2|.

A computer program was written to carry out this calculation for each vibrational state (v=0 and v=1). Then, using the center frequency of the ν_1 state, the vibrational frequencies were calculated. The selection rules used for this calculation are listed below.

$$\Delta K = 0$$
; $\Delta J = 0$, ± 1 ; $\Delta F = same$ as ΔJ

A list of parameters used in the calculation are given in Table 5.1. The parameters were obtained from an IR-MW double resonance study by Jones et al. (13,14) and from a double resonance experiment done by Fawzy and Schwendeman (15).

Lineshape Analysis and Generation

To generate the lineshape of the three-level double resonance signal the density matrix equation of motion must be used. This equation can be written as,

$$\dot{\rho} = -\frac{i}{\hbar} (H\rho - \rho H) - k\Delta\rho . \qquad (5.22)$$

Here, $\dot{\rho}$ is the partial derivative with respect to time of the density matrix. Each diagonal element of the density matrix ρ , when multiplied by the total number of molecules in the sample, represents a "population" of that particular state. Also, H is the Hamiltonian of the molecule, k is the relaxation rate, and $k\Delta\rho$ is an extra term added to account for the relaxation. For simplicity, H is divided into two parts $H^{(0)}$, the contribution from the vibration-rotation energies, and $H^{(1)}$, the contribution from the interaction

119

Table 5.1 Parameters for CF_3I Ground State and v_1 Band.

	Ground State	v_1 Band
ν _{vib}	$0.0 (cm^{-1})$	1075.191 cm^{-1}
eQq	-2140.464 MHz	-2145.214 MHz
В	1517.50 MHz	1523.26 MHz
D _J	0.001 KHz	0.002 KHz
D _{JK}	0.006 KHz	0.006 KHz
D _K	0.000 KHz	0.000 KHz

References (14,15).

between the molecules and the two radiant beams,

$$H = H^{(0)} + H^{(1)}.$$
 (5.23)

Then, in a basis that diagonalizes $H^{(0)}$,

$$\mathbf{H}_{\mathbf{j}\mathbf{k}}^{(0)} = \delta_{\mathbf{j}\mathbf{k}}\mathbf{H}_{\mathbf{j}\mathbf{j}}^{(0)} \tag{5.24}$$

and

$$H_{jk}^{(1)} = -\mu_{jk} (\epsilon_1 \cos \omega_1 t + \epsilon_2 \cos \omega_2 t). \qquad (5.25)$$

Here, \mathcal{E}_1 is the amplitude of the electric field and ω_1 is the frequency of the microwave radiation; and \mathcal{E}_2 and ω_2 are the corresponding quantities for the infrared radiation. The indices j and k are confined to a, b, and c for the three levels involved; the energy level diagram used for this calculation is shown in Figure 5.1. Only $\mu_{ab} = \mu_{ba}$ and $\mu_{bc} = \mu_{cb}$ are non-zero and it is assumed that $\omega_1 = \omega_{ba}$ and $\omega_2 = \omega_{cb}$ where $\omega_{jk} = (\mathcal{E}_j - \mathcal{E}_k)/h$.

The matrix elements for the equation of motion of the density matrix are as follows:

$$\dot{\rho}_{aa} = -\frac{i}{\hbar} (H_{ab}^{(1)} \rho_{ba} - \rho_{ab} H_{ba}^{(1)}) - k_{aa} \Delta \rho_{aa}$$
 (5.26)

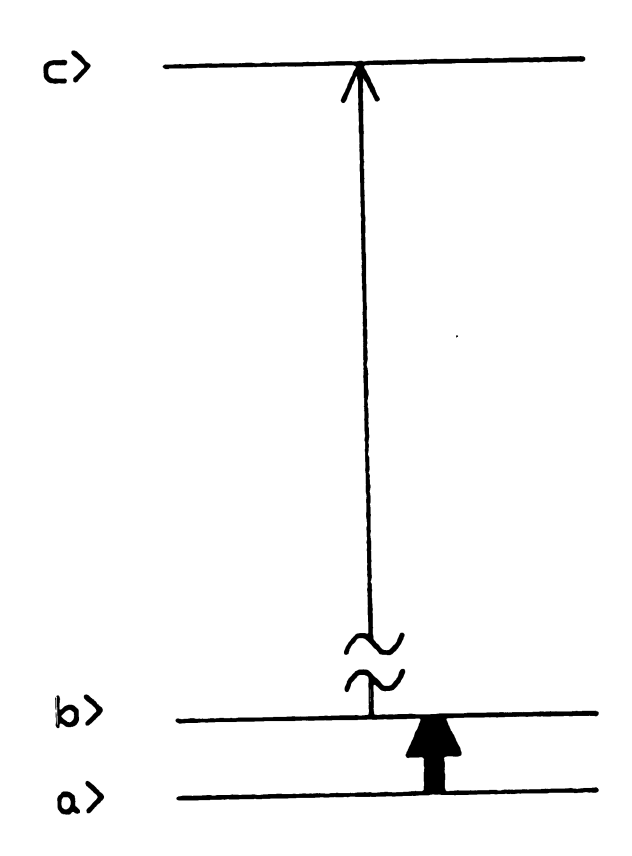


Figure 5.1. Three level energy diagram used for density matrix calculation.

$$\dot{\rho}_{bb} = -\frac{i}{\hbar} (H_{ba}^{(1)} \rho_{ab} + H_{bc}^{(1)} \rho_{cb} - \rho_{ba} H_{ab}^{(1)} - \rho_{bc} H_{cb}^{(1)}) - k_{bb} \Delta \rho_{bb}$$
 (5.27)

$$\dot{\rho}_{cc} = -\frac{i}{\hbar} (H_{cb}^{(1)} \rho_{bc} - \rho_{cb} H_{bc}^{(1)}) - k_{cc} \Delta \rho_{cc}$$
 (5.28)

$$\dot{\rho}_{ba} = - (i\omega_{ba} + k_{ba})\rho_{ba} - \frac{i}{\hbar} (H_{ba}^{(1)}\rho_{aa} + H_{bc}^{(1)}\rho_{ca} - \rho_{bb}H_{ba}^{(1)}) (5.29)$$

$$\dot{\rho}_{cb} = - (i\omega_{cb} + k_{cb})\rho_{cb} - \frac{i}{\hbar} (H_{cb}^{(1)}\rho_{bb} - \rho_{cc}H_{cb}^{(1)} - \rho_{ca}H_{ab}^{(1)}) \quad (5.30)$$

$$\dot{\rho}_{ca} = - (i\omega_{ca} + k_{ca})\rho_{ca} - \frac{i}{\hbar} (H_{cb}^{(1)}\rho_{ba} - \rho_{cb}H_{ba}^{(1)}) \qquad (5.31)$$

Now we make the substitutions,

$$P_{ba} = d_{ba}e^{-i\omega}l^{t}, \qquad (5.32)$$

$$\rho_{ch} = d_{ch}e^{-i\omega}2^{t}, \qquad (5.33)$$

$$\rho_{ca} = d_{ca} e^{-i(\omega_1 + \omega_2)t},$$
 (5.34)

and introduce the Rabi frequencies,

$$x_1 = \frac{\mu_{ab}^{\xi} 1}{\hbar}$$
 and $x_2 = \frac{\mu_{bc}^{\xi} 2}{\hbar}$. (5.36)

We can then write the following equations for the matrix elements by applying the rotating wave approximation:

$$\dot{\rho}_{aa} = \frac{i x_1}{2} (d_{ba} - d_{ab}) - k_{aa} \Delta \rho_{aa} \qquad (5.37)$$

$$\dot{\rho}_{bb} = \frac{i x_1}{2} (d_{ab} - d_{ba}) + \frac{i x_2}{2} (d_{cb} - d_{bc}) - k_{bb} \Delta \rho_{bb}$$
 (5.38)

$$\dot{\rho}_{cc} = \frac{i \times 2}{2} (d_{bc} - d_{cb}) - k_{cc} \Delta \rho_{cc} \qquad (5.39)$$

$$\dot{d}_{ba} = i(\omega_1 - \omega_{ba})d_{ba} + \frac{i x_1}{2} (\rho_{aa} - \rho_{bb}) + \frac{i x_2}{2} d_{ca} - k_{ba}d_{ba}(5.40)$$

$$d_{cb} = i(\omega_2 - \omega_{cb})d_{cb} + \frac{i \times_2}{2}(\rho_{bb} - \rho_{cc}) + \frac{i \times_1}{2}d_{ca} - k_{cb}d_{cb}$$
 (5.41)

$$d_{ca} = i(\omega_1 + \omega_2 - \omega_{ca})d_{ca} + \frac{i \times 2}{2}d_{ba} - \frac{i \times 1}{2}d_{cb} - k_{ca}d_{ca}$$
 (5.42)

Now, if we let $d_{ij} = d'_{ij} + id'_{ij}$ for i = a,b,c; $j = a,b,c \neq i$,

where dij and dij are both real,

$$d_{ha} - d_{ab} = 2id_{ha}^{'}$$
 (5.43)

Then, if we let $\Delta\omega_1 = \omega_1 - \omega_{ba}$ and $\Delta\omega_2 = \omega_2 - \omega_{cb}$,

the equations for the diagonal elements are reduced to the following form:

$$\dot{\rho}_{aa} = - x_1 d_{ba} - k_{aa} \Delta \rho_{aa} \qquad (5.44)$$

$$\dot{\rho}_{bb} = + x_1 d_{ba} - x_2 d_{cb} - k_{bb} \Delta \rho_{bb} \qquad (5.45)$$

$$\dot{\rho}_{CC} = x_2 d_{CD}^{*} - k_{CC} \Delta \rho_{CC} \qquad (5.46)$$

Since $\rho_{aa} + \rho_{bb} + \rho_{cc}$ contains no radiation terms, we let $\Delta_1 = \rho_{aa} - \rho_{bb}$, $\Delta_2 = \rho_{bb} - \rho_{cc}$,

and separate each d value into a real and imaginary part to get 8 equations for the matrix elements. These are

$$\dot{\Delta}_{1} = -2 x_{1} d_{ba}^{...} + x_{2} d_{cb}^{...} - k_{11} (\Delta_{1} - \Delta_{1}^{0}) - k_{12} (\Delta_{2} - \Delta_{2}^{0}), \quad (5.47)$$

$$\dot{\Delta}_{2} = x_{1} d_{ba}^{\prime \prime} - 2x_{2} d_{cb}^{\prime \prime} - k_{21} [\Delta_{1} - \Delta_{1}^{0}) - k_{22} (\Delta_{2} - \Delta_{2}^{0}), \qquad (5.48)$$

$$\dot{d}_{ba}' = -\Delta \omega_1 d_{ba}' - \frac{\kappa_2}{2} d_{ca}' - k_{ba} d_{ba}',$$
 (5.49)

$$\dot{d}_{ba}' = \Delta \omega_1 d_{ba}' + \frac{x_1}{2} \Delta_1 + \frac{x_2 d_{ca}}{2} - k_{ba} d_{ba}',$$
 (5.50)

$$d_{cb} = -\Delta \omega_2 d_{cb} + \frac{x_1}{2} d_{ca} - k_{cb} d_{cb}$$
, (5.51)

$$\dot{d}_{cb}^{..} = \Delta \omega_2 \dot{d}_{cb}^{.} + \frac{x_2}{2} \Delta_2 - \frac{x_1}{2} \dot{d}_{ca}^{.} - k_{cb} \dot{d}_{cb}^{..},$$
 (5.52)

$$d_{ca} = -(\Delta \omega_1 + \Delta \omega_2) d_{ca} + \frac{x_2}{2} d_{ba} - \frac{x_1}{2} d_{cb} - k_{ca} d_{ca},$$
 (5.53)

$$\dot{d}_{ca}'' = (\Delta \omega_1 + \Delta \omega_2) d_{ca}' + \frac{x_2}{2} d_{ba}' - \frac{x_1}{2} d_{cb}' - k_{ca} d_{ca}''.$$
 (5.54)

In these equations,

$$k_{11} = (2k_{aa} + k_{bb})/3$$

$$k_{22} = (k_{bb} + 2k_{cc})/3$$

$$k_{21} = (k_{cc} - k_{bb})/3$$

$$k_{12} = (k_{aa} - k_{bb})/3$$

Now, we set all of the time derivatives to 0 (i.e., assume a steady state). Then, we can write the equation in matrix form,

$$AL = C. (5.55)$$

Here, the matrices A, L, and C are (5.56)

$$\mathbf{A} = \begin{bmatrix} \mathbf{k}_{11} & 0 & 2\mathbf{x}_{1} & 0 & 0 & \mathbf{k}_{12} & 0 & -\mathbf{x}_{2} \\ 0 & \mathbf{k}_{ab} & -\Delta\omega_{1} & 0 & -\mathbf{x}_{2}/2 & 0 & 0 & 0 \\ -\mathbf{x}_{1}/2 & -\Delta\omega_{1} & \mathbf{k}_{ab} & -\mathbf{x}_{2}/2 & 0 & 0 & 0 & 0 \\ 0 & 0 & \mathbf{x}_{2}/2 & \mathbf{k}_{ca} & \Delta\omega_{3} & 0 & 0 & -\mathbf{x}_{1}/2 \\ 0 & -\mathbf{x}_{2}/2 & 0 & -\Delta\omega_{3} & \mathbf{k}_{ca} & 0 & \mathbf{x}_{1}/2 & 0 \\ \mathbf{k}_{21} & 0 & -\mathbf{x}_{1} & 0 & 0 & \mathbf{k}_{22} & 0 & 2\mathbf{x}_{2} \\ 0 & 0 & 0 & 0 & -\mathbf{x}_{1}/2 & 0 & \mathbf{k}_{cb} & \Delta\omega_{2} \\ 0 & 0 & 0 & \mathbf{x}_{1}/2 & 0 & -\mathbf{x}_{2}/2 & -\Delta\omega_{2} & \mathbf{k}_{cb} \end{bmatrix}$$

$$L^{T} = (\Delta_{1}, d_{ba}, d_{ba}, d_{ca}, d_{ca}, d_{ca}, d_{cb}, d_{cb})$$
 (5.57)

$$c^{T} = (-k_{11}\Delta_{1}^{0} - k_{12}\Delta_{2}^{0}, 0, 0, 0, -k_{21}\Delta_{1}^{0} - k_{22}\Delta_{2}^{0}, 0, 0)$$
 (5.58)

With this system the matrix elements of L can be calculated. By using the correct density matrix elements the absorption coefficients can be found.

Absorption Coefficient

The absorption coefficient (γ) is related to the inquadrature component of the polarization with frequency ω_2 ($P_{\bf g}^{~(2)}$) by the following equation:

$$\gamma = -\left(\frac{4\pi\omega}{c}\right)\left(\frac{p_s^{(2)}}{s}\right). \tag{5.59}$$

To calculate γ from the density matrix ρ , we use

$$\underline{P} = N \text{ tr}(\rho_{\underline{V}}). \qquad (5.60)$$

For the three level system described above we get

$$P = N[\mu_{ha} (\rho_{ha} + \rho_{ab}) + \mu_{ch} (\rho_{cb} + \rho_{bc})] . \qquad (5.61)$$

Since,

$$\rho_{ba} = (d_{ba} + id_{ba}) e^{-i\omega} l^{t} \quad \text{and} \quad (5.62)$$

$$\rho_{ab} = (d_{ba}' - id_{ba}') e^{+i\omega} l^{t}, \qquad (5.63)$$

$$\rho_{ba} + \rho_{ab} = d_{ba}(e^{-i\omega}l^t + e^{i\omega}l^t) + id_{ba}(e^{-i\omega}l^t - e^{i\omega}l^t)$$

$$= 2d_{ba}\cos\omega_l t + 2d_{ba}\sin\omega_l t .$$
(5.64)

Also,

$$P_{cb} = (d_{cb}' + id_{cb}') e^{-i\omega_2 t}, \qquad (5.65)$$

$$\rho_{bc}^{=} (d_{cb}^{\prime} + id_{cb}^{\prime\prime}) e^{i\omega_2 t},$$
 (5.66)

$$\rho_{cb} + \rho_{bc} = 2d_{cb}^{*} \cos \omega_{2} t + 2d_{cb}^{*} \sin \omega_{2} t , \qquad (5.67)$$

80

$$P = 2N \left[\mu_{ba} (d_{ba}^{\dagger} cos \omega_{l} t + d_{ba}^{\dagger} sin \omega_{l} t) + \mu_{cb} (d_{cb}^{\dagger} cos \omega_{2} t + d_{cb}^{\dagger} sin \omega_{2} t) \right].$$

$$(5.68)$$

Here P equals the induced polarization of the sample. This oscillation of the polarization leads to emission, which has the form

$$E_{s} = 2N \frac{\pi\omega_{1}!}{c} \left[\mu_{ba}(d_{ba}^{\dagger}\sin\omega_{1}t - d_{ba}^{\dagger}\cos\omega_{1}t) + 2N \frac{\pi\omega_{2}!}{c} \mu_{cb}(d_{cb}^{\dagger}\sin\omega_{2}t - d_{cb}^{\dagger}\cos\omega_{2}t) \right]$$

$$(5.69)$$

At the infrared detector this emission beats with the infrared radiation of frequency ω_2 . The output of the detector is proportional to the component of the product of E_s and E_{IR} that has zero frequency. This component is proportional to $\mu_{cb}d_{cb}$. Therefore, with this information the absorption coefficient can be calculated.

$$\gamma = \frac{8\pi\omega_2}{c\epsilon_0} \quad (N_{\mu_{cb}} d_{cb}^{\ cb}) \tag{5.70}$$

Equation (5.70) calculates the absorption at the infrared detector.

In the infrared region the Doppler effect is very important, and therefore Doppler averaging must be done for a proper lineshape. This is carried out by convoluting a Gaussian function with the data obtained in the absorption coefficient calculation. The Doppler averaging equation can be written as

$$\bar{\gamma}_{I} = \int_{-\infty}^{\infty} \gamma_{I} f(v) dv . \qquad (5.71)$$

Here,

$$f(v) = \frac{1}{\sqrt{\pi u^2}} e^{-v^2/\mu^2}$$
 (5.72)

with
$$\mu^2 = 2k_BT/M$$
 . (5.73)

Here, v is the component of the velocity of the molecule in the direction of the radiation, γ_I is the absorption coefficient calculated for $\omega_2 = \omega_2^{\ 0} (1-v/c)$, k_B is Boltzmann's

constant, T is the absolute temperature, and M is the molecular mass. Since the lineshape of interest is in the frequency domain, the Doppler averaging was carried out in the frequency domain. The result is

$$\bar{\gamma}_{I} = \int_{-\infty}^{\infty} f(\nu) \gamma_{I} d\nu , \qquad (5.74)$$

where
$$f(\nu) = \frac{1}{\sqrt{\pi \sigma^2}} \exp(-\nu^2/\sigma^2)$$
 (5.75)

with
$$\sigma = \Delta v_D / \sqrt{\ln 2}$$
 and $v = \omega_2 v / 2\pi c$. (5.76)

Here $\Delta \nu_D$ is the Doppler half-width at half-height. The integration was done numerically and carried out to three Doppler widths from the center frequency. This calculation was done for many different Rabi frequencies and pressures by the computer program, DBRSIR, written in FORTRAN for the VAX computer. The lineshape shown in Figure 5.2 was calculated with the following parameters:

Infrared Rabi frequency = 0.001 MHz

Microwave Rabi frequency = 100.0 MHz

Population difference for IR transition = 0.99

Population difference for MW transition = 0.004

Doppler half width at half max. = 34.5 MHz

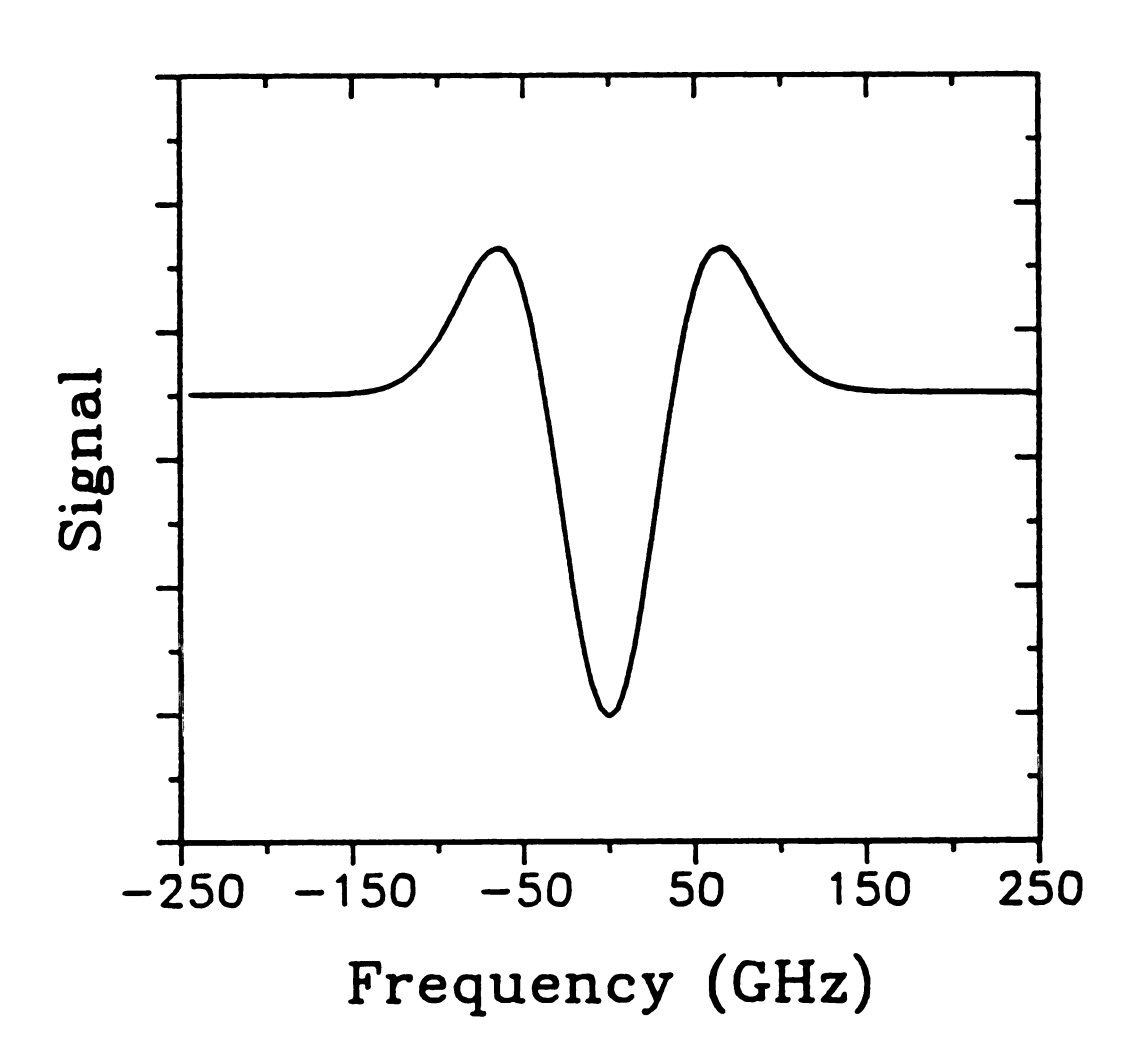


Figure 5.2. Calculated lineshape using a Rabi frequency of 100 MHz for the pumping radiation.

Relaxation rates for all transitions = 3 MHz.

The results of additional calculations with this program will be described below.

5.3 Experimental

CO₂ Sideband Laser

The infrared-microwave double resonance experiment described below was accomplished by using a CO₂ sideband laser system for the infrared source. The CO₂ sideband laser was described in Chapter 4. A diagram of the spectrometer used is shown in Figure 5.3. The CO₂ sideband laser was used in the tunable traveling wave mode; therefore, the infrared power was very low.

The microwave radiation used for sideband generation was phase locked by a Hewlett Packard model 8709A synchronous detector to a harmonic of the output from a PTS model 500-M7010 radiofrequency synthesizer. This scheme of locking was explained in Chapter 4. The only difference is that in this case the microwave frequencies are referenced to the PTS synthesizer instead of to the Hewlett Packard synthesizer. The frequency of the CO₂ laser is locked to the Lamb dip in the fluorescence from an extracavity cell that contains CO₂.

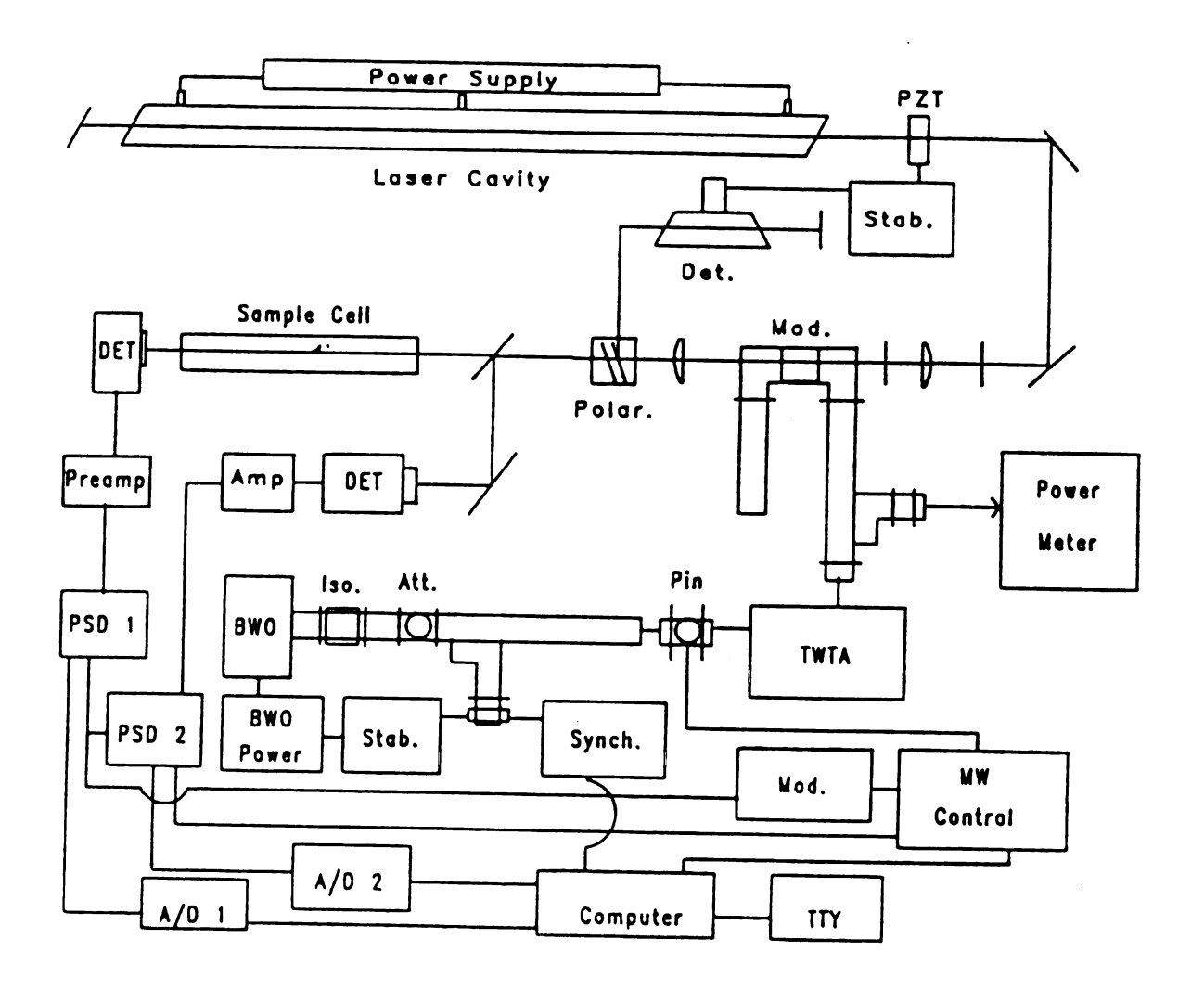


Figure 5.3. Block diagram of CO_2 sideband laser spectrometer.

For the double resonance experiment, the sideband laser beam is not modulated and the radiation is not divided into reference and signal beams. The power of the sideband radiation is still kept constant, however, by controlling the microwave power applied to the electrooptic modulator.

The detector used as the reference is a microwave power meter thermistor head connected to a microwave power meter. The thermistor samples the microwave power by means of a directional coupler after the traveling wave tube amplifier (TWTA). The voltage output from the power meter is sent to the PIN diode control circuit which adjusts the microwave power by controlling the attenuation by the PIN diode. This experimental setup controls the sideband power only by controlling the microwave fluctuations; therefore CO₂ laser fluctuations have no effect on the reference loop and are not taken into account. The reason for the changes in control are to allow modulation by chopping the microwave pumping radiation.

Microwave Pump

The microwave (pump) radiation source was a Varian backward wave oscillator (BWO). The BWO was phase locked by a Hewlett Packard synchronous detector to a harmonic from a HP 8455A reference oscillator, as described in Chapter 4.

The microwaves were then amplified by a Varian traveling wave tube amplifier (TWTA). The microwave radiation was 100% amplitude modulated at 33.3 kHz by a PIN diode, as explained in Chapter 4, but the microwave frequency was not swept. To reduce fluctuations, the microwave radiation was monitored at the output of the TWTA by a thermistor through a directional coupler (40 db total attenuation). The output of the power meter was sent to a PIN diode control circuit similar to that described above. This kept the microwave power constant and reduced the noise at the IR detector.

Double Resonance Spectrometer

The double resonance specrometer is shown in Figure 5.4. The pumping microwaves were modulated and the infrared signal was processed at the modulation frequency by a lockin amplifier. The signal at the output of the lock-in amplifier was the difference between the infrared signals with the microwave pump on and off. The signal was sent to an analog to digital converter and stored in a PDP-8 computer. The spectrometer was computer controlled as disscussed in Chapter 4. The microwave cell used for the double resonance experiment is the cavity cell explained in Chapter 3 and is shown again in Figure 5.5. This cell is a cavity cell which increases the electric field inside if

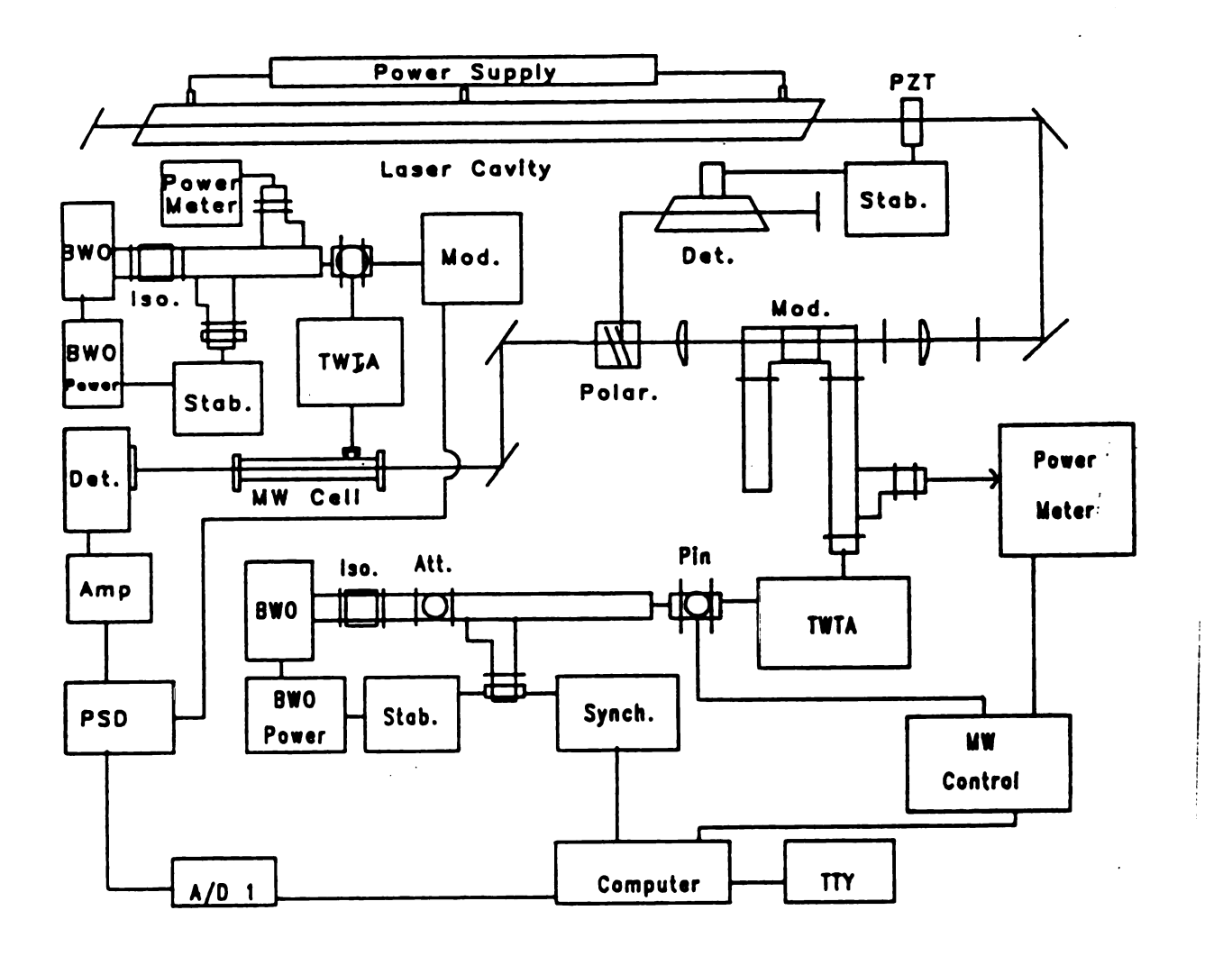


Figure 5.4. Block diagram of infrared microwave double resonance spectrometer.

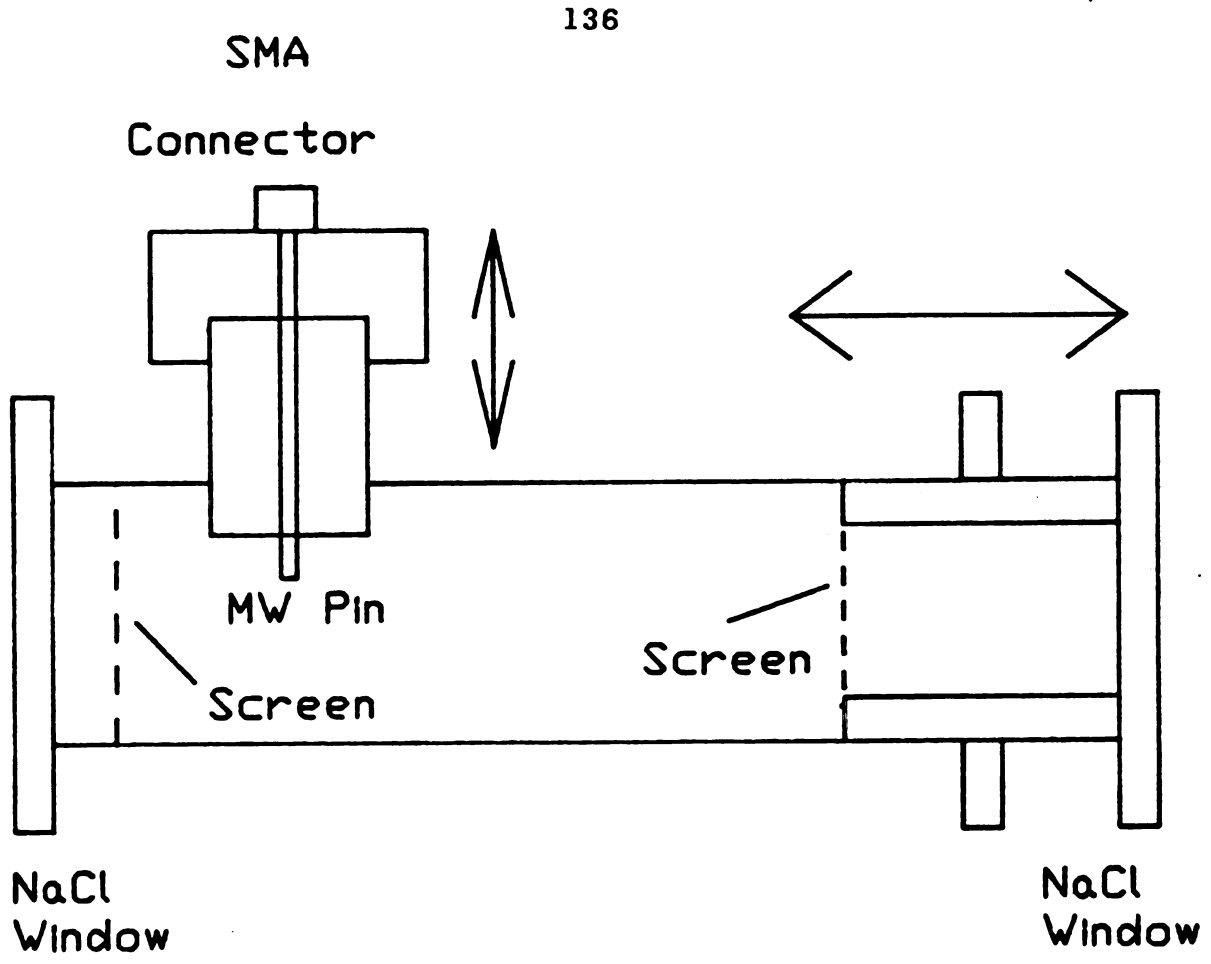


Figure 5.5. Resonance cavity cell used in infrared microwave double resonance experiment to obtain high microwave fields.

adusted to the proper dimensions. The adjustment is made by minimizing the reflected power back from the cell as explained in Chapter 3.

5.4 Results and Discussion

Infrared-Microwave Double Resonance in ${ m CH_3OH}$

The essential results of the CH₃OH infrared microwave double resonance study are shown in Table 5.2. Here the experimental results are compared to values calculated by using Henningsen's parameters (10,11). Of the 8 transitions listed, four are Q branch transitions that had not been experimentally determined before.

The number of transitions is somewhat limited by the constraints listed below: The infrared source used is limited to a spectral coverage of ±(8 - 18 GHz) from each CO₂ laser line. The microwave pumping source used had to be in the other microwave band from that of the sideband microwave generator; i.e., if the X-band (8.0 - 12.4 GHz) microwave generator was used for sidebands, then the P-band (12.4 - 18.0 GHz) generator was used for the pumping microwave and vice versa. This was because our laboratory has only one BWO in each region. Another reason for the limited number of double resonance signals is the rather large (~0.8 cm⁻¹) CH₃OH rotational constant (B). This allows only a small number of ground state rotational transitions to be pumped with an 8-18 GHz microwave source.

Figure 5.6 shows a one photon trace over a 1 GHz scan.

Table 5.2 CH₃OH Double Resonance Experiment Results.

139

Pump	Probe	Experiment	Theory 1
lower-upper	IR trans	(cm^{-1})	(cm^{-1})
(J,k)-(J,k)sym	$(J,k)\tau$, n, sym		
(2,0)-(3,1),E	R(2,0)2,1,E	1038.8316	1038.831
(4,1)-(4,1),A	R(4,1-)3,0,A	1041.7829	1041.789
$(4,3)-(5,2),A^+$	R(5,2-)2,0,A	1042.7351	1042.747
$(4,3)-(5,2),A^+$	R(5,2 ⁺)2,0,A	1042.7393	1042.739
$(4,3)-(5,2),A^+$	Q(5,2 ⁻)2,0,A	1033.1712	1033.175
(4,3)-(5,2),A ⁻	Q(5,2 ⁺)2,0,A	1033.1763	1033.175
(4,3)-(5,2),A ⁺	Q(4,3)1,0,A	1034.0357	1034.035
(2,0)-(3,1),E	Q(3,1)1,0,E	1034.2645	1034.264

¹ Theoretical predictions by J. O. Henningsen (10,11).

There are two absorption signals shown here. In Figure 5.7 the double resonance signal is given. The transition which has its lower energy level in common with one of the pumped ground state levels is present in the double resonance signal. The comparison between the two figures illustrates the selectivity of the double resonance experiment. The double resonance signal is considerably smaller than the one photon absorption signal; however, the signal to noise ratios for the two signals appear to be about the same. The reason for the decreased noise in the double resonance experiment is because we modulate the molecules in this experiment rather than modulate the source. Therefore the source noise contribution to the total noise of the signal is greatly reduced.

Infrared-Microwave Double Resonance in CF₃I

There have been many attempts to understand and assign the 10 μ m region of the CF₃I molecule; however, all of these attempts have met with limited success (12-17). The greatest progress was made by Jones et al., who used a double resonance technique to gain an understanding of the mid-infrared bands of CF₃I (13,14). What we had hoped to be able to do was to pump selectively the ground state rotational transitions and probe the ν_1 band transitions.

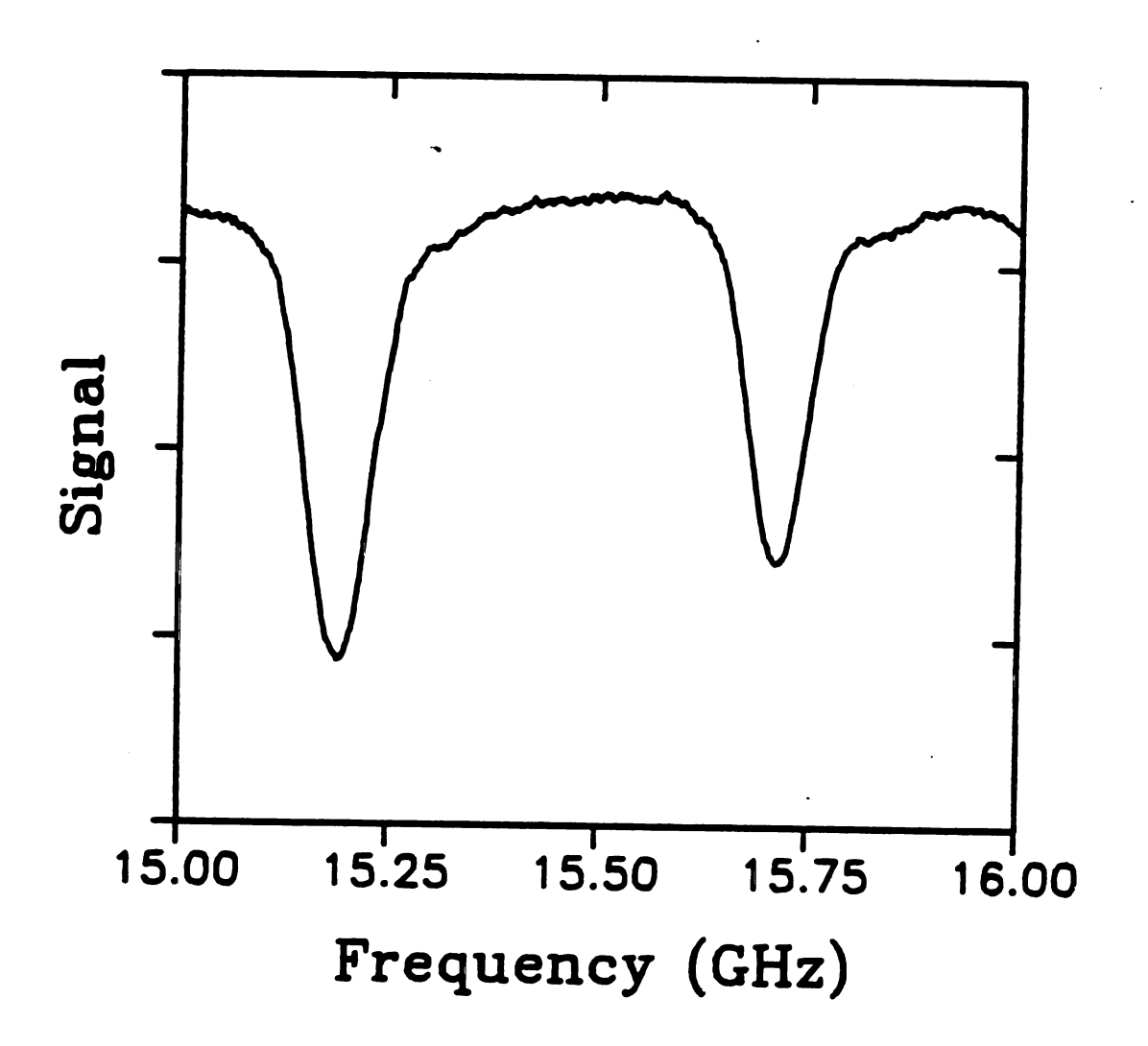


Figure 5.6. Absorption spectrum of CH_3OH . The CO_2 laser is on the 9P(24) laser line and the microwaves are swept from 15.0 to 16.0 GHz.

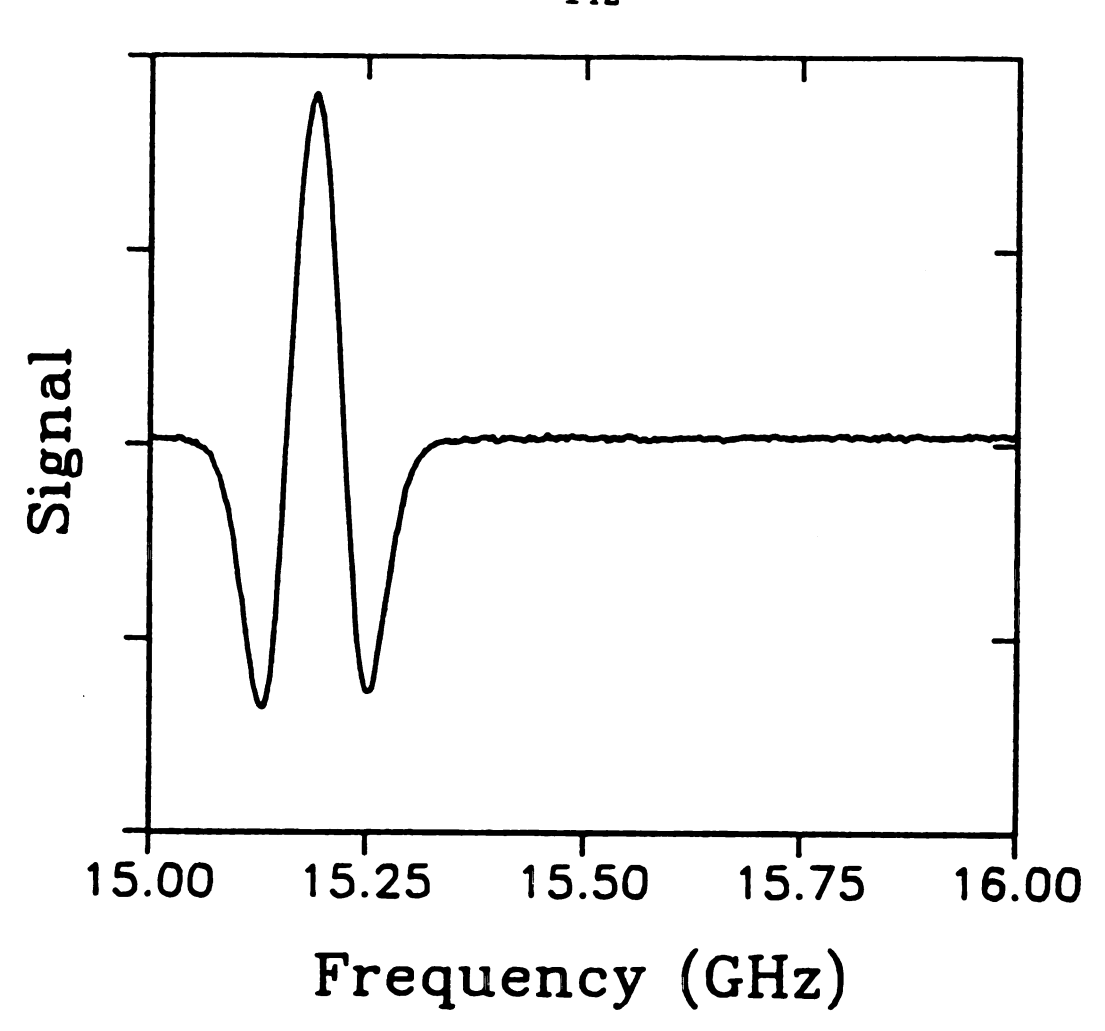


Figure 5.7. Double resonance spectrum of CH_3OH over the same region as Figure 6. This shows the selectivity of the double resonance technique.

The information about the ground state rotational transitions is already known, and could in principle assist in an assignment of the ν_1 band transitions. A plot of a typical infrared microwave double resonance spectrum obtained by our technique is shown in Figure 5.8. Unlike the CH₃OH study, Figure 5.8 shows many double resonance signals. Possible reasons for these groups of double resonance signals are discussed below.

To understand the signal seen we must first review the vibration rotation theory as applied to CF_3I . The hyperfine splitting associated with the quadrupole moment of the iodine nucleus greatly increases the complexity and number of the rotational transitions in the ground and vibrationally excited states of CF_3I . These transitions are closely spaced and because of the large Rabi frequency of the pumping radiation, more than one transition can be pumped at the same time.

An experiment was done on a methanol transition to determine the relationship between the microwave pumping radiation frequency and the ground state rotational transitions pumped. A plot was created of the lineshapes recorded at different microwave pumping frequencies. This is displayed in Figure 5.9. The results of the experiment show that a small signal still exists even with pumping ~300 MHz off resonance. The lineshape here also shows the off

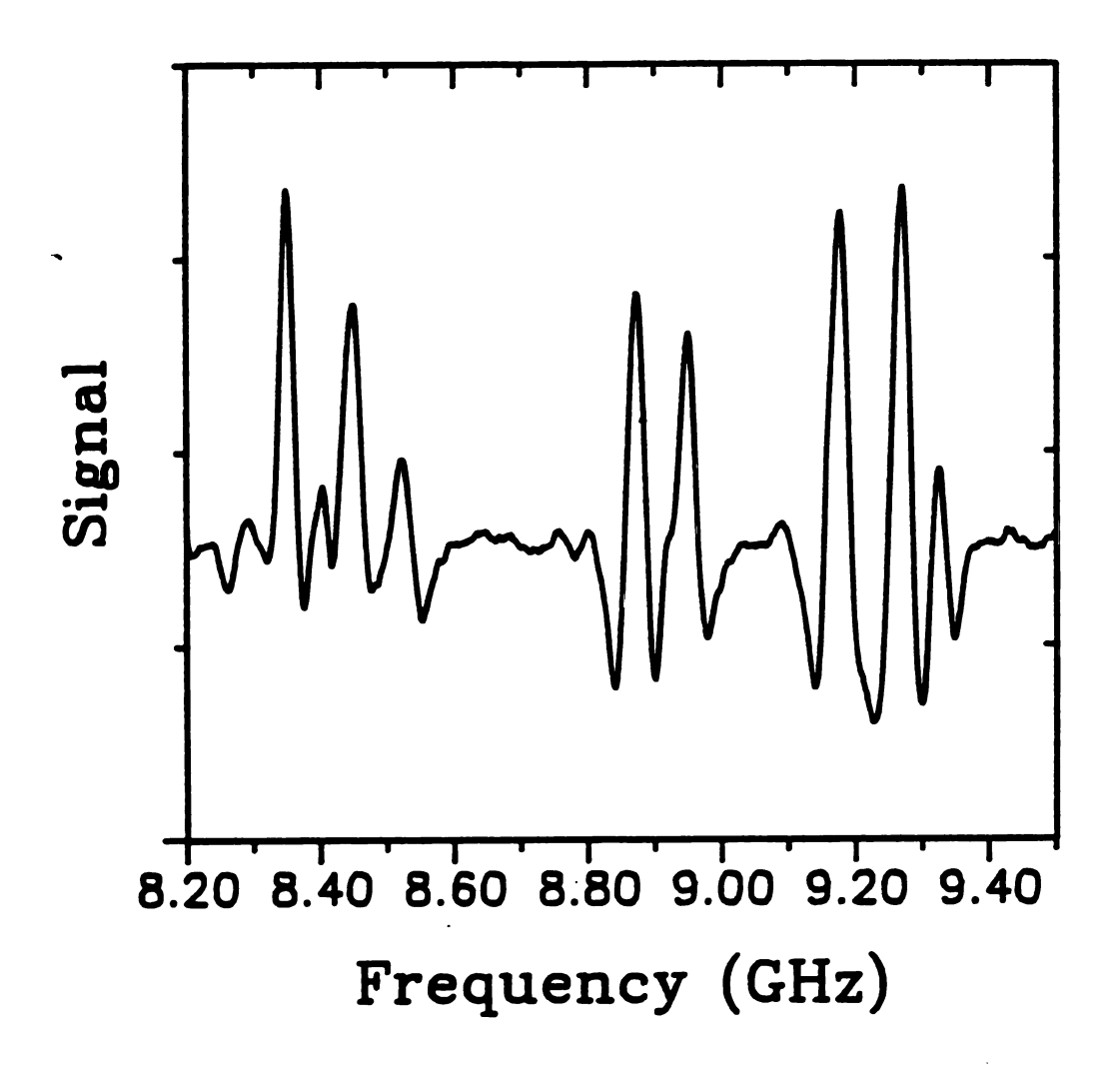
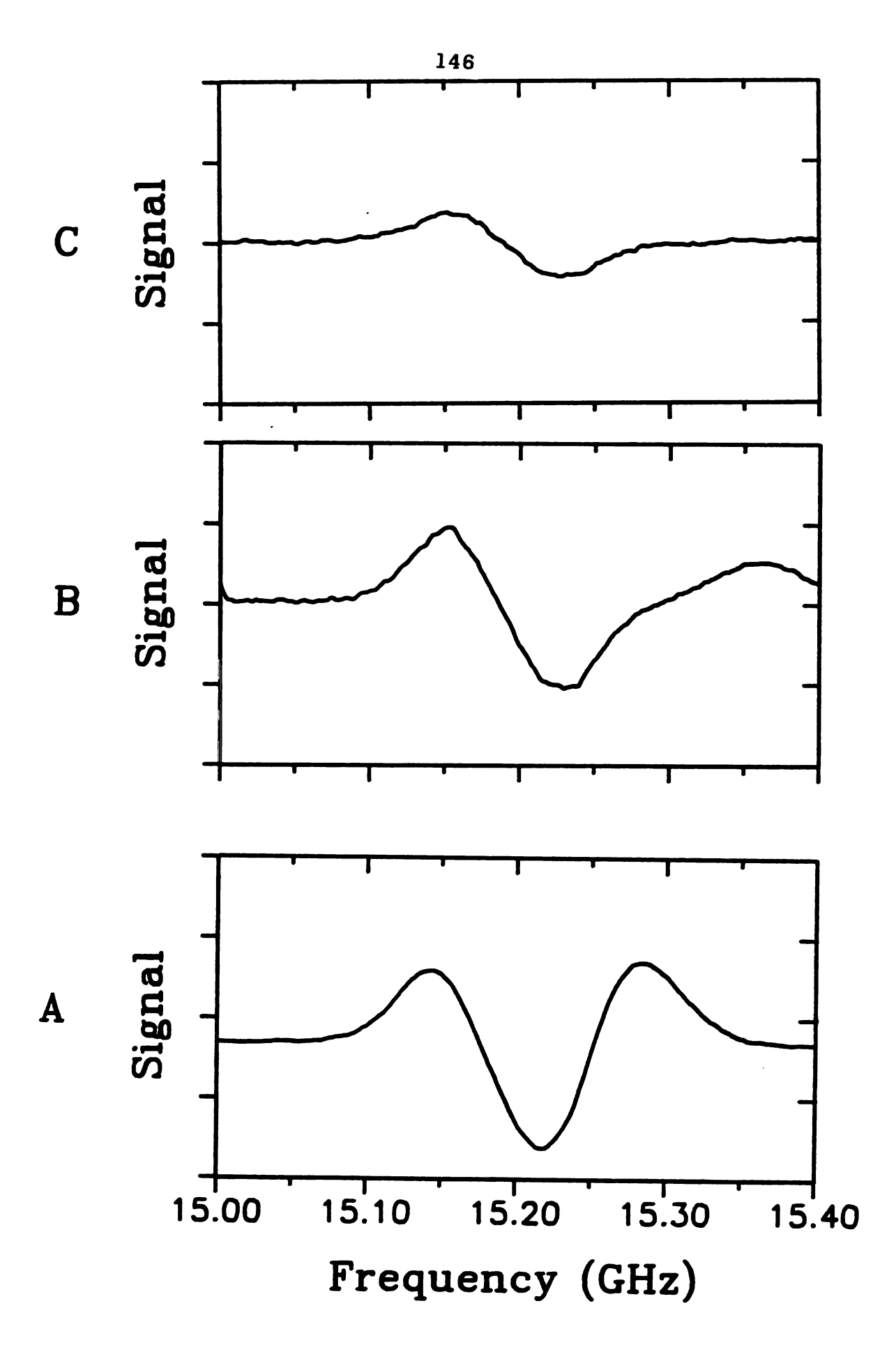


Figure 5.8. Infrared microwave double resonance spectrum of ${\rm CF_3I.}$ The ${\rm CO_2}$ laser is on the ${\rm 9R(16)}$ laser line. The pump frequency is 15,287.6 MHz.

Figure 5.9. Trace A shows the double resonance signal of CH₃OH with the pumping frequency on resonance with the pumped transition. Trace B is 150 MHz off resonance and Trace C is 300 MHz off resonance. The CO₂ laser is on the 9P(24) laser line.



resonance pumping effect. It should be noted here that the size of the Rabi frequency of the pumping radiation depends on both the electric field and the dipole transition moment for the pumped transition.

By using the method of energy calculations discussed in the theoretical section of this chapter, we can calculate the energy levels for CF_3I . A list of frequencies of the possible pumped transitions is shown in Table 5.3. The table illustrates the possiblity of multiple level pumping. This could contribute to the large number of double resonance signals seen.

The final reason for the complexity of the double resonance signal oberved is the large number of vibrational bands which overlap in the 10 µm region. These bands are fundamental, combination, and hot bands and their estimated center frequencies, as determined by previous experiments (18), are given in Table 5.4.

It is apparent that the double resonance signals and center frequencies cannot be easily determined under the conditions of the CF₃I case. For future reference, a series of plots is given for the CF₃I infrared microwave double resonance experiment. These are shown in Figures 5.8, 5.10, and 5.11.

Table 5.3 Pumped Ground State Rotational Transitions in ${\tt CF_3I}$.

		F1	Offset ²	
Lower-U		Frequency		
(J,k,F) -		(MHz)	(MHz)	
3,3,4.5		11990.763	-309.237	
3,3,3.5	4,3,4.5	12000.323	-299.677	
3,2,3.5	4,2,4.5	12097.288	-202.712	
3,0,1.5	4,0,2.5	12104.064	-195.936	
3,2,4.5	4,2,5.5	12106.689	-193.311	
3,0,2.5	4,0,3.5	12118.500	-181.500	
3,1,2.5	4,1,3.5	12126.159	-173.841	
3,1,1.5	4,1,2.5	12137.483	-162.517	
3,0,0.5	4,0,1.5	12140.427	-159.573	
3,1,3.5	4,1,4.5	12149.526	-150.474	
3,2,2.5	4,2,3.5	12151.686	-148.314	
3,0,3.5	4,0,4.5	12165.904	-134.096	
3,1,4.5	4,1,5.5	12186.965	-113.035	
3,1,0.5	4,1,1.5	12189.439	-110.561	
3,0,5.5	4,0,6.5	12202.991	-97.009	
3,3,2.5	4,3,3.5	12204.011	-95.989	
3,0,4.5	4,0,5.5	12215.800	-84.200	
3,1,5.5	4,1,6.5	12219.283	-80.717	
3,2,1.5	4,2,2.5	12243.071	-56.929	
3,2,5.5	4,2,6.5	12266.886	-33.114	
3,2,0.5		12339.021	+39.021	
	4,3,6.5		+42.283	
	4,3,2.5	12438.590	+138.590	
	4,3,1.5		+295.461	
-,-,	-,-, -			

Calculated by the program described in the text; the parameters are those in the first entry in Table 5.4.

Assuming pumping frequency of 12300.0 MHz.

149 Table 5.4 Parameters for CF $_3$ I Transitions in $10\,\mu m$ Region.

Band	v/cm^{-1}	B(MHz)	D _J (MHz)	D _{JK} (MHz)	eQq
g.s. ¹	0.0	1523.29	0.002	0.006	-2145.214
ν ₁ ²	1075.191	1517.50	0.001	0.006	-2140.464
4v3 3	1145.212	1520.69	0.005	0.015	-2147.65
2,5	1079.66	1516.67	0.000	0.008	-2145.214
4 ₂ 6	1046.0	1521.13	0.0015	0.006	-2142.91
ν _ω 3	1075.269	1516.53	0.013	0.006	-2145.214
ر ع پ	1074.78	1520.78	0.013	0.006	-2145.214
	1075.256	1514.90	0.002	0.006	-2145.214
ν ₆ +ν ₁ 3	1075.42	1516.95	0.001	0.006	-2145.214
ν ₅ +ν ₁ 3	1075.168	1512.43	0.000	0.006	-2145.214

Reference (19).

Reference (15).

Reference (14).

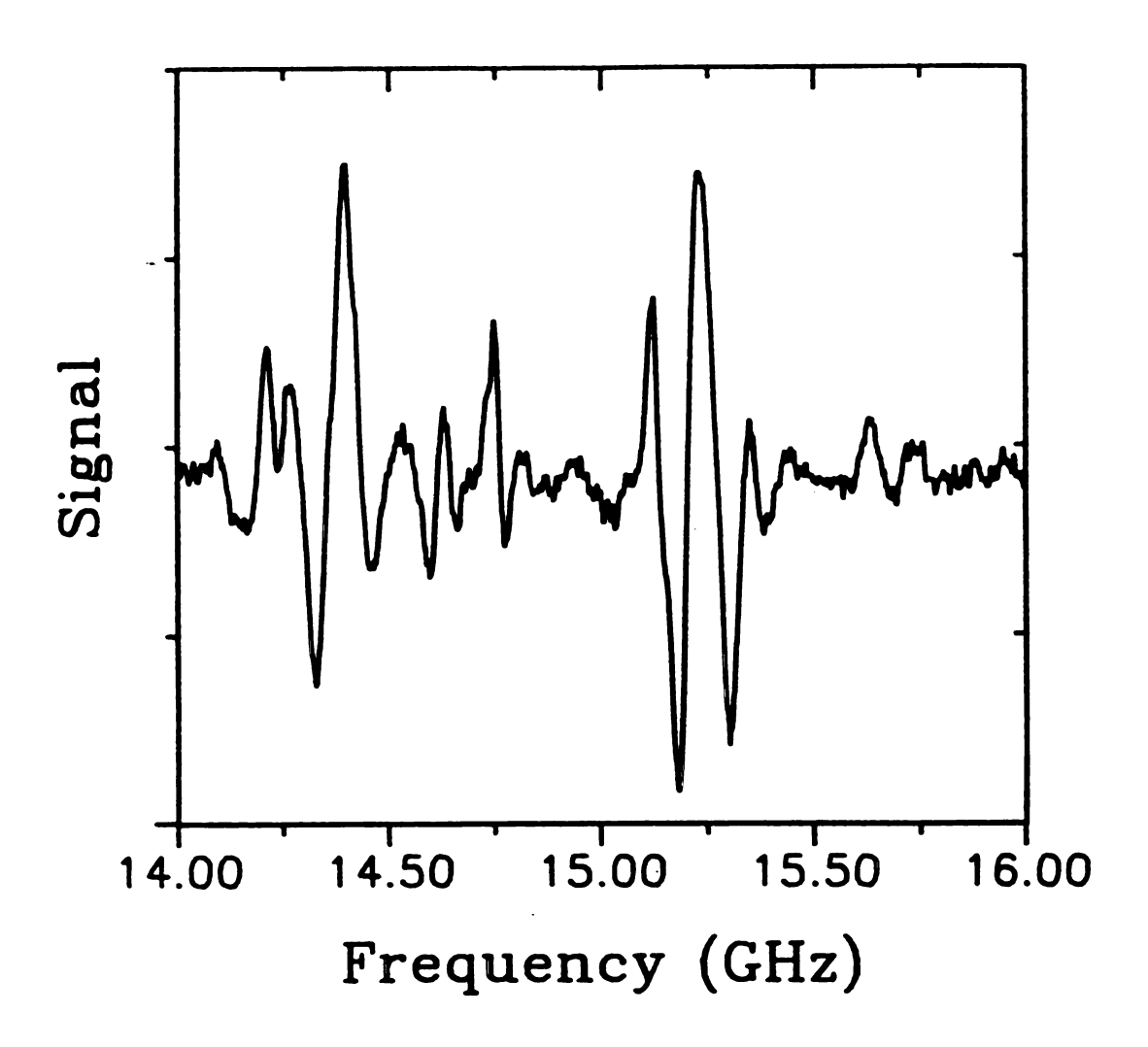


Figure 5.10. Infrared microwave double resonance spectrum of CF_3I . The CO_2 laser is on the 9R(16) laser line. The pumping frequency is 12,150.0 MHz.

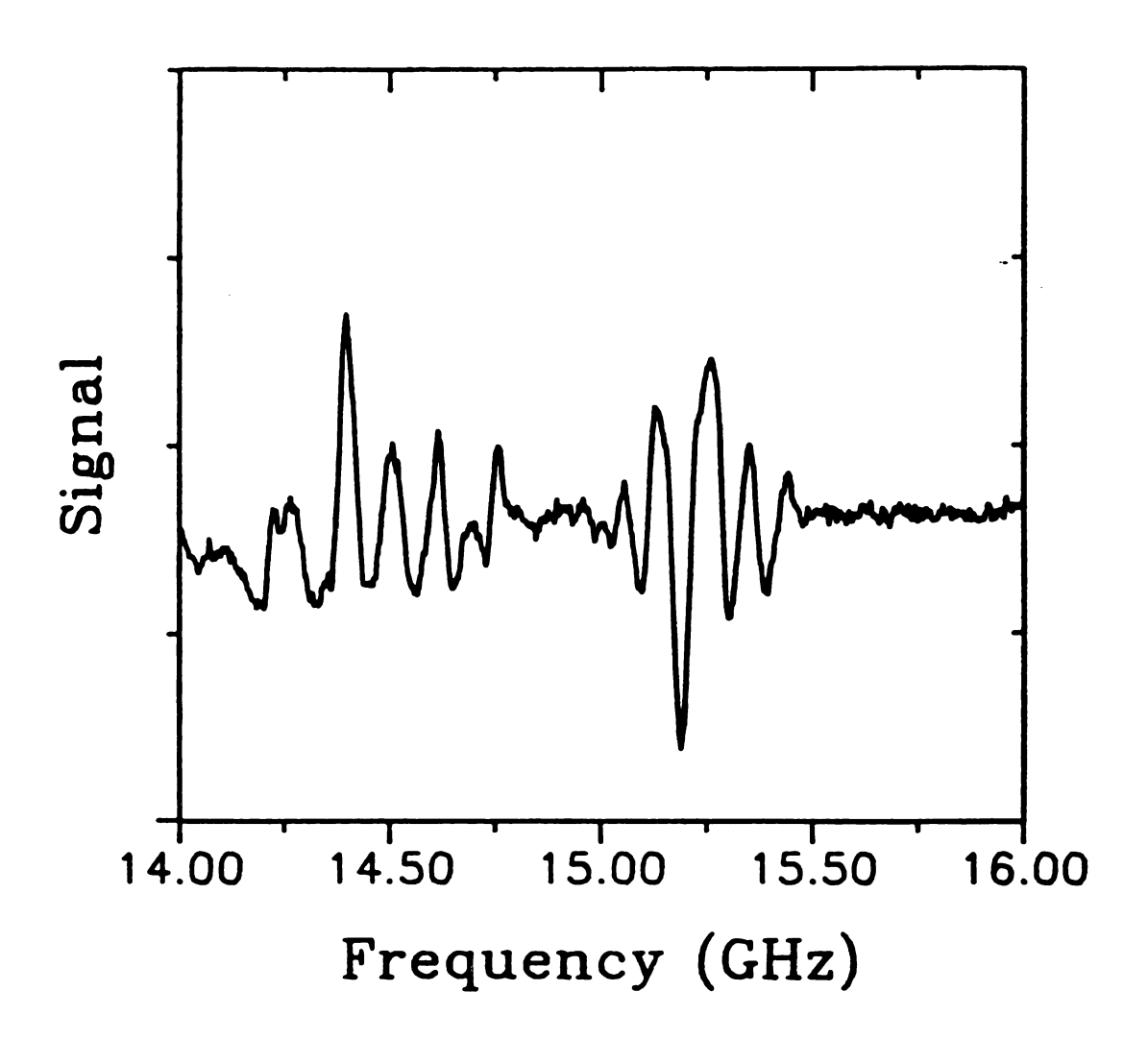


Figure 5.11. Infrared microwave double resonance spectrum of CF_3I . The CO_2 laser is on the 9R(16) laser line. The pumping frequency is 9,000.0 MHz.

сн3он

The theory for lineshape calculation of the double resonance signal was explained in the theoretical section above. By using the DBRSIR program with experimental data, we can approximate the Rabi frequencies involved in the pump. Figure 5.12 shows theoretically-calculated plots of double resonance effects vs. frequency for the Rabi frequencies of the microwave radiation. The largest signal shown here is at highest Rabi frequency; the smallest is at lowest Rabi frequency. One of the two trends in the lineshapes is an increase in signal amplitude with an increase in Rabi frequency. The second trend, which is less obvious, is variation of the splitting in the seven cases. By using this second feature the Rabi frequency for the pumped transition can be estimated.

An experiment was carried out on the R(4,1)A transition in CH₃OH to determine the effect of Rabi frequency on the lineshape. Figure 5.13 shows the results of this experiment. As the plot shows, there is a noticeable change in the signal as predicted by the double resonance calculation done earlier. With this reassurance that the theoretical prediction is experimentally observable, an experiment to obtain the electric field

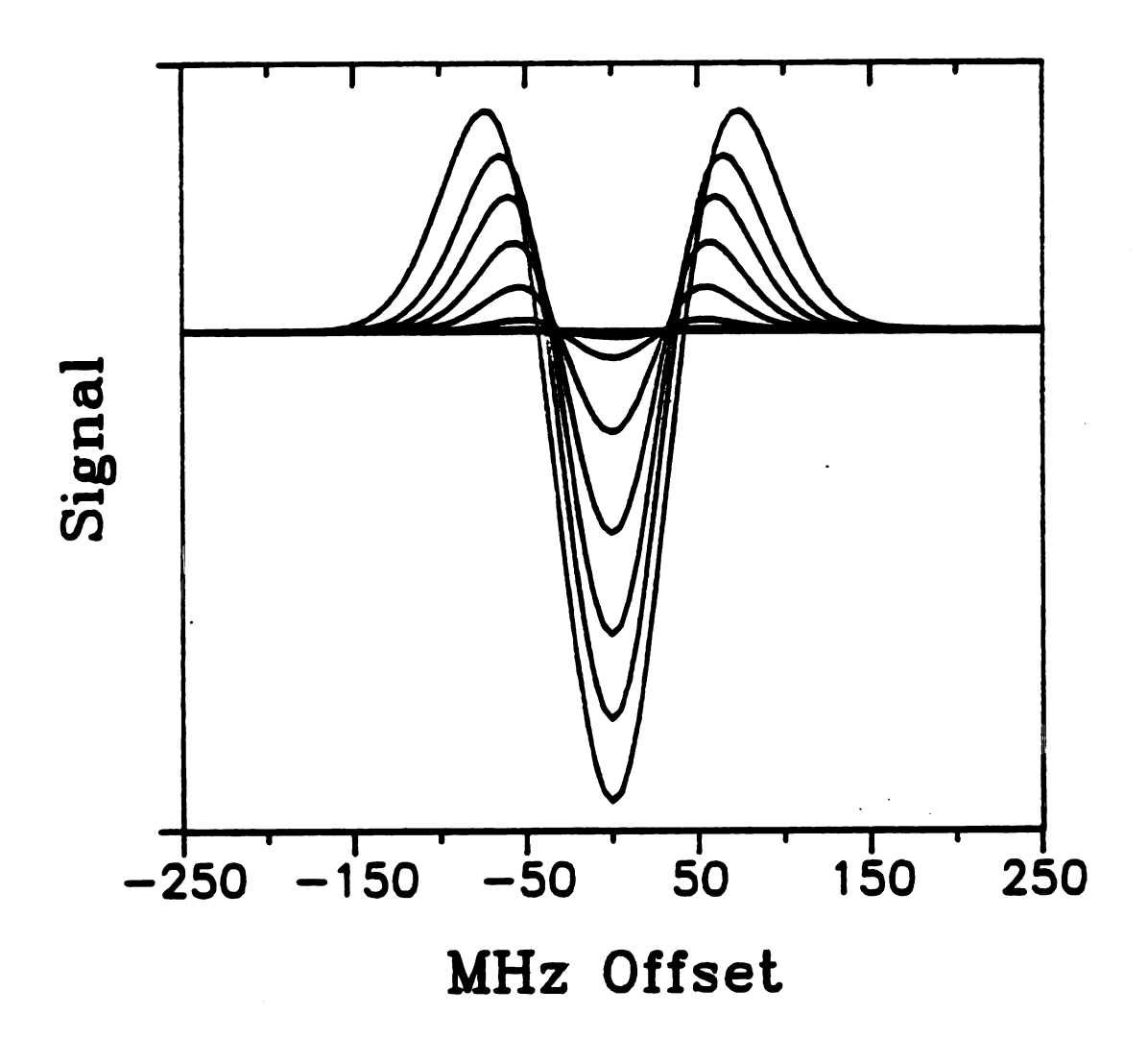


Figure 5.12. Calculated lineshape using different Rabi frequencies. The signal with the largest amplitude was generated using the largest Rabi frequency.

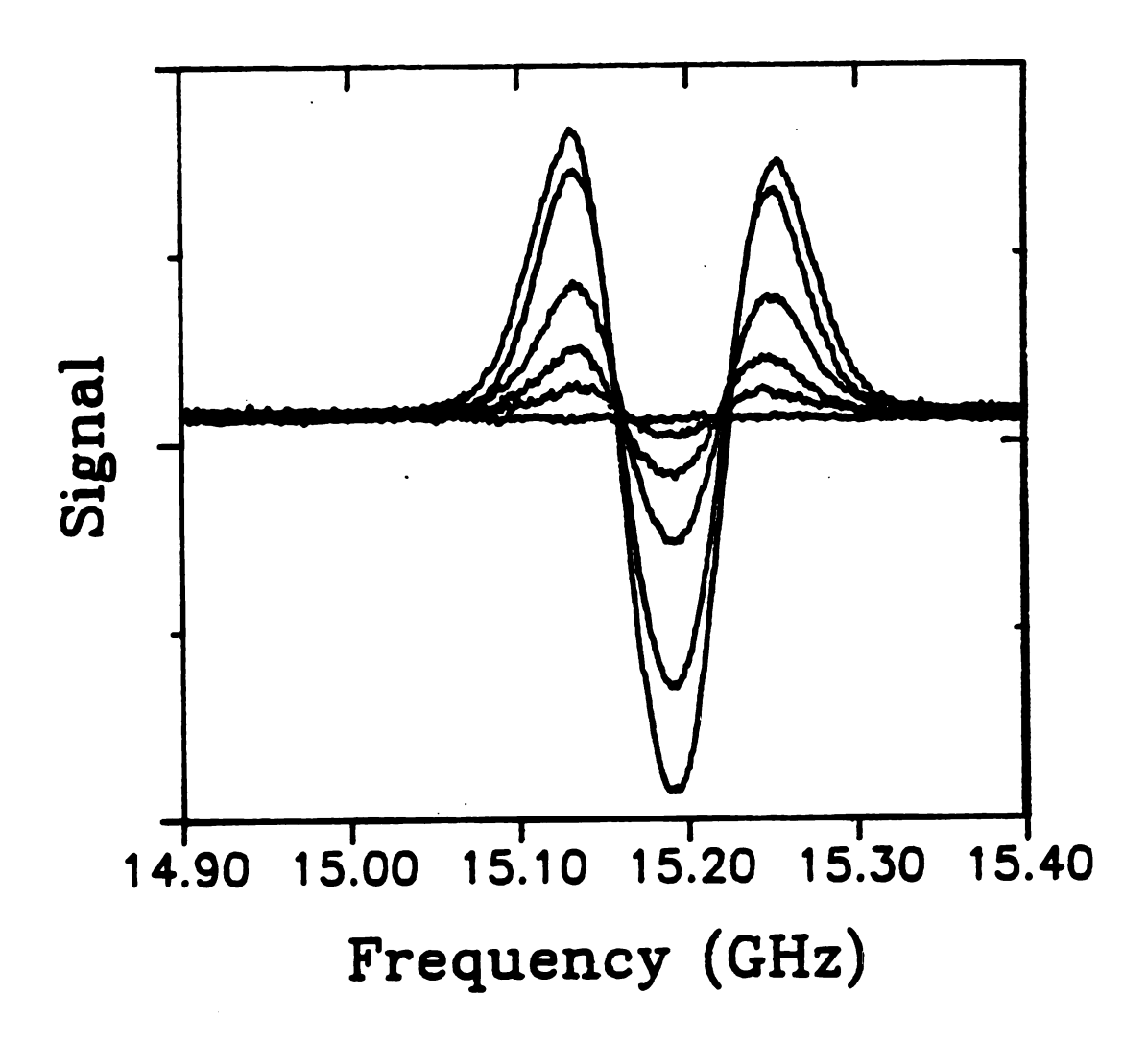


Figure 5.13. Experimental results for the infrared-microwave double resonance on the R(4,1)A transition of CH_3OH , obtained using different pumping powers. The CO_2 laser is on the 9P(24) laser line.

strength inside the cell can be done. This experiment was accomplished by comparing the observed lineshape to that of a calculated signal. For this particular frequency and Q of the cell, the electric field was ~350 V/cm.

The lineshape experiment and calculation were performed to characterize further the application of infrared microwave double resonance with a high power microwave source and a low power infrared source. It should be evident by now that the results obtained with this method for the CH₃OH molecule were not useful, at least by themselves, for the CF₃I case. We conclude, therefore, that the technique of infrared microwave double resonance is experimentally difficult and has some fundamental shortcomings, but it can give information that is unobtainable in any other way.

5.5 References

- V. J. Corcoran, R. E. Cupp, J. J. Gallagher, and W.
 T. Smith, Appl. Phys. Lett. 16, 316 (1970).
- G. Magerl, E. Bonek, and W. A. Kreiner, Chem. Phys. Lett., <u>52</u>, 473 (1977).
- S. K. Lee, R. H. Schwendeman, and G. Magerl, J. Mol. Spec., <u>117</u>, 416 (1986).
- 4. S. K. Lee, R. H. Schwendeman, R. L. Crownover, D. D. Skatrud, and F. C. DeLucia, J. Mol. Spec. 123, 145 (1987).
- 5. S. K. Lee, Ph.D. Thesis, Michigan State University, 1986.
- 6. H. Sasada and R. H. Schwendeman, J. Mol. Spec. <u>117</u>, 331 (1986).
- G. Magerl, J. M. Frye, W. A. Kreiner, and T. Oka, Appl. Phys. Lett., <u>42</u>, 656(1983).
- Y. T. Chen, and T. Oka, Symposium on Molecular Spectroscopy, Ohio State University, June 1987.
- F. Scappini, W. A. Kreiner, J. M. Frye, and T. Oka, J.
 Mol. Spec., <u>106</u>, 436(1984).
- 10. J. O. Henningsen, J. Mol. Spec., <u>85</u>, 282(1981).
- 11. J. O. Henningsen, J. Mol. Spec., 102, 399 (1983).
- 12. H. P. Benz, A. Bauder, and Hs. H. Gunthard, J. Mol. Spec., 21, 156(1966).

- 13. H. Jones and F. Kohler, J. Mol. Spec., <u>58</u>, 125 (1975).
- 14. F. Kohler, H. Jones, and H. D. Rudolph, J. Mol. Spec., 80, 56 (1980).
- W. Fawzy, and R. H. Schwendeman, J. Mol. Spec., <u>120</u>,
 317 (1986).
- 16. H. H. Ritze and V. Stert, J. Mol. Spec., <u>94</u>, 215 (1982).
- 17. P. K. Wahi, V. A. Job, and V. B. Kartha, J. Mol. Spec., 114, 305 (1985).
- 18. H. Burger, K. Burczyk, H. Hollenstein, and M. Quack, Mol. Phys., <u>55</u>, 255 (1985).
- 19. S. W. Walters and D. H. Whiffen, J. Chem. Soc., Faraday
 Trans. 2, 79, 941 (1983).

CHAPTER VI

Summary and Future Work

6.1 Summary

This chapter presents an overview of the results obtained by the different experiments performed for this thesis in the high resolution infrared and microwave spectroscopy laboratory at Michigan State University. The experiments presented in the previous chapters are diverse in nature, but had a common goal, which was to develop and apply double resonance techniques to molecular systems for a better understanding of these systems. This goal was reached for the microwave-microwave double resonance study, but only partially achieved in the infrared-microwave double resonance experiments.

The microwave-microwave double resonance studies on $\mathrm{NH_3}$ -He and $\mathrm{NH_3}$ -H₂ were four level double resonance experiments. The information gained concerned the molecular collisional processes of $\mathrm{NH_3}$ with He and $\mathrm{NH_3}$ with H₂. The results of the microwave-microwave double resonance experiment (1) were complementary to earlier experimental work done by Oka et al.(2-6). The more recent theoretical calculations show that $\mathrm{Oka's}$ and our experiments were

carried out correctly. A further experiment, done by Das and Townes (7), gives similar results on the "collisional selection rules" developed by Oka. It is our conclusion that this work on NH_3 -He and NH_3 -H₂ collisions can only be further understood by additional theoretical calculations.

The FTIR-microwave double resonance experiment described in Chapter 3 was not so successful, but has some very interesting possibilities. If the experiment could be realized, the data from such a double resonance study would be very important for complex molecules. Therefore, I believe that this experiment should be tried again after steps are taken to increase the signal to noise ratio of the FTIR spectrometer.

The uses of the CO₂ sideband spectrometer in Chapters 4 and 5 show its importance in the field of high resolution infrared spectroscopy. The CH₃OH one photon study of the CO stretching fundamental band agrees in essence with the experimental work previously completed by Sattler et al. (8,9), but has more accurate frequencies for the transitions and also many additional transitions not reported earlier. A list of the infrared transitions measured and their relative intensities is given in the Appendix.

The infrared-microwave double resonance experiment with a high power microwave source and with the ${\rm CO}_2$ sideband

laser as an infrared source worked very well. The results obtained by this method provided some previously unidentified Q-branch transitions in the CO stretch band of CH₃OH. The selectivity of the method was not as high as needed to unravel the complex spectrum of CF₃I. The problem associated with the strong microwave pumping radiation is the broad range of the pump. The multi-level pumping problem exists because of the large Rabi frequency needed to overcome the Doppler width of the infrared transition. One possible way to proceed is to employ sub-Doppler spectroscopic conditions in the infrared region. This can be achieved by Lamb-dip experiments similar to those described in the next section.

6.2 Future Work

In this section we propose an extension to the infrared-microwave double resonance studies described above. The extension involves use of partial saturation of Lamb-dip conditions for the infrared absorption. To understand the Lamb-dip experiment we must first describe the process of Doppler averaging associated with infrared transitions. Since the half-width at half-height of a line is given by

$$\Delta v_{\rm D} = 2 \left[\frac{\omega^0}{c} \right] \left[\frac{2 \, kT \, ln2}{m} \right]^{1/2} , \qquad (6.1)$$

as the frequency is increased so is the Doppler width. In the mid-infrared region the Doppler width is much larger than the pressure broadening for low pressure gases whereas in the centimeter microwave region it is smaller except for extremely low pressures. The Doppler broadening is due to the different velocities of the molecules in the direction of the incident radiation. If we can eliminate the velocity distribution, we can eliminate the Doppler broadening of the line.

One way to reduce the effect of the velocity distribution is to pass the radiation through the sample cell twice, as shown in Figure 6.1. The only additional feature in Figure 6.1, apart from the reflection of the beam

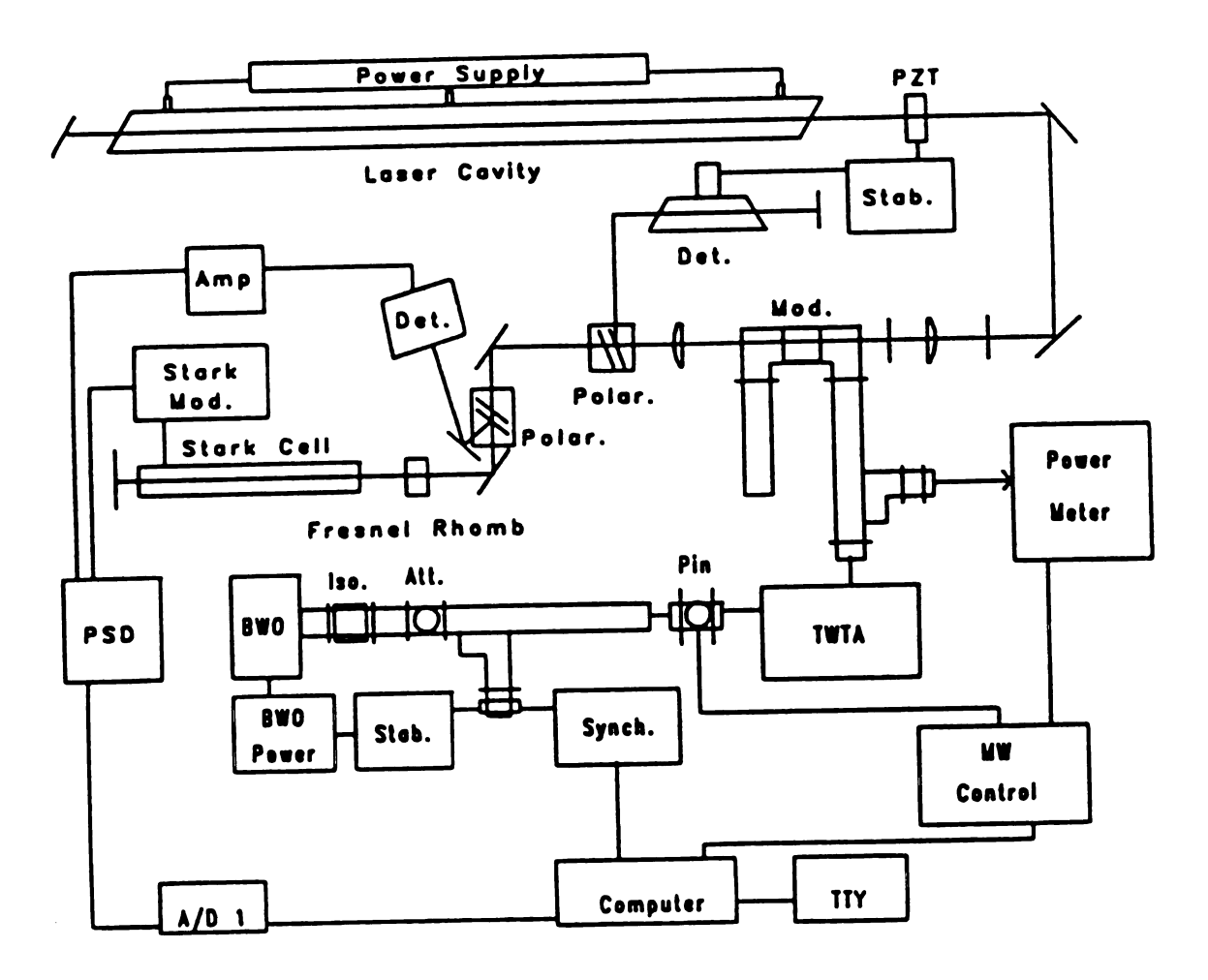


Figure 6.1. Diagram of sideband laser Lamb-dip spectrometer.

back through the cell, is the use of the Fresnel Rhomb to allow the two beams to be coincident. The rhomb converts the plane polarized incoming beam to circularly polarized radiation. After passing through the cell and reflection, the second passage through the rhomb converts the circularly polarized radiation to plane polarization again, but with the polarization plane 90° to the original. Therefore, a polarizer can separate the incoming and outgoing beams.

If for this experiment we call the direction of the radiation beam the z axis, then the molecules with the velocity component v along the z axis experience two Doppler shifted electric fields,

$$E(v) = E_{+}\cos(1+v/c)\omega t + E_{-}\cos(1-v/c)\omega t, \qquad (6.2)$$

where ω is the laboratory frequency of the laser and B_+ and B_- are the electric fields of incoming and reflected laser radiation, respectively. While molecules with $v \neq 0$ are resonant with only one of the two laser fields, molecules with v = 0 are resonant for both fields and experience twice the saturation. This leads to the generation of saturation dips. These Lamb-dips (10), as they are called, are Doppler free and therefore have much smaller line widths. By using the Lamb-dip technique much smaller microwave fields would be required to see the double resonance effect

of the infrared transitions. Smaller microwave fields would pump only one specific transition instead of pumping many off-resonance transitions at once.

The infrared microwave sideband laser has been shown by Magerl et al. (11) to have sufficent power to produce saturation dips. We have also been able to see such dips by using a Stark modulation scheme. A plot of saturation dips in the Q(5,3) transition in the ν_2 band of CH_2F is shown in Figure 6.2. This spectrum was recorded by employing squarewave modulation of an electric field between 0 and 20 volts/cm. The Stark field splits the molecular transitions into their m components, thereby causing an amplitude modulation of the absorption. The experimental setup for this study is shown in Figure 6.1. The sideband radiation was not amplitude modulated for this experiment, so the only change is from the Stark effect. The square wave Stark modulation could be replaced with square wave amplitude modulation of a microwave pump. This procedure would modulate only those transitions which had an energy level in common with one of the pumped levels. Since the saturation dips are less than 1 MHz wide, microwave Rabi frequencies of this magnitude should be sufficient. The infrared-microwave experiment using the Lamb-dip technique might be a useful technique to try with the CF₃I molecule.

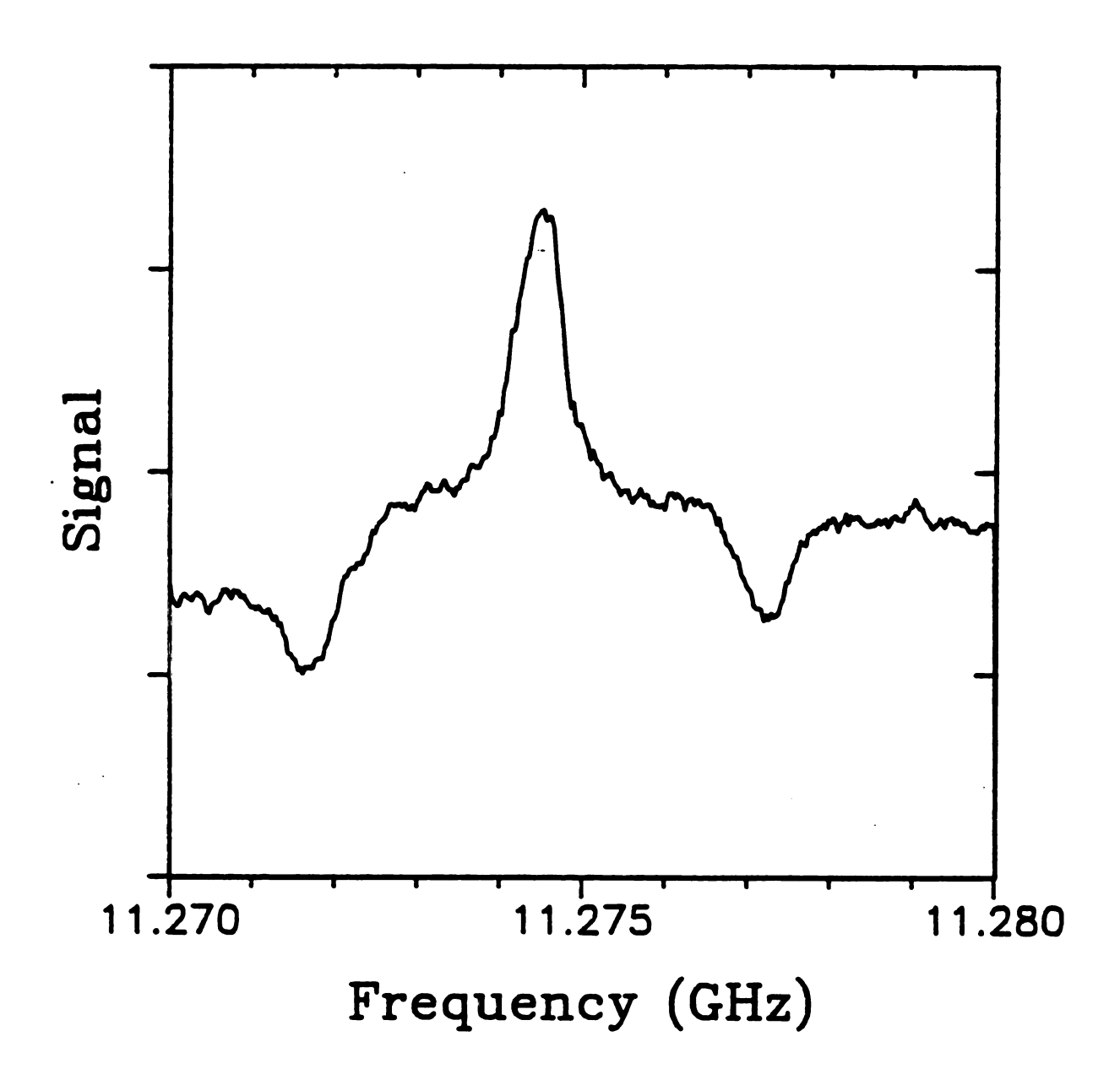
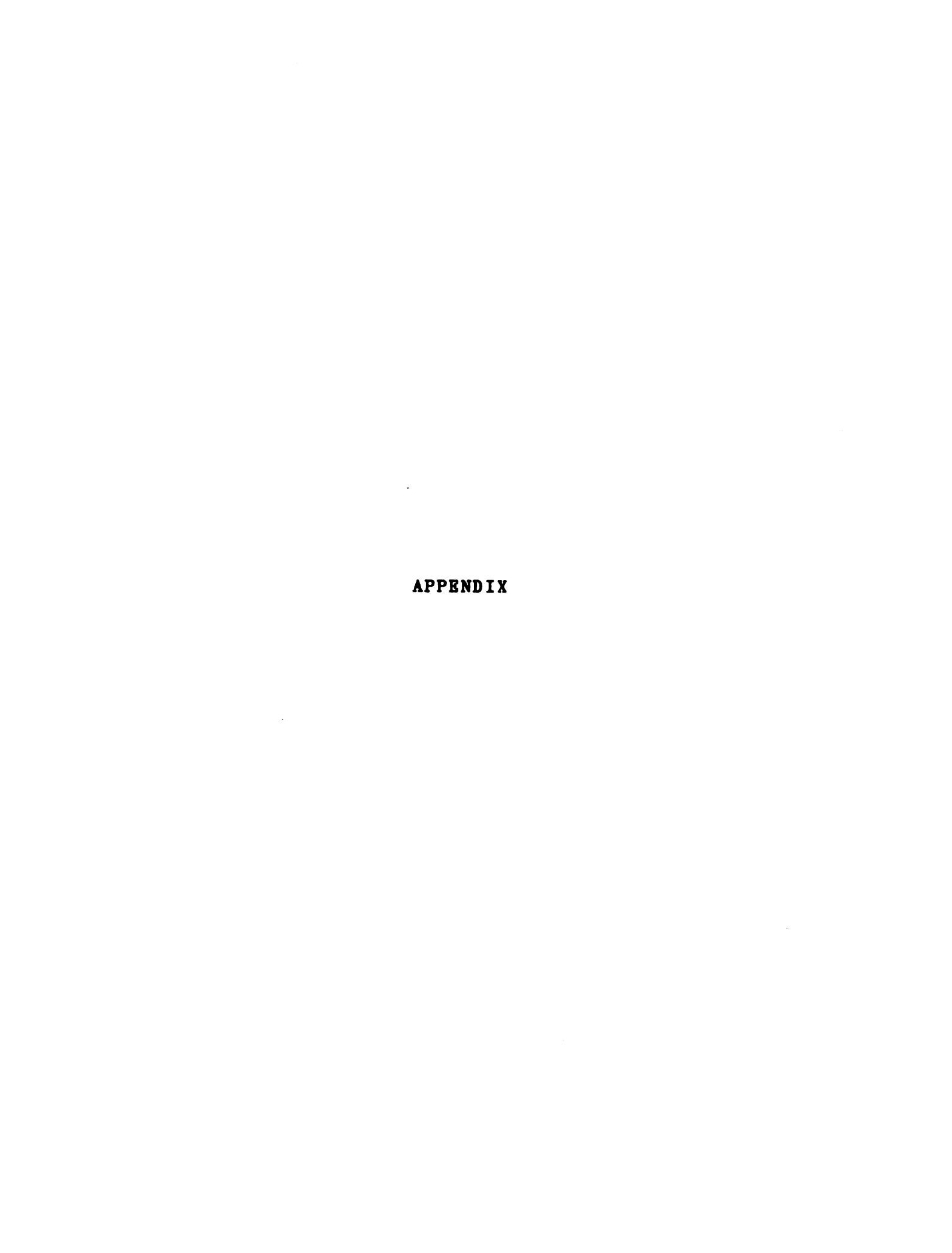


Figure 6.2. A plot of a Stark modulated Lamb-dip from the Q(5,3) transition of CH_3F .

6.3 References

- D. B. Peterson, and R. H. Schwendeman, J. Chem. Phys. 86, 7241 (1987).
- 2. T. Oka, J. Chem. Phys. 47, 4852 (1967).
- 3. T. Oka, J. Chem. Phys. 48, 4919 (1968).
- 4. T. Oka, J. Chem. Phys. 49, 3135 (1968).
- 5. P. W. Daly, and T. Oka, J. Chem. Phys. <u>53</u>, 3272 (1970).
- 6. A. R. Fabris and T. Oka, J. Chem. Phys. <u>56</u>, 3168 (1972).
- 7. A. Das, and C. H. Townes, J. Chem. Phys. 85, 179 (1986).
- 8. J. P. Sattler, T. L. Worchesky, and W. A. Riesler, Infrared Phys. 18, 521 (1978).
- 9. J. P. Sattler, T. L. Worchesky, and W. A. Riesler, Infrared Phys. 19, 217 (1979).
- 10. W. E. Lamb, Jr., Phys. Rev. 134A, 1429 (1964).
- 11. G. Magerl, J. M. Frye, W. A. Kreiner, and T. Oka, Appl. Phys. Lett., <u>47</u>, 656 (1983).



Appendix

This Appendix lists the transition frequencies that were measured for the CO stretch band of the CH₃OH molecule. Because the two sidebands were not separated, only an absolute microwave frequency (GHz) can be given for the transitions. The list is displayed by laser line and microwave frequency. The intensities of all of the transitions are estimated as weak (W), medium (M), strong (S) or very strong (VS).

10R(6) 12c1602 1	aser line a	at 966.250360 cm ⁻¹ .	
11305.853	(W)	11708.119	(W)
10R(8) 12c16o2 1	aser line a	at 967.707233 cm ⁻¹ .	
10165.744	(W)	11479.206	(W)
10866.616	(W)	11800.336	(W)
11310.655	· (W)	12047.633	(W)
10R(10) 12c16o2	laser line	at 969.139547 cm ⁻¹ .	
10477.897	(W)	11712.375	(M)
10R(14) 12c16o2	laser line	at 971.930258 cm ⁻¹ .	
10066.798	(W)	10925.326	(W)
10755.910	(W)		

10R(16)	¹² c ¹⁶ o ₂	laser	line	at	973.288516 cm ⁻¹ .	
9	9435.340	(V	۷)		9936.347	(M)
9	9645.237	(1	۷)		10728.197	(M)
10R(18)	¹² c ¹⁶ o ₂	laser	line	at	974.621939 cm ⁻¹ .	
10	0423.763	(1	۷)			
10R(20)	¹² c ¹⁶ o ₂	laser	line	at	975.930493 cm ⁻¹ .	
9	9372.400	(1	٧)		11002.632	(W)
9	9650.966	(1	1)		11727.015	(W)
9	9915.174	(1	٧)		11920.473	(W)
10	0668.733	(1	1)			
10R(22)	¹² c ¹⁶ o ₂	laser	line	at	977.213922 cm ⁻¹ .	
9	9820.005	(1	۷)		11744.501	(W)
10	0690.437	(1	٧)		11762.194	(W)
10R(24)	¹² c ¹⁶ o ₂	laser	line	at	978.472285 cm ⁻¹ .	
10	983.395	(1	٧)		11146.605	(W)
1	1055.214	(1			11635.553	
10R(26)	¹² c ¹⁶ o ₂	laser	line	at	979.705420 cm ⁻¹ .	
9	9588.984	(1	٧)		11086.345	(M)
9	9682.722	(¥	٧)		11436.595	(W)
•	9892.476	(1	٧)		11512.685	(M)
10	976.495	(1	٧)			

10R(28) 12c16o2	laser line	at 980.913210 cm ⁻¹ .	
9822.575	(W)	11213.743	(M)
10291.176	(W)	12038.836	(W)
10R(30) 12c16o2	laser line	at 982.095530 cm ⁻¹ .	
9416.936	(M)	10685.815	(M)
9765.589	(W)	11236.097	(M
9913.104	(W)	11758.493	(W
10234.634	(M)	12045.813	(W
10458.351	(M)		
10R(32) 12c16o2	laser line	at 983.252249 cm ⁻¹ .	
9414.117	(W)	10684.151	(M
9770.055	(W)	11234.037	(M
9918.509	(W)	11754.391	(W
10276.537	(M)	12029.626	(W
10461.579	(M)		

9P(36)	¹² c ¹⁶ o ₂	laser line	at	1031.477430 cm ⁻¹ .	
1	2381.834	(S)		15701.569	(S)
1	2634.805	(S)		15781.546	(M)
1	2749.212	(M)		15925.403	(S)
1	2752.750	(S)		16166.109	(8)
1	3124.729	(M)		16331.344	(VS)
1	3270.547	(W)		16589.616	(VS)
1	4488.296	6 (W)		16701.968	(VS)
1	4835.297	(M)		16870.761	(VS)
1	4978.103	(M)		16969.188	(VS)
1	5505.948	B (S)		17121.908	(VS)
9P(34)	¹² c ¹⁶ o ₂	laser line	at	1033.487999 cm ⁻¹ .	
1	2540.211	(V S)		16203.403	(VS)
1	2680.676	(S)		16413.347	(VS)
1	2798.580	(M)		16694.627	(VS)
1	2938.955	(S)		16923.222	(S)
1	3159.644	(S)		17155.847	(M)
1	3320.842	(S)		17236.524	(VS)
1	3549.288	(S)		17338.715	(M)
1	3726.006	S (S)		17650.241	(VS)
1	3817.301	(M)		17857.348	(S)
1	3931.411	(S)		17984.468	(S)
1	6082.096	S (VS)			

9P(32)	12c16o2	laser line at	1035.473616 cm ⁻¹ .	
12	2410.960	(W)	15221.521	(W)
12	2640.439	(W)	15334.099	(W)
13	3001.789	(W)	15453.679	(W)
13	3062.504	(M)	15670.059	(M)
13	3191.916	(M)	15780.409	(W)
13	3296.670	(W)	16107.860	(W)
13	3535.398	(M)	16264.618	(W)
13	3676.345	(W)	16608.048	(M)
14	1089.519	(W)	16713.887	(W)
14	1349.908	(M)	16962.424	(W)
14	1532.375	(S)	17430.548	(M)
15	5131.742	(M)	17775.637	(W)
9P(30) 1	12c16o2	laser line at	1037.434110 cm ⁻¹ .	
1.0				
12	2668.429	(W)	15832.121	(W)
	2668.429 2930.127	, ,	15832.121 16067.268	(W) (W)
12		(W)		
12 13	2930.127	(W) (W)	16067.268	(W)
12 13 13	2930.127 3264.369	(W) (W) (W)	16067.268 16168.172	(W)
12 13 13	2930.127 3264.369 3533.622	(W) (W) (W)	16067.268 16168.172 16522.189	(W) (W) (VS)
12 13 13 14 15	2930.127 3264.369 3533.622 1203.592	(W) (W) (W) (M)	16067.268 16168.172 16522.189 16765.686	(W) (W) (VS) (W)

9P(28) 12c16o2 las	ser line at	1039.369314 cm ⁻¹ .	
12485.147	(W)	15876.409	(VS)
12747.843	(M)	16094.408	(S)
12997.548	(M)	16407.361	(M)
13414.586	(VS)	16858.452	(M)
13683.217	(W)	17110.369	(W)
13952.292	(M)	17606.367	(S)
15101.267	(M)	17805.142	(W)
9P(26) 12c1602 las	ser line at	1041.279074 cm ⁻¹ .	
9611.117	(W)	15721.398	(VS)
10138.663	(W)	16072.848	(W)
10541.298	(M)	16345.408	(M)
14650.566	(M)	16976.601	(W)
15199.525	(S)		
9P(24) 12c1602 las	ser line at	1043.163239 cm ⁻¹ .	
9355.457	(VS)	13484.538	(S)
9529.798	(S)	13600.605	(M)
10076.012	(W)	14216.101	(M)
10453.621	(S)	14439.049	(M)
10628.454	(S)	15104.427	(M)
10754.866	(M)	15292.709	(W)
11115.109	(W)	15939.769	(W)
11583.446	(W)	16592.505	(M)
11942.081	(W)	16926.228	(W)
12412.931	(VS)	17267.867	(M)
12518.536	(VS)	17761.467	(M)
12657.404	(S)		

9P(22)	¹² c ¹⁶ o ₂	laser lin	e at	1045.021669 cm ⁻¹ .	
10	045.980) (VS))	14716.785	(W)
10	0176.217	(M)		15618.843	(VS)
12	2937.51	(VS))	16870.117	(M)
13	3066.316	S (W)			
9P(20)	12c16o2	laser lin	e at	1046.854234 cm ⁻¹ .	
9	9395.477	7 (VS))	14279.281	(S)
9	9665.978	3 (S)		14797.637	(M)
9	9964.665	5 (W)		14976.298	(8)
11	1382.806	(VS))	15111.939	(W)
11	1523.258	B (M)		15342.307	(W)
11	1800.129	(M)		16159.497	(W)
12	2582.089	(S)		16332.686	(W)
12	2841.07	(M)		16428.638	(W)
13	3139.600	(W)		16586.694	(S)
13	3963.856	(W)		16755.001	(S)
9P(18)	12c16o2	laser lin	e at	1048.660809 cm ⁻¹ .	
9	9493.822	? (W)		11931.094	(W)
9	9902.895	5 (W)		12627.631	(M)
9	9988.79	(W)		12872.796	(W)
10	389.278	B (W)		14300.555	(M)
10	935.575	(W)		14522.827	(M)
11	1156.419	(M)		14907.046	(W)
11	1269.952	(W)		15212.984	(W)
11	1407.28	(W)		15623.208	(M)
11	1570.069	(W)		15725.552	(S)

9P(16)	¹² c ¹⁶ o ₂	laser line	at	1050.441282 cm ⁻¹ .	
	9530.259	(S)		10678.409	(M)
	9701.715	(S)		10961.088	(M)
	9928.068	(S)		11878.128	(S)
1	10084.209	(S)		11965.029	(M)
9P(14)	¹² c ¹⁶ o ₂	laser line	at	1052.195545 cm ⁻¹ .	
	9417.868	B (S)		11122.938	(W)
	9695.514	(W)		11267.514	(M)
	9873.130	(S)		11365.653	(M)
]	10239.099	(M)		11744.097	(M)
]	10577.813	B (W)		12072.052	(M)
]	10821.332	(S)			
9P(12)	¹² c ¹⁶ o ₂	laser line	at	1053.923503 cm ⁻¹ .	
	9492.153	3 (W)		10212.493	(M)
	9589.169	(W)		11783.491	(W)
	9765.349	(M)		10538.906	(W)
	10001.41	5 (W)		11196.796	(VS

